7N-05
178474
9/8

TECHNICAL NOTE
D-218

LONGITUDINAL AERODYNAMIC CHARACTERISTICS

OF A HIGH-SUBSONIC-SPEED TRANSPORT AIRPLANE MODEL WITH

A CAMBERED 40° SWEPTBACK WING OF ASPECT RATIO 8 AT

MACH NUMBERS TO 0.96

By Atwood R. Heath, Jr.

Langley Research Center
Langley Field, Va.

NATIONAL AERONAUTICS AND SPACE ADMINISTRATION

WASHINGTON   February 1960

NATIONAL AERONAUTICS AND SPACE ADMINISTRATION

TECHNICAL NOTE D-218

LONGITUDINAL AERODYNAMIC CHARACTERISTICS

OF A HIGH-SUBSONIC-SPEED TRANSPORT AIRPLANE MODEL WITH

A CAMBERED 40° SWEPTBACK WING OF ASPECT RATIO 8 AT

MACH NUMBERS TO 0.96

By Atwood R. Heath, Jr.

SUMMARY

The longitudinal aerodynamic characteristics of a complete transport airplane configuration designed for high subsonic speeds with a cambered wing of aspect ratio 8 and 40° of sweepback have been determined. The wing was cambered for a lift coefficient of 0.514, had a taper ratio of 0.3, and had NACA 65A-series airfoil sections perpendicular to the wing quarter-chord line. Modifications to the model such as changes in the fuselage shape, leading-edge extensions on the wing, special wing bodies, and lower surface ridges on the wing have been investigated. Model force and moment measurements were made in the Mach number range from 0.40 to 0.96 for model angles of attack from -5° to 12° in the Reynolds number range from 2.48×10^6 to 4.4×10^6. A modification to a fuselage which was contoured for the area-rule for Mach number 1.00 with superposed streamlines gave higher maximum lift-drag ratios above a Mach number of 0.70 than a cylindrical fuselage of the same maximum cross-sectional area. Wing-root leading-edge extensions improved the maximum lift-drag ratios at Mach numbers above 0.87. The addition of special wing bodies on the configurations with the leading-edge extensions improved the maximum lift-drag ratios at Mach numbers above 0.90. Addition of low spanwise ridges to the wing lower surface alleviated the unstable pitch tendencies noted in the high-subsonic-speed range.

INTRODUCTION

The design of an efficient high-subsonic-speed transport airplane requires a configuration with a high lift-drag ratio which remains high as a Mach number of 1.0 is approached. The problems associated with such a configuration have been investigated previously and were reported in references 1 to 3. Reference 1 is concerned with the longitudinal characteristics of a twisted and cambered wing of high aspect ratio.

References 2 and 3 are concerned primarily with delaying the abrupt drag rise that occurs below but near a Mach number of 1.0 by means of fuselage modifications and special bodies on the wing.

The present investigation was made to determine the performance of a wing of relatively high aspect ratio and sweepback as part of a complete transport configuration which included pylon-mounted nacelles. The wing was cambered by using linear theory for the special case of sonic velocity. The effects of fuselage shape on drag were explored, particularly the effects of a fuselage contoured to fit in the flow field of the cambered wing. In addition, methods of increasing the Mach number at which the abrupt rise in drag occurs were also investigated. For this part of the investigation, inboard extensions on the wing leading edge and special bodies on the wing similar to those of reference 3 were used.

The investigation was made over a Mach number range from 0.40 to 0.96 and angle-of-attack range from -5° to 12°. The Reynolds number based on wing mean aerodynamic chord varied from 2.48×10^6 to 4.40×10^6. Lift, drag, and pitching-moment data as well as pressures in the wing-fuselage juncture were obtained.

SYMBOLS

a_0, a_1, a_2 coefficients of equation for spanwise variation of lift coefficient

b wing span

$C_{A,I}$ nacelle internal-drag coefficient

C_D drag coefficient, D/qS

C_L lift coefficient, L/qS

C_{L_α} lift-curve slope

C_m pitching-moment coefficient about quarter-chord point of wing mean aerodynamic chord, $\dfrac{\text{Pitching moment}}{qS\bar{c}}$

$C_{m_{C_L}}$ static-longitudinal-stability parameter

$C_{m_{i_t}}$ horizontal-tail effectiveness parameter

C_p pressure coefficient, $\dfrac{p - p_\infty}{q}$

c local wing chord, measured streamwise

c_l distance along local chord, measured from leading edge

$\bar{c}$ wing mean aerodynamic chord

$\bar{c}_t$ horizontal-tail mean aerodynamic chord

c_l section lift coefficient

D drag

D_1 maximum diameter of special bodies on wing

i_t angle of incidence of horizontal tail

k cotangent of wing leading-edge sweep angle, y/x

L lift

M Mach number

p local static pressure

p_∞ free-stream static pressure

q free-stream dynamic pressure

R_1, R_2 external and internal radial ordinates, respectively, of nacelles

r_1, r_2 radii of special bodies on wing (see fig. 11)

S wing area (includes area covered by fuselage)

t maximum thickness of wing section

V free-stream velocity

w downwash velocity (positive upward)

x, y, z streamwise, lateral, and vertical coordinates, respectively

x_1, y_1 streamwise and lateral coordinates, respectively, of field point

x_3, y_3 longitudinal and lateral coordinates, respectively, of the outboard pylon center line, referred to nacelle center line origin at nose

x', x_1', x_2' longitudinal dimensions of special bodies on wing

α angle of attack of fuselage reference line

Γ strength of circulation

ΔC_D incremental drag coefficient

Subscripts:

le leading edge of wing

max maximum

MODELS AND APPARATUS

Models

A photograph of the complete model with the modified contoured fuselage mounted in the Langley 16-foot transonic tunnel is shown in figure 1. A sketch of the model with wing, contoured fuselage, and empennage is shown in figure 2.

Wing.- The wing was twisted and cambered for $C_L = 0.514$ by using the linear theory for the special case of sonic velocity given in the appendix. The calculated streamwise camber ordinates are shown in figure 3. The calculated spanwise distribution of wing twist is shown in figure 4. The wing deflection due to load $\left(C_L = 0.514, \quad M = 0.90, \text{ and } q = 711 \text{ lb/sq ft} \right)$ was also calculated, and the calculated wing twist was adjusted for this deflection. The twist distribution adjusted for deflection due to load, which was used for the wing construction, is shown in figure 4. The wing had an aspect ratio of 8, taper ratio of 0.3, and 40° of sweepback of the quarter-chord line. The airfoil sections perpendicular to the quarter-chord line were the NACA 65A-series. The wing thickness-chord ratio, streamwise, varied from 0.12 at the root to 0.06 at 0.60 semispan and remained at 0.06 to the tip. Figure 4 shows the variation of thickness-chord ratio with semispan station. The wing was constructed of steel.

Fuselages.- Two different fuselages were used, and modifications were made to each. Both fuselages were constructed of plastic resin and glass cloth. The first fuselage, hereinafter called the cylindrical fuselage, had nose and center sections which were circular in cross section. (See fig. 5(a).) The nose was an ellipsoid of revolution with a fineness ratio of 3.577, whereas the rearward part of the fuselage tapered to an elliptic cross section where the sting entered the fuselage. The fuselage fineness ratio based on the truncated length of the fuselage was 10.62, and the maximum cross-sectional area was 5 percent of the wing plan-form area. The combined wing and fuselage cross-sectional area was 7.89 percent of the wing plan-form area.

The cylindrical fuselage was modified by an addition to the top of the fuselage just ahead of the wing. The modification was similar to modifications used in reference 2. A sketch of the modified cylindrical fuselage is shown in figure 5(b) and the longitudinal distributions of cross-sectional area for both the cylindrical and modified cylindrical fuselage are shown in figure 6.

A sketch of the contoured fuselage is shown in figure 2. The fuselage was indented according to the area rule for a Mach number of 1.00. (See ref. 4.) Streamlines due to the design lift coefficient $C_L = 0.514$ and due to the wing thickness have been calculated for the fuselage. These streamlines were combined with the area-rule lines to give the resultant fuselage shape in the region of the wing. Figure 7 shows the resultant cross sections of the fuselage. The maximum cross-sectional area of the fuselage was 5 percent of the wing plan-form area. The fuselage and wing combined had a longitudinal cross-sectional-area distribution equal to that of an ellipsoid of revolution with a maximum cross-sectional area which was 5.31 percent of the wing plan-form area. (See fig. 8.)

The contoured fuselage was modified in the region of the wing but above the wing only. The modified top fuselage line is shown in figure 2. Several modified cross sections are shown in figure 7, and the cross-sectional-area distribution is shown in figure 8.

Empennage.- The horizontal tail was made of aluminum alloy, had an aspect ratio of 4.0, taper ratio of 0.3, and sweepback of the quarter-chord line of 40°. NACA 65A006 airfoil sections, streamwise, were used. The vertical tail was made of plastic with a steel core, had an aspect ratio of 1.25, taper ratio of 0.3, and sweepback of the quarter-chord line of 40°. NACA 65A006 airfoil sections, streamwise, were used. Sketches of the vertical and horizontal tails are shown in figure 2.

Nacelles and pylons.- The model was fitted with four pylon-mounted nacelles made of glass cloth impregnated with plastic resin. Figure 9 shows sketches of the nacelles and pylons and tables of the external and

internal nacelle coordinates and pylon center-line coordinates. The inlets were NACA 1-62.5-174.5-series cowlings based on a critical Mach number of 0.88. (See ref. 5.) Streamlines of the flow field under the wing were calculated, and the nacelles were alined with the local flow at the inlets. The pylons were contoured and oriented to fit in the calculated flow field. NACA 65A006 airfoil sections streamwise were used for the pylons, and the leading edge of each pylon was swept back 75°.

Wing leading-edge extensions.- Two wing leading-edge extensions were investigated, and figure 10 shows sketches of the plan forms and wing cross sections. Leading-edge extension I was made by extending the wing root chord 19.1 percent. Then, the new wing leading-edge apex was connected with the midsemispan leading edge by a straight line to form a cranked-wing plan form. The maximum thicknesses of the wing sections were not changed; therefore, the maximum thickness-chord ratio at the root decreased from 0.1200 to 0.1008. NACA 65A-series airfoils, streamwise, were used for the extension and were made fair with the original wing at the maximum thickness locations. Leading-edge extension II was formed in a manner similar to extension I by increasing the root chord by 38.2 percent. Again, the maximum thicknesses of the wing sections were not changed; therefore, the thickness-chord ratio at the root decreased to 0.0868. Both extensions removed the camber from the leading edge of the airfoil sections of the inboard part of the wing.

Special wing bodies.- Two configurations utilizing special bodies on the wing similar to those reported in reference 3 were used. Figure 11 shows sketches of the special bodies tested. The first configuration had four bodies on the wing with the bodies located at 25 percent and 45 percent of the wing semispan. Each body was circular in cross section and had a maximum diameter equal to 8 percent of the local wing chord. Each body was ogival in shape and had an afterbody with a fineness ratio of 3.0. The bodies were located on the wing with the maximum diameters placed at 95 percent of the local chord and the body axes yawed out 3°.

The second configuration had six bodies on the wing with the bodies located at 20, 40, and 60 percent of the wing semispan. Each body had a maximum diameter equal to 6.5 percent of the local wing chord. The body shaping and placement on the wing were made in the same manner as for the four-body configuration.

Low spanwise ridges on wing lower surface.- Two ridges were put on each semispan of the wing. The ridges were wooden slats 0.06 inch thick by 0.63 inch wide. (See fig. 12.) The upstream slat was glued to the wing with the leading edge of the slat located on the 0.25 chord line. The slat extended from the fuselage to 0.35 semispan. The other slat had its leading edge located on the 0.70 chord line and extended from the fuselage to 0.625 semispan. Plastic was used at the leading and

trailing edge of each slat to make smooth ridges. These ridges were originally used as fairings for the external tubing necessary for measurement of pressures in the nacelles. The fairings were found to have a beneficial effect on the pitching-moment curves.

Apparatus

The investigation was made in the Langley 16-foot transonic tunnel which is a single-return tunnel with an octagonal, slotted throat. A detailed description of the tunnel is given in reference 6. The model was supported by a sting attached to the support strut which changed angle of attack in such a way that the model was kept close to the tunnel center line.

The model forces and moments were measured by an internal six-component strain-gage balance. The model angles of attack were measured by means of a pendulum-type strain-gage inclinometer located inside the model. Pressures at the wing-fuselage juncture were measured by means of orifices located on the fuselage surface about 0.0625 inch from the wing surface. Four static-pressure orifices located in the duct walls and 13 total-pressure tubes on a cruciform rake in the duct (fig. 9) were used to measure the internal drag of the pylon-mounted nacelles. Only one inboard nacelle and one outboard nacelle were instrumented.

Observations of the flow in the boundary layer of the wing upper surface were made for several configurations by using the fluorescent-oil-film method of reference 7.

TESTS

Tests on about half of the configurations were made for a Mach number range from 0.40 to 0.96. For the rest of the tests, the top Mach number reached was 0.92. At $M = 0.40$, the angle of attack was varied from -5° to 12°. At the other Mach numbers, the angle of attack varied from about -5° to about 3° and was dependent on the balance load limits. The Reynolds number range, based on wing mean aerodynamic chord, varied from about 2.47×10^6 at $M = 0.40$ to about 4.40×10^6 at $M = 0.96$.

The wing was first tested in combination with each of the two fuselages and the two modified fuselages without the empennage. The remainder of the tests were made with the modified contoured fuselage. With the empennage on, tests were made with the horizontal tail at two angles of incidence, $i_t = -1^\circ$ and $i_t = 2^\circ$. Tests were then made of the complete configuration. Tests to determine the internal drag of the nacelles were

made independently of the force tests on the complete configuration because the pressure leads from the nacelles had to be tacked to the lower surface of the wing. The configuration with the wing, modified contoured fuselage, empennage, and the four special wing bodies was then tested. Next, the configurations with the leading-edge extensions were tested with and without the six special wing bodies. Finally, the wing lower-surface ridges were tested in combination with wing leading-edge extension I.

Transition was fixed on the wing and fuselages for all tests by means of 0.125-inch-wide strips of No. 220 abrasive particles. On the wing, strips were located on the upper and lower surfaces at the 2.5-percent chord line. On each fuselage the strip was placed around the nose at 2.5 percent of the body length.

CORRECTIONS AND ACCURACY

Model angles of attack have been corrected for a tunnel upwash angle of 0.17° which was determined from previous tests in the Langley 16-foot transonic tunnel. Based on instrument accuracy and repeatability of data, the model angles of attack are believed to be accurate to $\pm 0.1^\circ$.

The drag data presented herein have had the internal drag of the nacelles removed where required. Figure 13 shows the variation of nacelle internal-drag coefficient with angle of attack for various Mach numbers. All force data have been adjusted to the condition of free-stream static pressure at the model base. The following table shows the accuracy of the aerodynamic coefficients based on instrument error for Mach numbers of 0.40 and 0.80:

	M = 0.40	M = 0.80
C_L	±0.012	±0.004
C_D	±0.0018	±0.0006
C_m	±0.0023	±0.0008

No corrections have been made for either wing aeroelasticity or sting interference.

L
7
0
7

RESULTS AND DISCUSSION

The basic aerodynamic characteristics (lift, drag, and pitching-moment coefficients) of the various configurations are presented in figures 14 to 20, and the analyses of the data are shown in figures 21 to 44 as follows:

	Basic data figure	Analysis figure
Fuselage modifications	14 and 15	21 to 26
Horizontal tail	16	27 and 28
Complete configuration	17	29 to 33
Wing leading-edge extensions . . .	18	34 to 37
Special wing bodies	17 and 19	38 to 41
Wing lower-surface ridges	20	42 to 44

Fuselage Modifications

The effects of fuselage modifications on the longitudinal characteristics of the wing-fuselage combination are shown in figures 14 and 15. Comparisons of the variation of drag coefficient with Mach number for several values of lift coefficient are shown in figure 21. For $C_L = 0.4$, the modification to the cylindrical fuselage increased the drag at Mach numbers below 0.8 but decreased the drag markedly above $M = 0.8$. (See fig. 21(a).) The modification is similar to one in reference 2, and as reported in the reference, the modification decreased the drag of the combination of cylindrical fuselage and wing at the higher Mach numbers. For $C_L = 0.4$, the combinations with the contoured and modified contoured fuselages both had lower values of drag than the cylindrical fuselage above $M = 0.8$ as seen in figure 21(b). This decrease in drag can be explained by the improved flow over the wing-fuselage junctures of the contoured fuselages which is shown by the pressure data of figure 22. In figure 22(a), the pressure distributions for the contoured fuselage show that the drag was less because of the leading-edge pressure peak at all Mach numbers. Pressure distributions for the cylindrical fuselage showed that most of the load was carried toward the rear of the airfoil which would increase the drag. The modified contoured fuselage configuration had a slightly lower drag than the contoured fuselage at $M = 0.90$ and $C_L = 0.4$ as shown in figure 21(b). The pressure distributions of figure 22(b) show that although the modified contouring lowered the pressure peak toward the leading edge of the juncture, the

modified contouring also lowered the pressure peak near 70 percent chord. The net effect of modifying the contouring was to lower the drag as shown in figure 21(b). The modification to the contouring which resulted in lower drag at all Mach numbers and lift coefficients is also advantageous from the viewpoint of fuselage volume which would be critical for the contoured fuselage.

It should be noted that each of the contoured fuselages has a smaller volume than either the cylindrical or modified cylindrical fuselages. If the volume of each of the contoured fuselages were made equal to that of the cylindrical fuselage, it is believed that the differences in drag coefficients shown in figure 21(b) for $C_L = 0.4$ above $M = 0.80$ would be less.

The increase of drag with Mach number near $M = 0.90$ for the wing in combination with the modified contoured fuselage is due to shock-induced separation of the flow over the inboard part of the wing upper surface. Figure 23 shows this flow separation which is indicated by the collection of oil over the back part of the wing. Examination of figure 23 indicates that the flow in the separated region is spanwise.

Figures 14(a) and 15(a) show that modifications to each of the fuselages generally increased the lift coefficient for a given angle of attack. Figure 24 shows that the modification to the cylindrical fuselage improved the lift-curve slope in the region of $M = 0.90$. Both contoured fuselages had a peak in the lift-curve-slope data that occurred at Mach numbers higher than the Mach number at which the peak occurred for the cylindrical-fuselage data.

The modification to the cylindrical fuselage provided an increment in pitching-moment coefficient. (See fig. 14(c).) This increment in pitch would be helpful in decreasing the drag which results from trimming the configuration for level flight. However, the modification to the contoured fuselage did not change the pitch curves essentially. (See fig. 15(c).) The longitudinal-stability-parameter variations with Mach number in figure 25 show that there was little change in static stability for all the wing-fuselage combinations investigated.

The maximum lift-drag ratios and the lift coefficients at maximum lift-drag ratio are presented in figure 26 for the wing-fuselage combinations. Below a Mach number of 0.84, the combination with the modified cylindrical fuselage showed better lift-drag ratios than that with the cylindrical fuselage. Above a Mach number of 0.70, the combinations with contoured and modified contoured fuselages showed better lift-drag ratios than the combination with the cylindrical fuselage. The combinations with the modified contoured and modified cylindrical fuselages have the same maximum lift-drag ratio at $M = 0.90$, but the combination with the

modified contoured fuselage is superior below M = 0.80. The wing combined with the modified contoured fuselage gives the best overall lift-drag ratio of all the wing-fuselage combinations tested.

Figure 16 shows the aerodynamic characteristics of the wing, modified contoured fuselage, vertical tail, and horizontal tail configuration with horizontal-tail incidences of $i_t = -1^\circ$ and $i_t = 2^\circ$. Since the horizontal-tail setting of $i_t = -1^\circ$ appeared to be closer to trim conditions for $C_L = 0.5$ at most Mach numbers, this setting was used for the remainder of the investigation. Figure 27 presents the effect of the horizontal tail, $i_t = -1^\circ$, on the longitudinal-stability parameters for the wing in combination with modified contoured fuselage. An unstable tendency in the $C_{m_{C_L}}$ curves for the tail-off configuration is noticed above M = 0.80. At $C_L = 0.4$, the addition of the horizontal tail caused the tendency to occur at a lower Mach number than the unstable tendency for the tail-off configuration. It appears that the horizontal-tail location was unsuitable for removing the unstable tendency present in the wing-fuselage data.

The horizontal-tail effectiveness parameter $C_{m_{i_t}}$ is presented in figure 28 for lift coefficients of 0.2 and 0.4.

Complete Configuration

The basic aerodynamic data for the complete configuration (wing, modified contoured fuselage, pylon-mounted nacelles, and empennage) is shown in figure 17. The lift-curve slope at $\alpha = 0^\circ$, drag coefficient for various lift coefficients, lift coefficient at maximum lift-drag ratios, and maximum lift-drag ratios are shown in figures 29 to 31. The complete configuration has a maximum lift-drag ratio of about 21.3 at M = 0.50 (fig. 31). However the lift-drag ratio drops abruptly in the region of M = 0.83 due to the rapid increase in drag as seen in figure 30.

A comparison of the longitudinal-stability parameters for the configuration with and without nacelles is shown in figure 32. The addition of the nacelles results in a decrease in stability. The unstable tendency in the pitch curves near M = 0.90 is affected only slightly by the addition of nacelles for the two lift coefficients shown.

Figure 33 shows the variation of the increment in drag coefficient due to the pylon-mounted nacelles with Mach number. For lift coefficients of 0.4 and 0.5, there is an abrupt increase in incremental drag coefficient near M = 0.85. This incremental drag rise due to the nacelles occurs in roughly the same Mach number range as the drag rise of the wing-fuselage combination.

Wing Leading-Edge Extensions

The basic aerodynamic data for the two configurations with the leading-edge extensions are presented in figure 18. Figure 34 shows the variation of drag coefficient with Mach number for the configurations with the plain wing and the wings with the two leading-edge extensions. The addition of the extensions increased the drag below about $M = 0.85$ due to the increased friction drag which is the result of increased wetted area. However, at lift coefficients from 0.3 to 0.5 the abrupt drag rise that occurs for the plain wing above $M = 0.85$ has been delayed to a higher Mach number for wings with leading-edge extensions. The delayed drag rise can be attributed to the fact that the wings with the extensions had lower thickness-chord ratios inboard and also greater sweepback than the plain wing. Also, visual observation of the flow on the wing showed that the shock wave on the wing, similar to that shown in figure 23, had moved toward the trailing edge; therefore, the area of separation with its relatively high negative pressures was reduced. It appears that use of leading-edge extension II provided little added benefit in drag to that already obtained from the use of leading-edge extension I.

The lift-curve slopes for the plain-wing configuration and the two configurations with the extensions are presented in figure 35. In general, the lift-curve slopes below $M = 0.85$ are higher for the configurations with extensions than for the plain-wing configuration. These high slopes can be attributed to the increase in area caused by adding the extensions.

The longitudinal-stability parameters for the plain-wing configuration and the two configurations with the extensions are shown in figure 36 as functions of Mach number. Both configurations with leading-edge extensions are less stable than the plain-wing configuration as shown by the more positive trends of the $C_{m_{C_L}}$ curves for the configurations with leading-edge extensions. The reduction in longitudinal stability is due to the fact that most of the area of the extensions was added ahead of the quarter-chord location of the mean aerodynamic chord of the original wing plan form. At $C_L = 0.4$, the configuration with leading-edge extension I shows an abrupt decrease in stability near $M = 0.87$, and the stability parameter becomes zero at $M = 0.92$. However, the configuration with leading-edge extension II shows a marked improvement in stability over that obtained for the configuration with leading-edge extension I.

Figure 37 shows the variations with Mach number of maximum lift-drag ratio and lift coefficient at maximum lift-drag ratio for the configurations with and without the leading-edge extensions. Addition of the extensions reduced the maximum lift-drag ratios at Mach numbers below

M = 0.85; however, each extension improved the ratios above M = 0.87. The addition of leading-edge extension II caused practically no improvement in lift-drag ratios over those obtained with leading-edge extension I at the higher Mach numbers. It appears that the benefits of a wing with lower thickness-chord ratio and increased sweep which results from the larger extension are offset to some extent by the increased drag from increased skin friction and lower aspect ratio.

Special Wing Bodies

Figure 17 shows the aerodynamic characteristics of the plain wing with four special wing bodies, and figure 19 shows the characteristics of the configurations with the leading-edge extensions and six special wing bodies. Comparisons of the variation of drag coefficient with Mach number for the configurations with and without the special wing bodies are shown in figure 38. Sizable decreases in drag coefficient at lift coefficients from 0.3 to 0.5 are obtained near M = 0.90 by use of four special wing bodies. (See fig. 38(a).) This effect has been previously shown in reference 3. Only four bodies were used because the region of separated flow, which the bodies are designed to correct, extends only slightly outboard of the midsemispan. Figures 38(b) and 38(c) show the effect on drag coefficient of adding six special wing bodies to the configurations with the leading-edge extensions on the wing. Although the leading-edge extensions were responsible for a decrease in drag coefficient near M = 0.90 as seen in figure 34, the addition of the special wing bodies provided further decreases in drag coefficient above M = 0.90. It can be seen that the effects of leading-edge extensions and special wing bodies are complementary, for the present cases. Thus, the best configuration may well require both modifications to the wing for the lowest drag above M = 0.90.

The variations of lift-curve slope with Mach number for the configurations with the special wing bodies and the leading-edge extensions are shown in figure 39. In general, the lift-curve slope above about M = 0.85 is increased by the addition of the bodies.

Figure 40 shows the variations of longitudinal-stability parameter with Mach number for the configurations with special wing bodies with and without the leading-edge extensions. The bodies are very effective in removing the unstable pitch tendency of the plain wing. (See fig. 40(a).) For the wing with leading-edge extension I, an unstable pitch tendency is still present after the addition of the six special wing bodies, but the magnitude of the tendency has been lessened. (See fig. 40(b).) For the wing with leading-edge extension II, the addition of the six special wing bodies affects the longitudinal-stability-parameter curve very little. (See fig. 40(c).) For the latter case, the fact that the bodies do not improve the longitudinal-stability parameter

curve may be due to incorrect body size and location. However, the possibility exists that the bodies are ineffective because the separated area behind the shock wave, which was noticed on the plain wing, was reduced by the addition of the leading-edge extension.

Figure 41 shows the maximum lift-drag ratio and lift coefficient at maximum lift-drag ratio for the configurations with the special wing bodies and leading-edge extensions. In all cases, the addition of the special wing bodies lowers the maximum lift-drag ratio at the lower Mach numbers. However, the lift-drag ratios are increased in the region of $M = 0.90$. In the case of the configuration with leading-edge extension II, the special bodies do not become effective until $M = 0.925$ is reached and then only give small benefits up to $M = 0.96$.

Wing Lower Surface Ridges

Figure 20 shows the aerodynamic characteristics of the wing, modified contoured fuselage, empennage, and lower-surface ridges on the wing. The wing was also fitted with leading-edge extension I. A comparison of the pitching-moment-coefficient curves with and without the ridges is presented in figure 42. The unstable tendency occurring between $C_L = 0.4$ and $C_L = 0.5$ for the configuration without the ridges is reduced when the ridges are added. This favorable effect may be due to modification of the flow over the wing, but this cannot be determined inasmuch as no data with the horizontal tail removed were obtained to determine the effects of the ridges on the wing-fuselage combination. However, the possibility that the wing downwash was changed in such a manner that the horizontal tail supplied the beneficial pitching-moment increments should not be overlooked.

Figure 43 shows comparisons of the drag coefficients for the configuration with and without ridges. The drag is essentially unchanged by the addition of the ridges up to $C_L = 0.4$. At $C_L = 0.5$, the addition of the ridges reduces the drag coefficient above $M = 0.91$. Therefore, in the Mach number range of $M = 0.90$ to 0.96, the ridges can be used with little or no penalty in drag coefficient, and in some cases a reduction in drag is obtained.

A comparison of the pitching-moment-coefficient curves for two configurations with six special wing bodies with and without lower surface ridges is shown in figure 44. An increment in pitching-moment coefficient similar to that obtained from a lower surface flap results from the addition of ridges. The improved flow resulting from the addition of the special bodies eliminates the effects of the ridges on stability. Therefore, the curves of figure 44 do not show the changes in trend seen in the curves of figure 42.

CONCLUSIONS

The longitudinal aerodynamic characteristics of a transport airplane model have been determined for Mach numbers up to 0.96. The cambered 40° sweptback wing was tested with various combinations of two different fuselages, modifications to each fuselage, empennage, pylon-mounted nacelles, wing leading-edge extensions, special wing bodies, and ridges on the lower surface of the wing. From these tests, the following conclusions can be drawn:

1. A modification to a fuselage which has been contoured for the area rule for Mach number 1.00 with superposed streamlines, gave higher maximum lift-drag ratios above a Mach number of 0.70 than a cylindrical fuselage of the same maximum cross-sectional area.

2. Wing leading-edge extensions improved the maximum lift-drag ratios at Mach numbers above 0.87.

3. The addition of special wing bodies on the configurations with the leading-edge extensions improved the maximum lift-drag ratios at Mach numbers above 0.90.

4. Addition of lower surface ridges to the wing alleviated the unstable pitch tendencies noted in the high-subsonic-speed range.

Langley Research Center,
      National Aeronautics and Space Administration,
            Langley Field, Va., November 3, 1959.

L
7
0
7

APPENDIX

DERIVATION OF FORMULAS FOR WINGS WITH UNIFORM

CHORDWISE LOADING IN SONIC FLOW

In order to obtain the ordinates of a camber surface which will carry a specified distribution of loading, it is necessary to know the slope of the downwash at all points on the wing. If the longitudinal dimensions of the wing are stretched according to the Prandtl-Glauert compressibility correction factor for sonic velocity, it can be seen that the bound vortices, which are at an infinite distance upstream, do not contribute to the downwash. Therefore, only the trailing vortices from that part of the wing upstream of the point at which the downwash is desired affect the downwash. Thus, the downwash at a field point such as (x_1, y_1) (see fig. 45) can be determined from the following equation:

$$w = -\frac{1}{2\pi} \int_{-kx_1}^{kx_1} \frac{\frac{d\Gamma}{dy}}{y_1 - y} \, dy \tag{1}$$

As was previously noted, in calculating the downwash at any field point (x_1, y_1) on the wing in sonic flow, it is necessary to take into account only the effect of the wing upstream of (x_1, y_1). The downwash then becomes

$$w = -\frac{1}{2\pi} \int_{-kx_1}^{kx_1} \frac{\frac{d\left[\frac{c_l}{2} V(x_1 - x)\right]}{dy}}{y_1 - y} \, dy \tag{2}$$

Note that this equation is complete for the case of a field point located upstream of the wing trailing-edge apex only. Then, the slope of the downwash or slope of the mean camber surface will be

$$\frac{w}{V} = \frac{dz}{dx_1} = -\frac{1}{4\pi} \left\{ \int_{-kx_1}^{kx_1} \frac{\frac{d\left[c_l(x_1 - x)\right]}{dy}}{y_1 - y} \, dy - \frac{1}{k} \int_{-kx_1}^{kx_1} \frac{c_l}{y_1 - y} \, dy \right\} \tag{3}$$

If the vertical ordinates of the wing leading edge are kept zero, the ordinates of the mean camber surface become

$$z = -\frac{1}{4\pi}\left\{\int_{x_{1,le}}^{x_1}\int_{-kx_1}^{kx_1}\frac{\dfrac{d\left[c_l(x_1-x)\right]}{dy}}{y_1-y}\,dy\,dx_1\right.$$

$$\left.-\frac{1}{k}\int_{x_{1,le}}^{x_1}\int_{-kx_1}^{kx_1}\frac{c_l}{y_1-y}\,dy\,dx_1\right\} \qquad (4)$$

This same equation results when the Prandtl-Glauert method of compressibility correction is applied to the equations for the determination of mean camber surfaces in subsonic flow given in reference 8.

An example of the calculations made for the wing of the present investigation follows. The only loading requirement necessary for the calculations is that the chordwise loading be uniform. For the present case, the variation of lift coefficient spanwise was

$$c_l = 0.5 + 0.32\left(\frac{y}{b/2}\right) - 0.45\left(\frac{y}{b/2}\right)^2 - \underbrace{\left[231.25\left(\frac{y}{b/2}-0.8\right)^4\right]}_{\text{for }\frac{y}{b/2}>0.8\text{ only}} \qquad (5)$$

This lift distribution gives a spanwise loading curve that is approximately elliptical. The sample calculation will be made for the field point (x_1, y_1) that lies upstream of the trailing-edge apex of the wing as shown on figure 45. Also, only the effect of the wing to the right of the x-axis on the camber ordinate will be calculated. Note that only the first three terms of the lift equation are required for the point (x_1, y_1).

18

$$z = -\frac{1}{4\pi k}\left\{\int_{y_1/k}^{x_1}\int_0^{kx_1}\frac{\dfrac{d\left[\left(a_0 + a_1 y + a_2 y^2\right)\left(y - kx_1\right)\right]}{dy}}{y - y_1}\,dy\,dx_1\right.$$

$$\left. + \int_{y_1/k}^{x_1}\int_0^{kx_1}\frac{a_0 + a_1 y + a_2 y^2}{y - y_1}\,dy\,dx_1\right\} \tag{6}$$

where

$$a_0 = 0.5$$
$$a_1 = 0.32$$
$$a_2 = -0.45$$

and all dimensions are made nondimensional in $b/2$. Performing the indicated integration with respect to y and substituting the limits gives

$$z = -\frac{1}{4\pi k}\int_{y_1/k}^{x_1}\left[-\frac{a_2}{2}\left(kx_1\right)^2 + \left(2a_1 + 3a_2 y_1\right)kx_1\right.$$

$$- \left(a_1 + 2a_2 y_1\right)\left(kx_1 - y_1\right)\log_e\frac{\left(kx_1 - y_1\right)}{y_1}$$

$$\left. + \left(a_0 + a_1 y_1 + a_2 y_1^2\right)\log_e\frac{\left(kx_1 - y_1\right)}{y_1}\right]dx_1 \tag{7}$$

Then integrating with respect to x_1 and substituting limits gives the camber ordinate.

$$z = -\frac{1}{4\pi k^2} \left\{ -\frac{a_2}{6}\left[(kx_1)^3 - y_1^3\right] + \left(a_1 + \frac{3}{2} a_2 y_1\right)\left[(kx_1)^2 - y_1^2\right] \right.$$

$$-\frac{1}{2}\left(a_1 + 2a_2 y_1\right)\left(kx_1 - y_1\right)^2\left[\log_e \frac{(kx_1 - y_1)}{y_1} - \frac{1}{2}\right]$$

$$\left. + \left(a_0 + a_1 y_1 + a_2 y_1^2\right)\left(kx_1 - y_1\right)\left[\log_e \frac{(kx_1 - y_1)}{y_1} - 1\right] \right\} \qquad (8)$$

These calculations may be made on a desk calculator; however, as many points may be desired to determine the camber surface accurately, the formulas are suitable for calculation by electronic computers.

REFERENCES

1. Edwards, George G., Tinling, Bruce E., and Ackerman, Arthur C.: The Longitudinal Characteristics at Mach Numbers up to 0.92 of a Cambered and Twisted Wing Having 40° of Sweepback and an Aspect Ratio of 10. NACA RM A52F18, 1952.

2. Whitcomb, Richard T.: A Fuselage Addition to Increase Drag-Rise Mach Number of Subsonic Airplanes at Lifting Conditions. NACA TN 4290, 1958.

3. Whitcomb, Richard T.: Special Bodies Added on a Wing to Reduce Shock-Induced Boundary-Layer Separation at High Subsonic Speeds. NACA TN 4293, 1958.

4. Whitcomb, Richard T.: A Study of the Zero-Lift Drag-Rise Characteristics of Wing-Body Combinations Near the Speed of Sound. NACA Rep. 1273, 1956. (Supersedes NACA RM L52H08.)

5. Nichols, Mark R., and Keith, Arvid L., Jr.: Investigation of a Systematic Group of NACA 1-Series Cowlings With and Without Spinners. NACA Rep. 950, 1949. (Supersedes NACA RM L8A15.)

6. Ward, Vernon G., Whitcomb, Charles F., and Pearson, Merwin D.: Air-Flow and Power Characteristics of the Langley 16-Foot Transonic Tunnel With Slotted Test Section. NACA RM L52E01, 1952.

7. Loving, Donald L., and Katzoff, S.: The Fluorescent-Oil Film Method and Other Techniques for Boundary-Layer Flow Visualization. NASA MEMO 3-17-59L, 1959.

8. Katzoff, S., Faison, M. Frances, and DuBose, Hugh C.: Determination of Mean Camber Surfaces for Wings Having Uniform Chordwise Loading and Arbitrary Spanwise Loading in Subsonic Flow. NACA Rep. 1176, 1954. (Supersedes NACA TN 2908.)

L-707

L-58-746
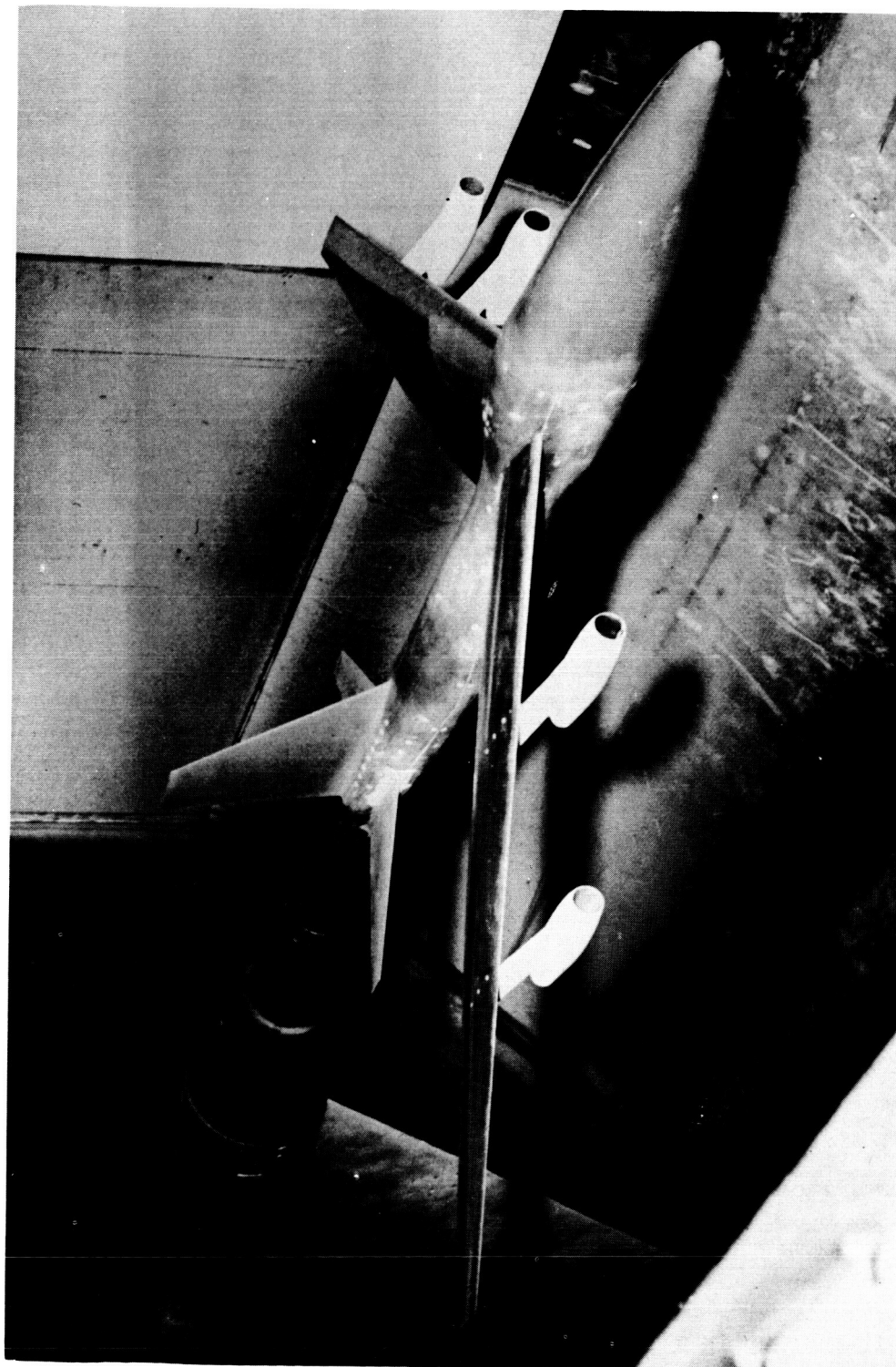
Figure 1.- Photograph of complete model with modified contoured fuselage mounted in the Langley 16-foot transonic tunnel.

	Wing	Horizontal tail	Vertical tail
Sections	NACA 65AXXX	NACA 65A006	NACA 65A006
Area ft^2	8.0	1.6	1.60
Aspect ratio	8.0	4.0	1.25
Taper ratio	.3	.3	.30
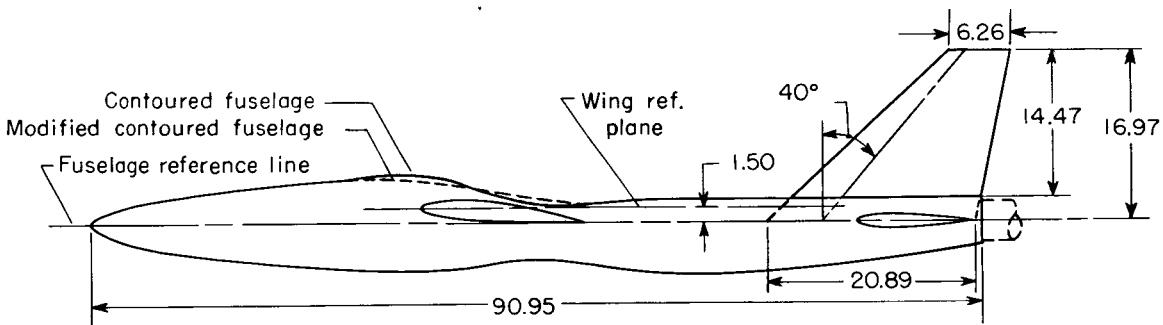
Figure 2.- Sketch of wing with contoured fuselage and empennage. All dimensions in inches unless otherwise noted.
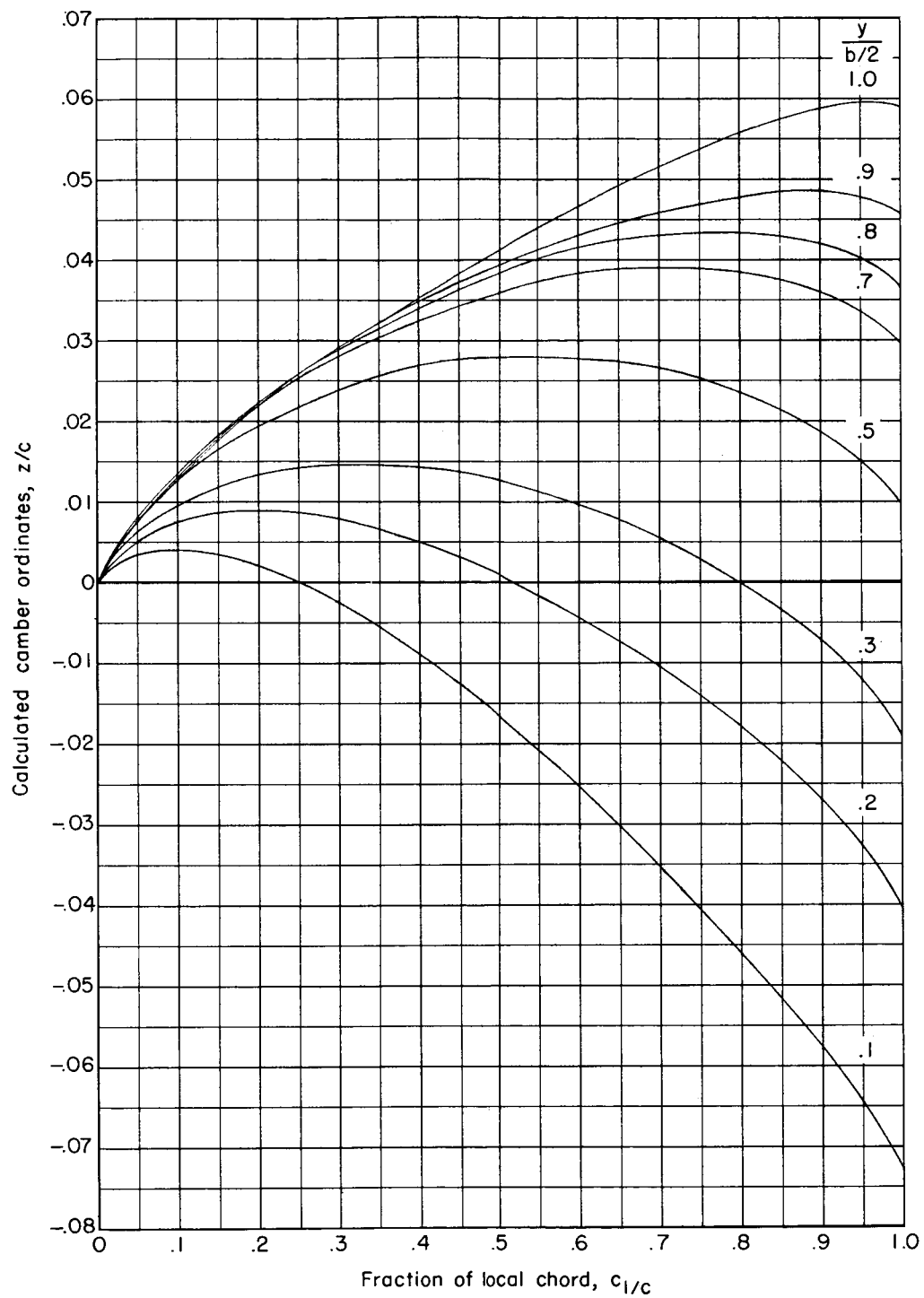
Figure 3.- Calculated streamwise camber ordinates for different spanwise stations.
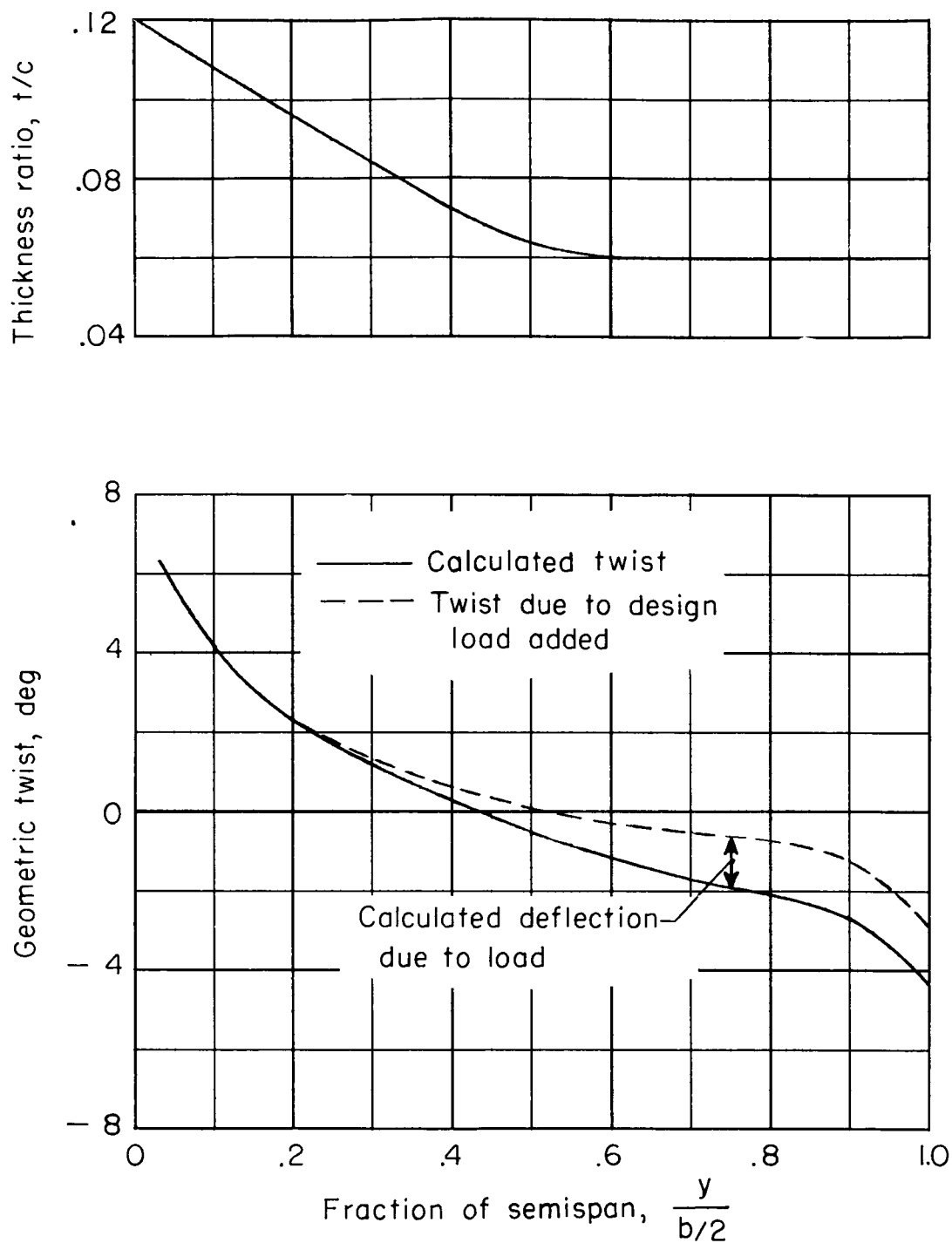
Figure 4.- Variation of wing geometric twist and maximum thickness-chord ratio with spanwise station.
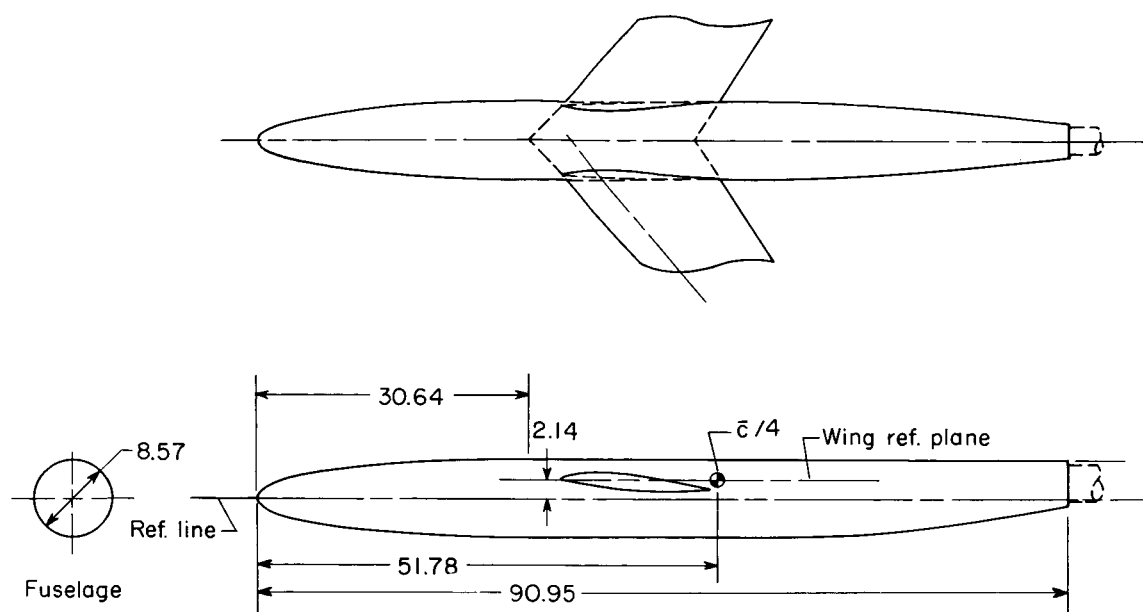
(a) Cylindrical fuselage.
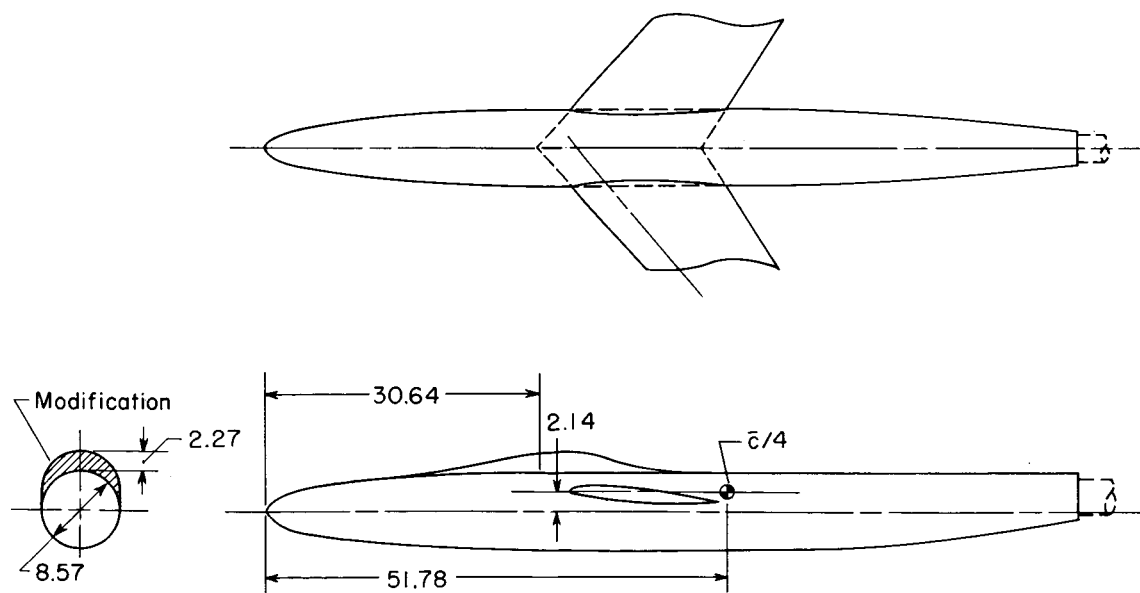
(b) Modified cylindrical fuselage.

Figure 5.- Sketch of cylindrical fuselage and modified cylindrical fuselage. All dimensions in inches.
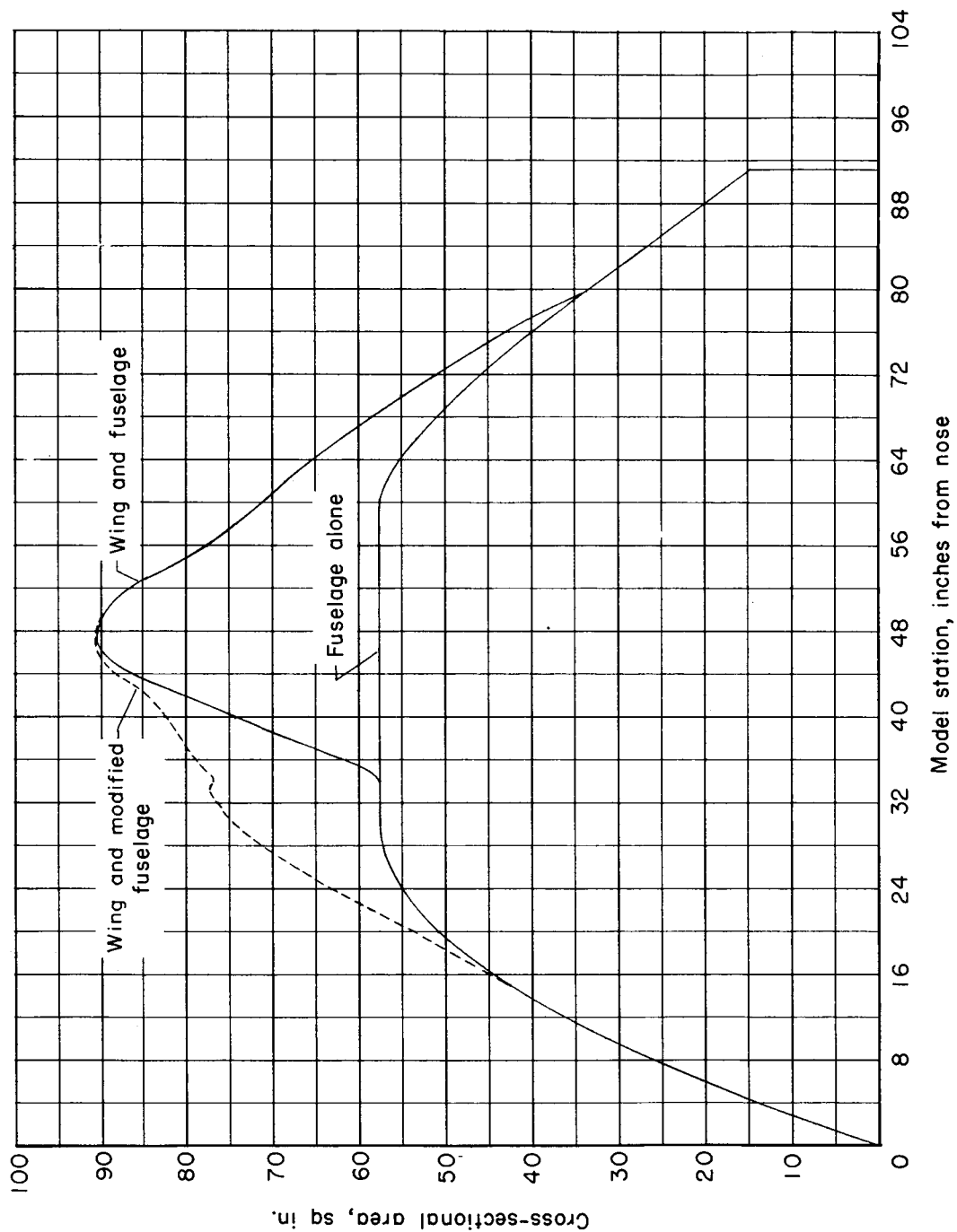
Figure 6.- Cross-sectional-area diagram of cylindrical fuselage and wing in combination with cylindrical fuselage and modified cylindrical fuselage.

L-707
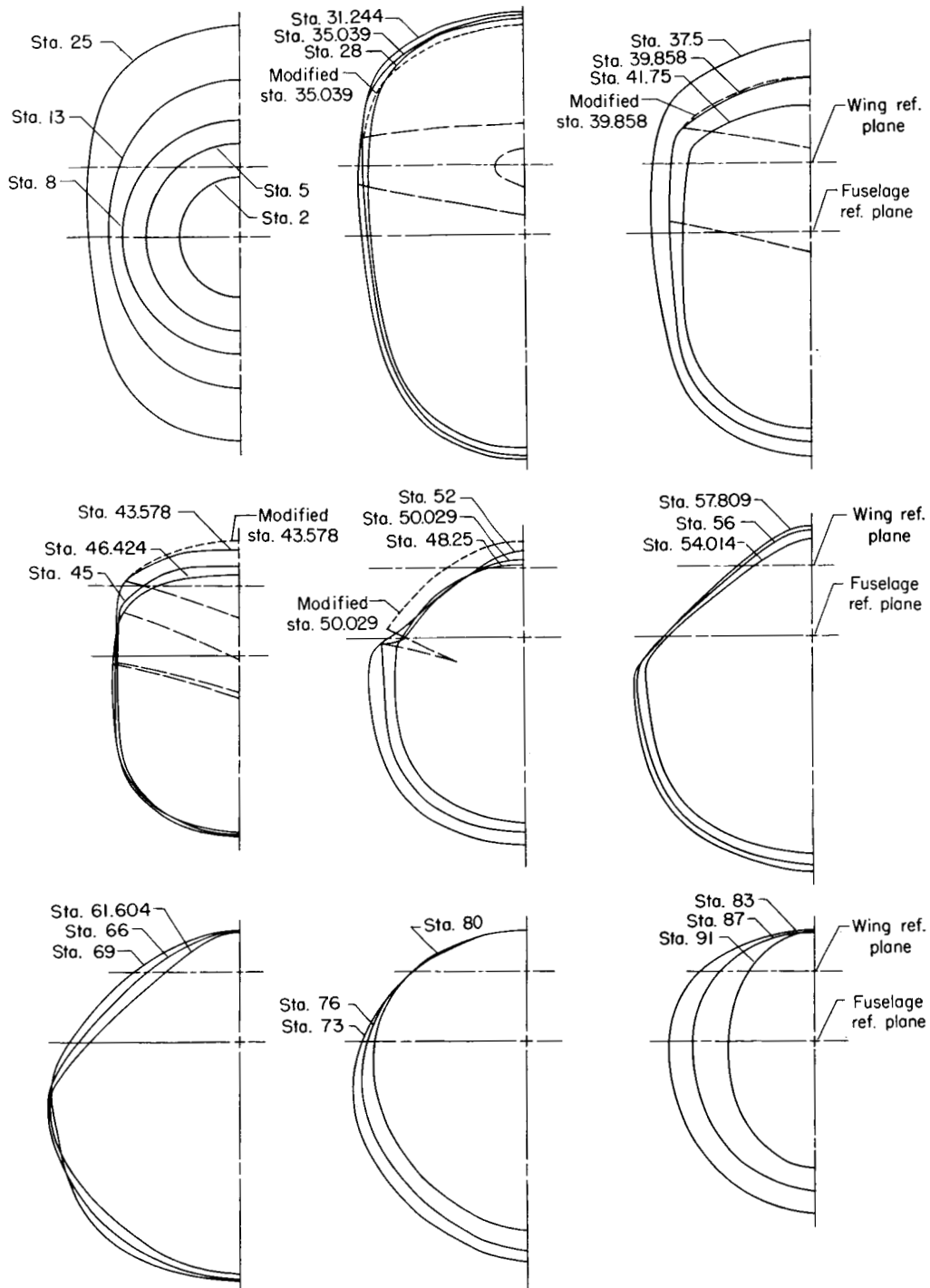
Figure 7.- Cross sections of contoured fuselage and modified contoured fuselage.
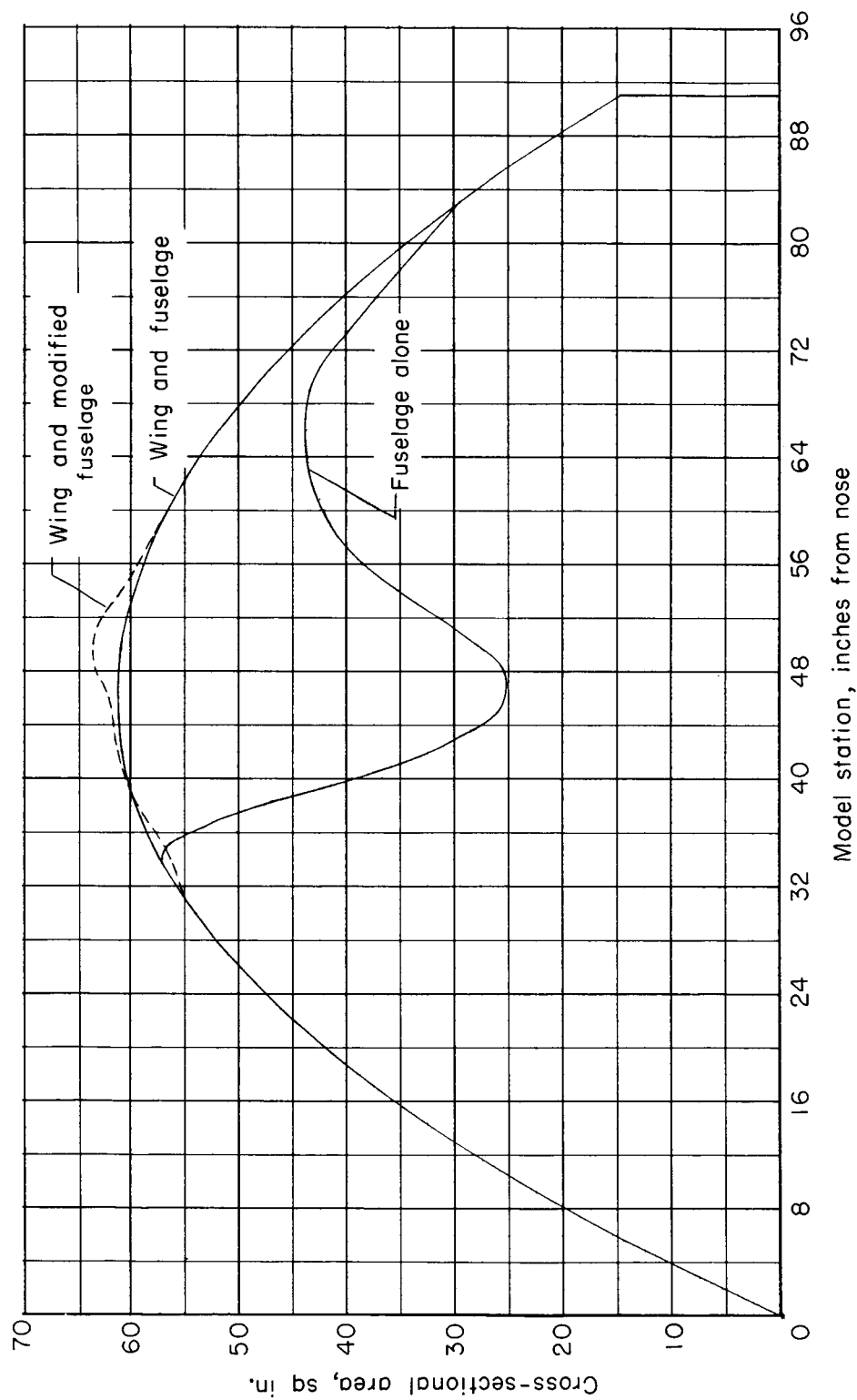
Figure 8.- Cross-sectional-area diagram of contoured fuselage and wing in combination with contoured fuselage and modified contoured fuselage.

Inboard nacelle
Station 16.80

Outboard nacelle
Station 30.00

9.651

Wing reference plane

15°

3.328

1.280

.25

Tubing

9.499

Ȼ parallel to plane of symmetry

3° 15'

1°

Nacelle Ȼ

Pylon Ȼ

Pylon Ȼ

Ȼ parallel to plane of symmetry

1.107
.811
.532
Tubing
Static orifice

45°

Section A-A
Not to scale

45°
Static orifice

Section B-B
Not to scale

EXTERNAL AND INTERNAL
NACELLE COORDINATES

x	R_1	R_2
0.000	0.969	0.963
.053	1.027	.955
.160	1.072	.956
.267	1.105	.957
.534	1.172	.959
1.067	1.263	.964
1.601	1.332	.979
2.134	1.387	1.001
2.668	1.431	1.034
3.201	1.466	1.069
3.733	1.485	1.092
4.268	1.498	1.103
4.797	1.504	1.109
5.335	1.503	1.114
5.632	1.498	1.116
6.144	1.476	1.120
6.656	1.444	1.124
7.168	1.398	1.127
7.680	1.345	1.109
8.192	1.284	1.060
8.704	1.218	.991
9.216	1.149	.924
9.728	1.077	.872
10.240	1.001	.841
10.752	.920	.836
11.213	.845	.836

COORDINATES FOR
OUTBOARD PYLON
CENTERLINE

x_3	y_3
0	-0.047
1	-.056
2	-.065
3	-.070
4	-.070
5	-.062
6	-.052
7	-.036
8	-.017
9	.011
10	.048
11	.088
12	.138
13	.198
14	.263
15	.338
16	.406
17	.472
18	.538
19	.610
20	.670

Figure 9.- Sketches of pylon-mounted nacelles. All dimensions in inches
unless otherwise noted.
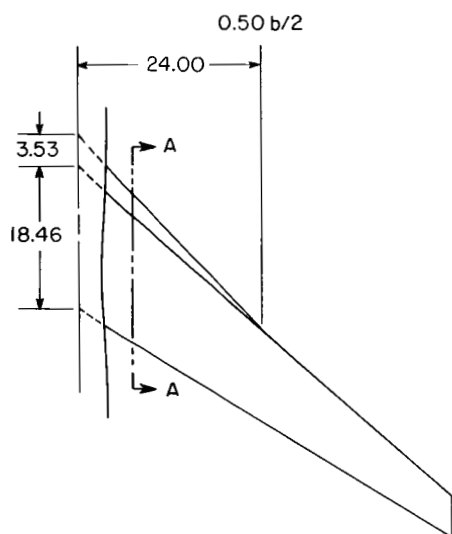
Leading-edge extension I
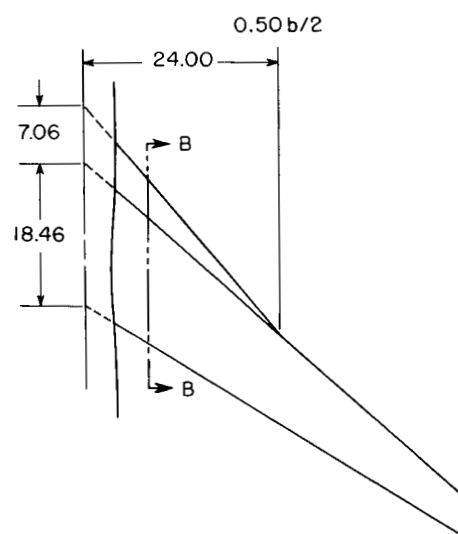
Leading-edge extension II
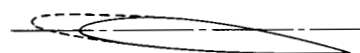
Section A--A
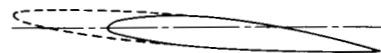
Section B-B
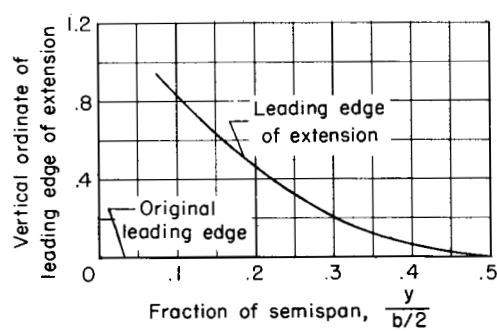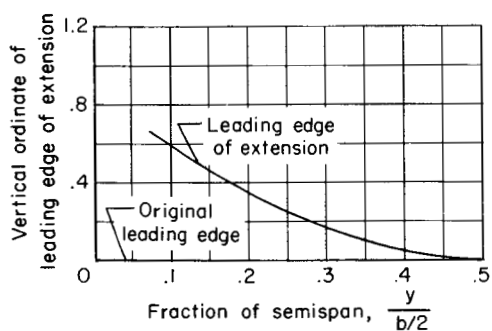
Figure 10.- Sketches of wing leading-edge extensions. All dimensions in inches unless otherwise noted.
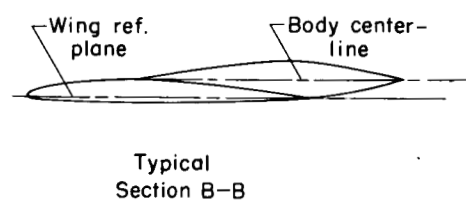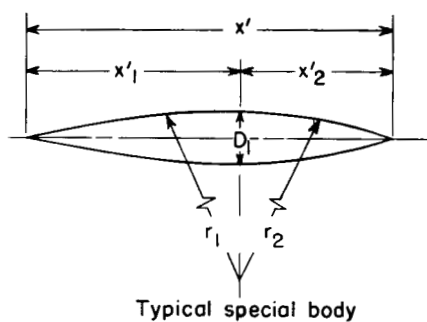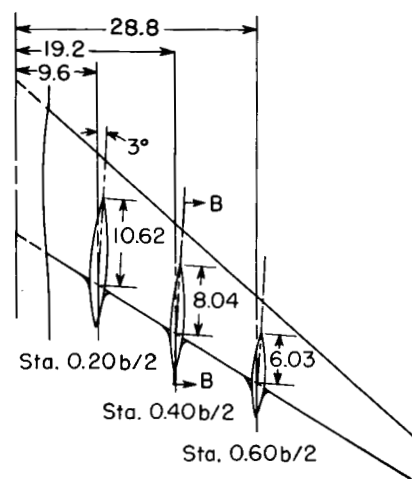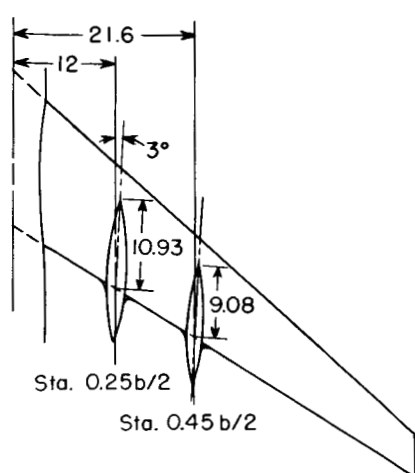
$\frac{y}{b/2}$	D_1	x'	x'_1	x'_2	r_1	r_2
0.20	2.07	16.05	9.83	6.22	47.11	19.17
.40	1.73	12.59	7.38	5.21	31.81	16.07
.60	1.39	9.68	5.49	4.19	21.91	12.91
.25	2.44	17.47	10.16	7.31	42.91	22.51
.45	2.02	14.51	8.44	6.07	35.77	18.75

Figure 11.- Sketches of special wing bodies. All dimensions in inches unless otherwise noted.

16.8

.63

30.0

Wing lower surface

Wing ref. plane

.06

.25c

.70c

Fairing

Section A—A

Wing ridges not to scale
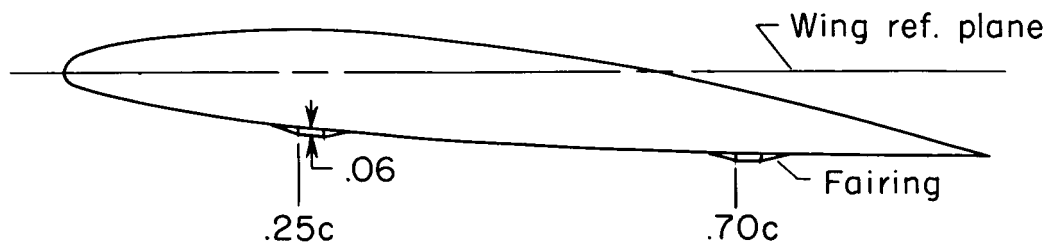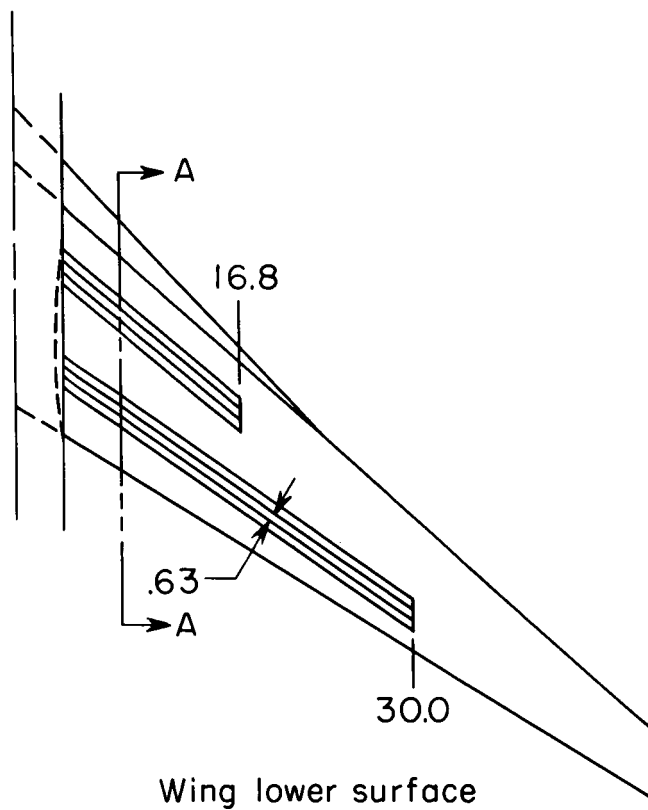
Figure 12.- Sketches of wing lower surface ridges. All dimensions in inches unless otherwise noted.

L-707
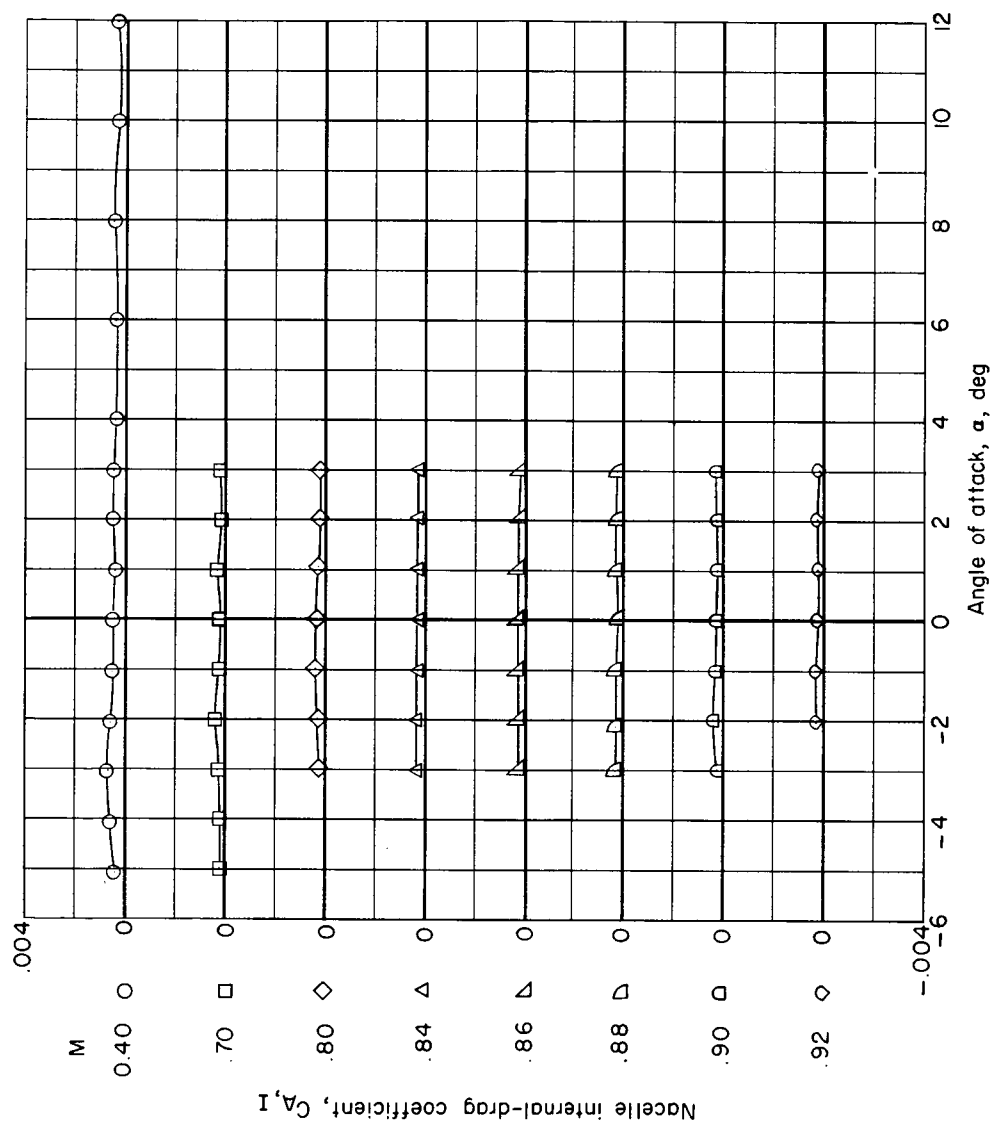
Figure 13.- Variation of nacelle internal-drag coefficient with model angle of attack.
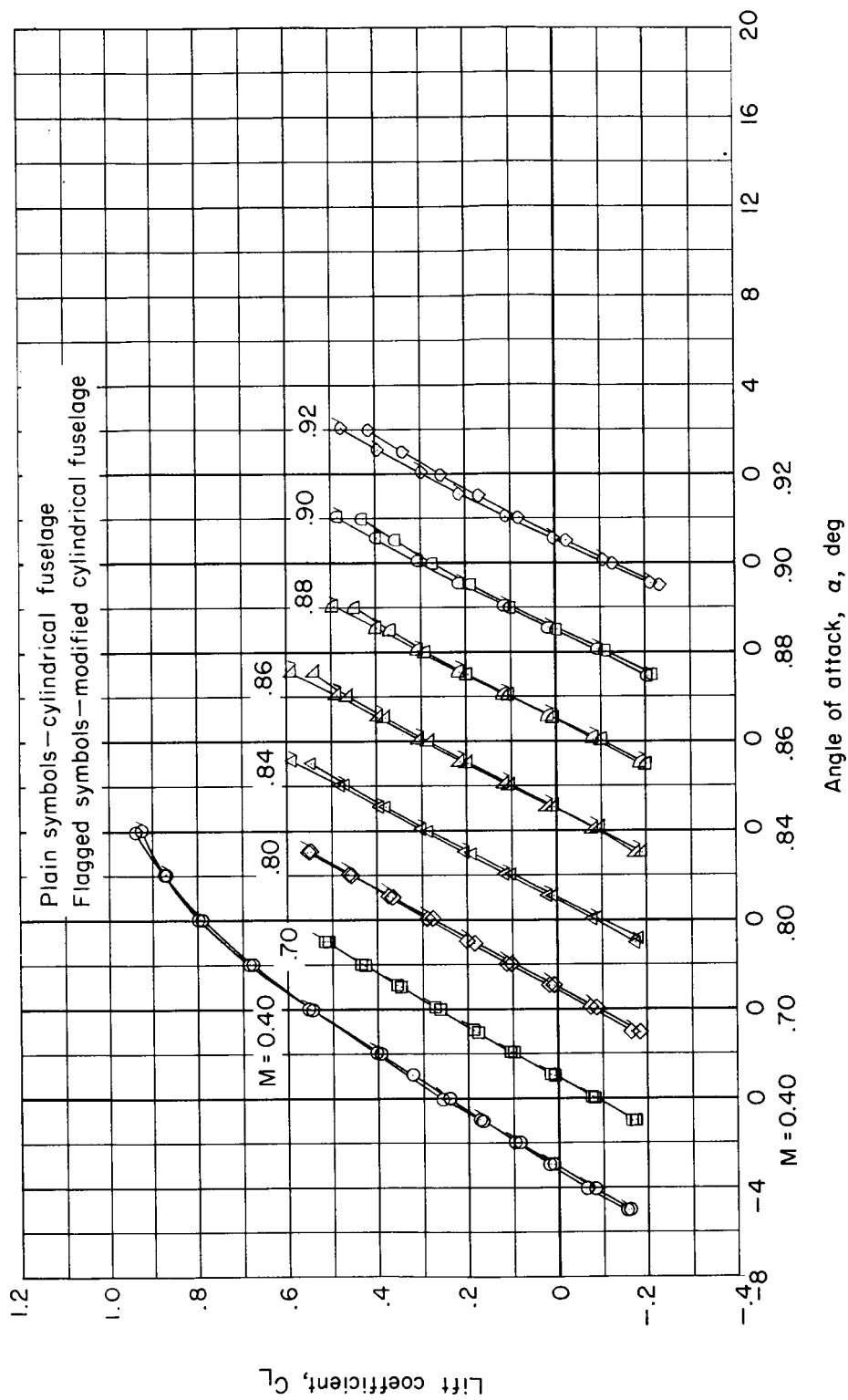
(a) Lift.

Figure 14.- Aerodynamic characteristics of the wing with the cylindrical fuselage and the modified cylindrical fuselage.

L-707

L-707
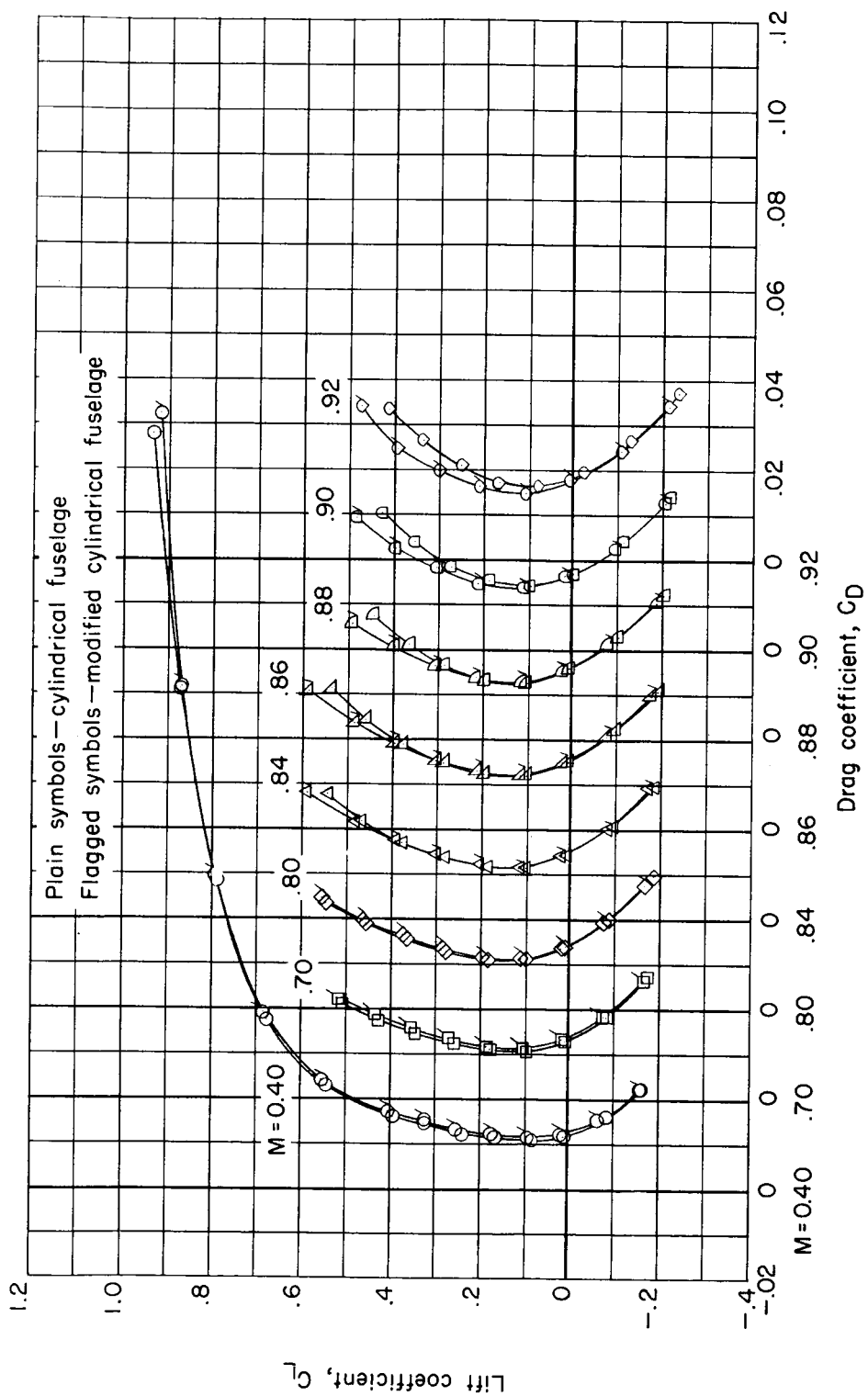
(b) Drag.

Figure 14.- Continued.
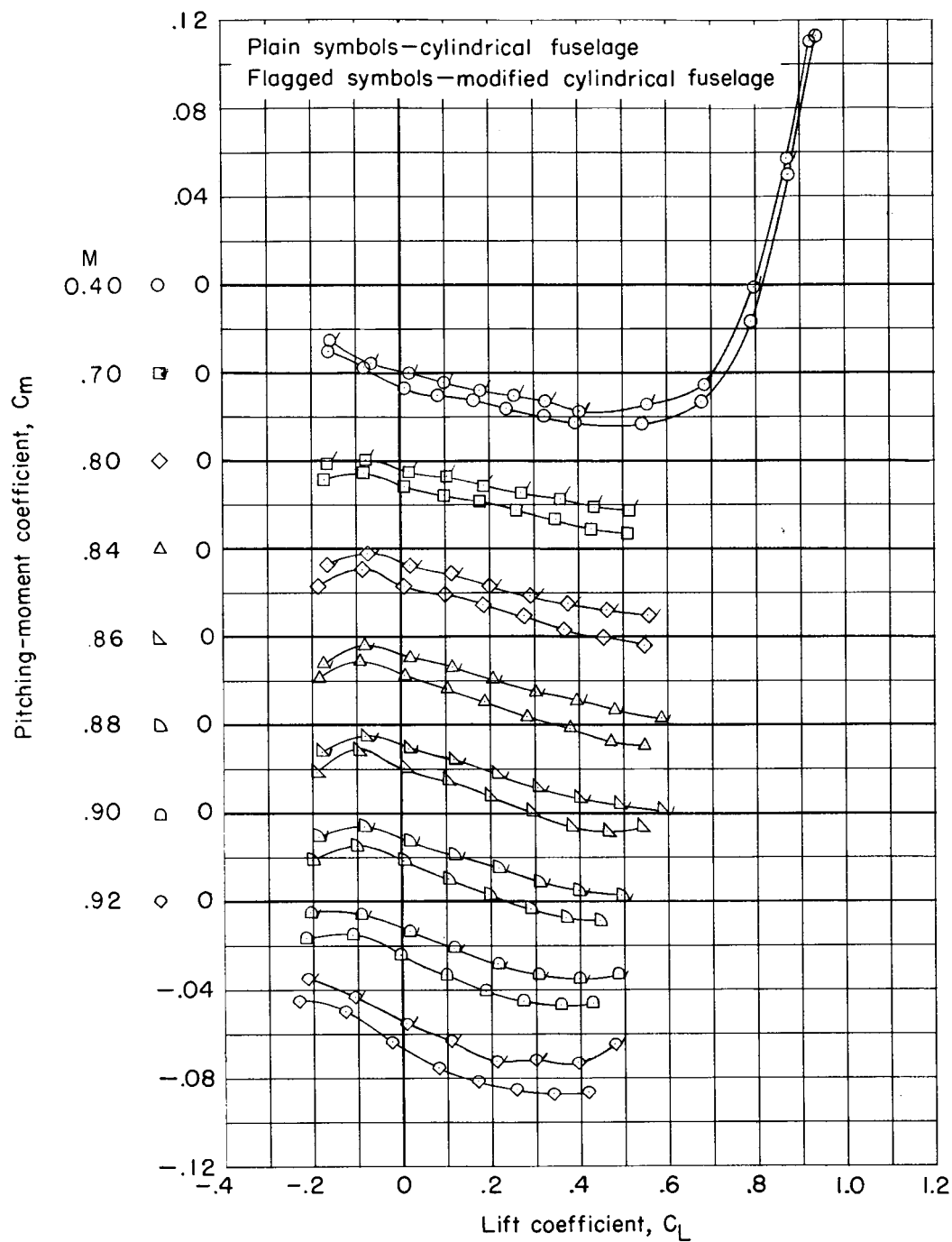
(c) Pitching moment.

Figure 14.- Concluded.

L-707
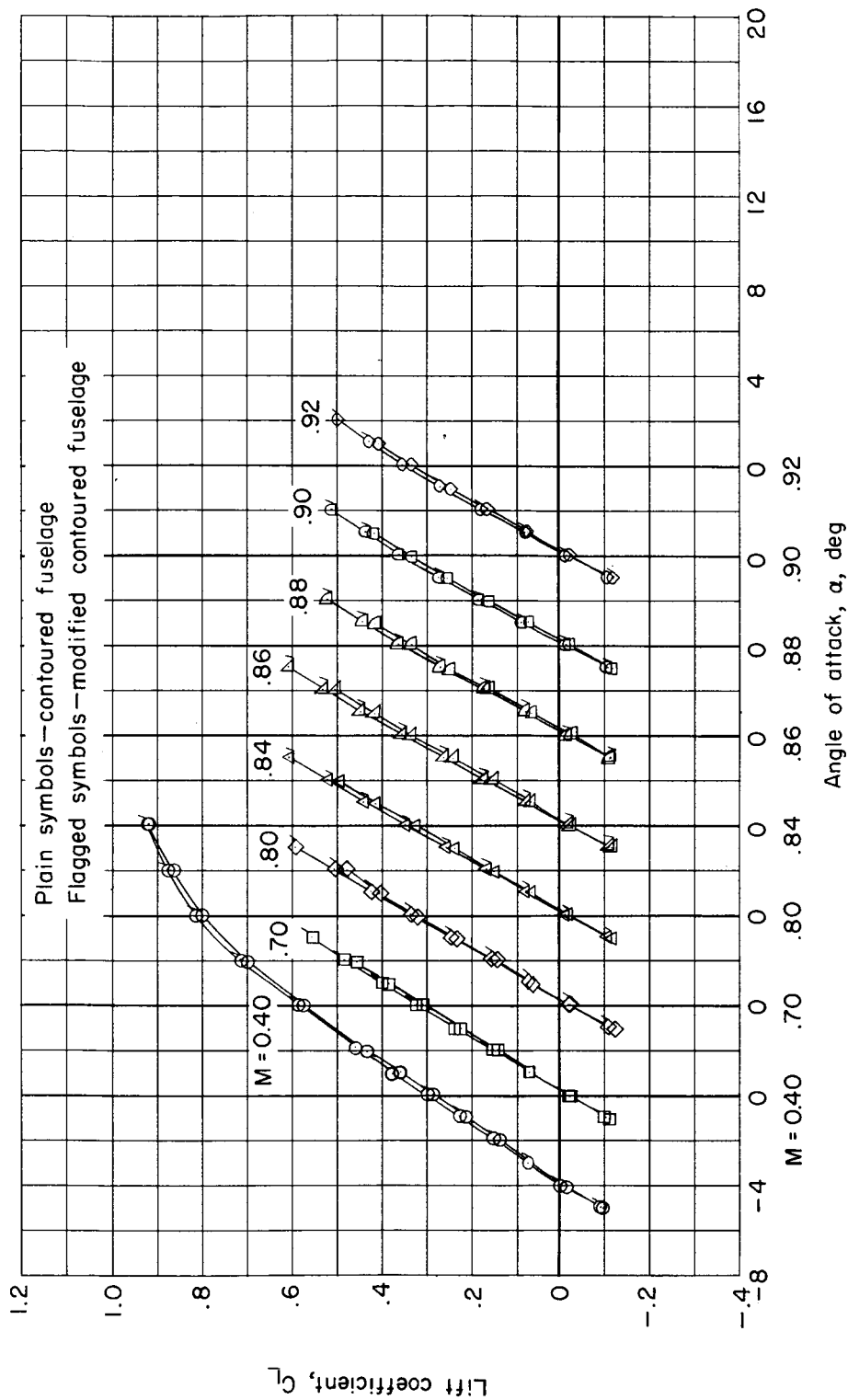
(a) Lift.

Figure 15.- Aerodynamic characteristics of the wing with the contoured fuselage and the modified contoured fuselage.
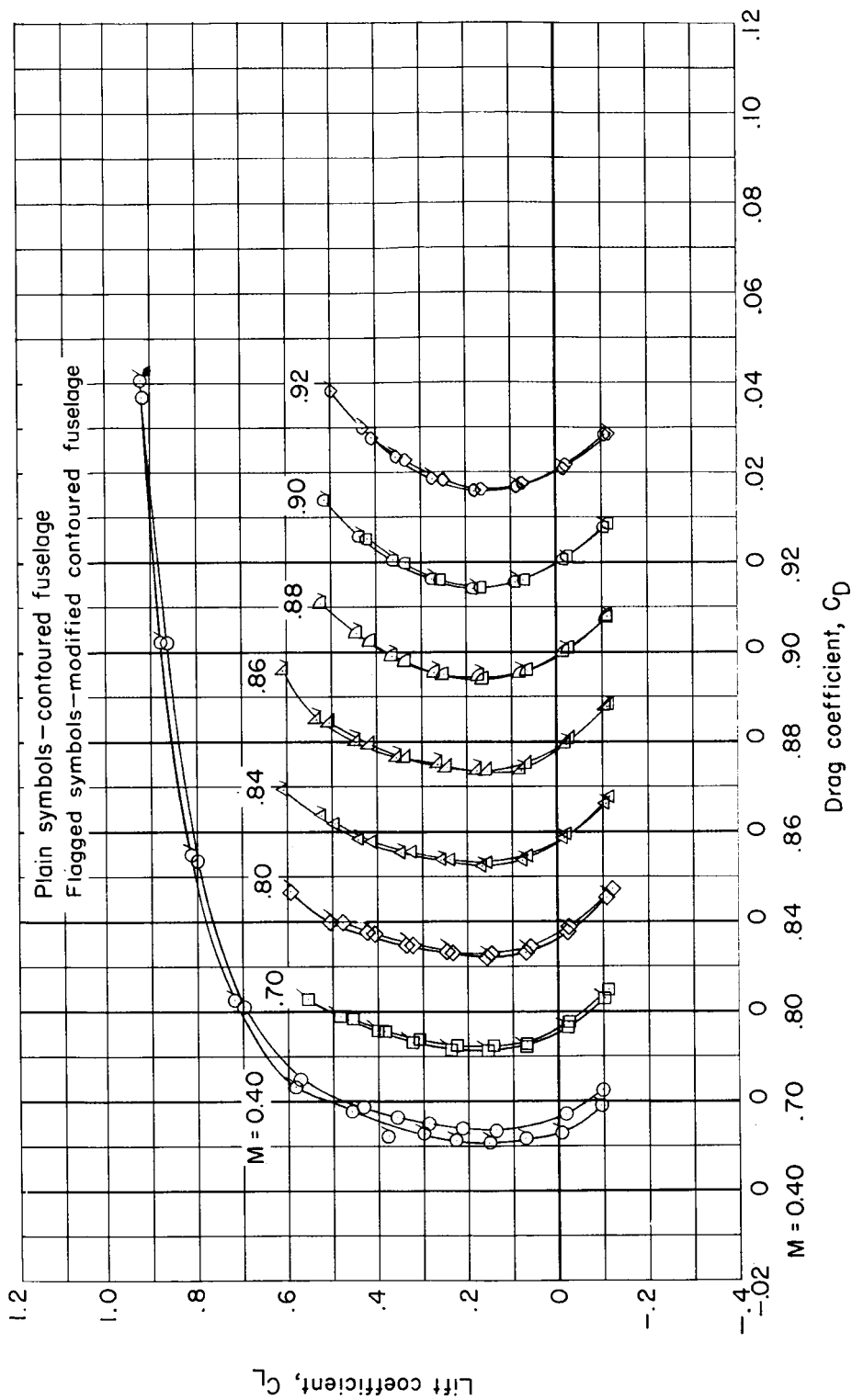
(b) Drag.

Figure 15.- Continued.
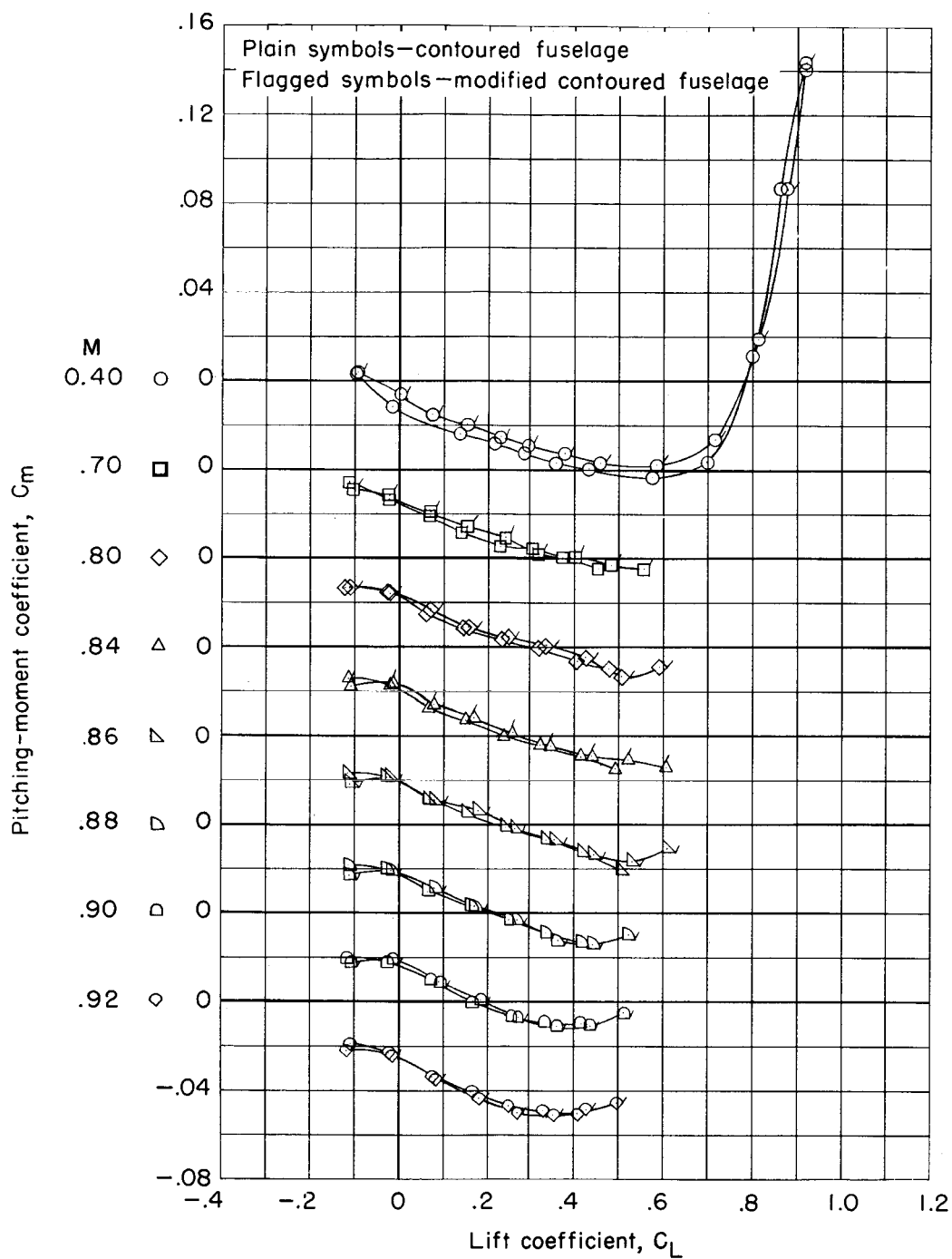
(c) Pitching moment.

Figure 15.- Concluded.
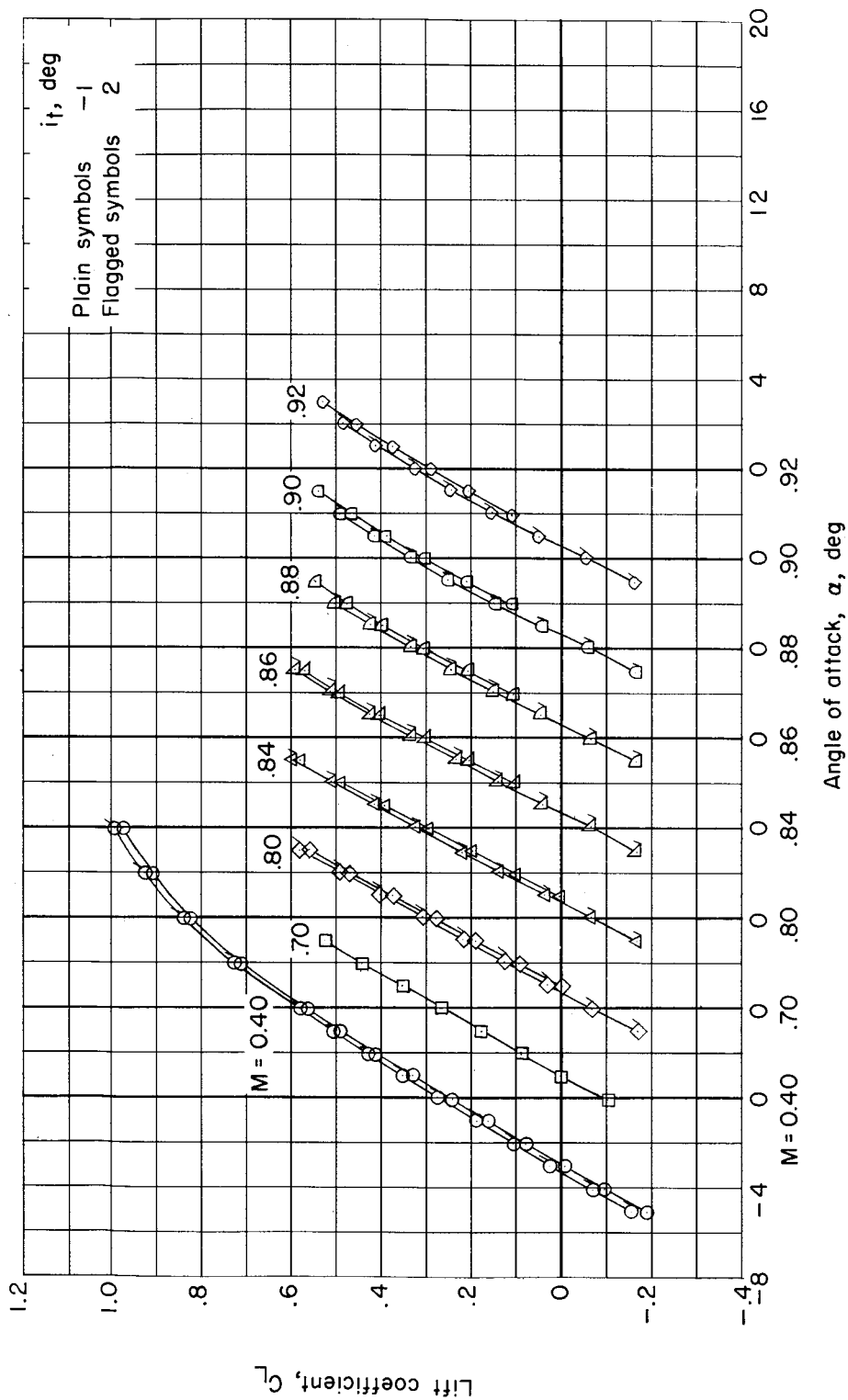
(a) Lift.

Figure 16.- Aerodynamic characteristics of the wing with the modified contoured fuselage with the vertical tail and with the horizontal tail at two incidences.

L-707
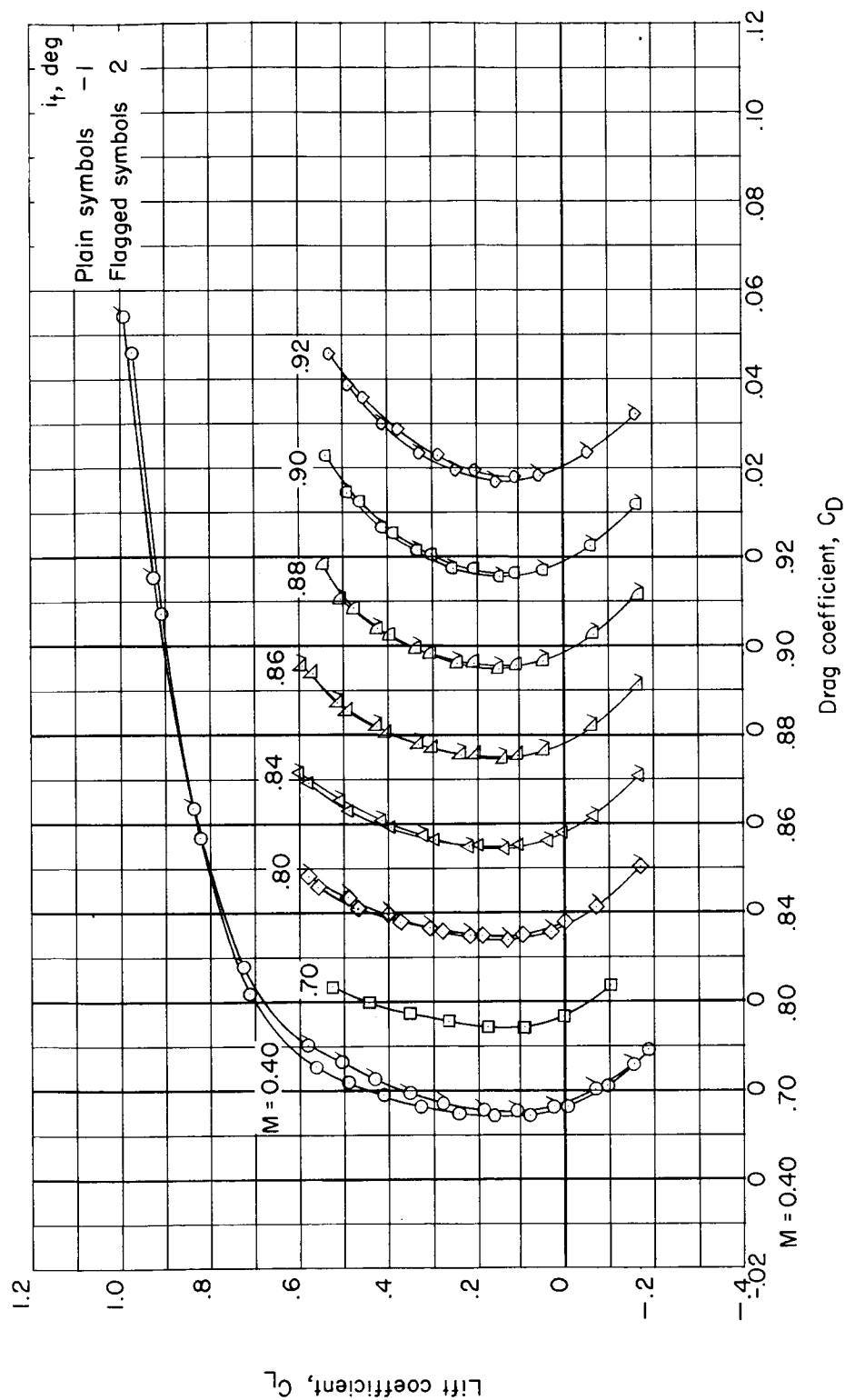
(b) Drag.

Figure 16.- Continued.
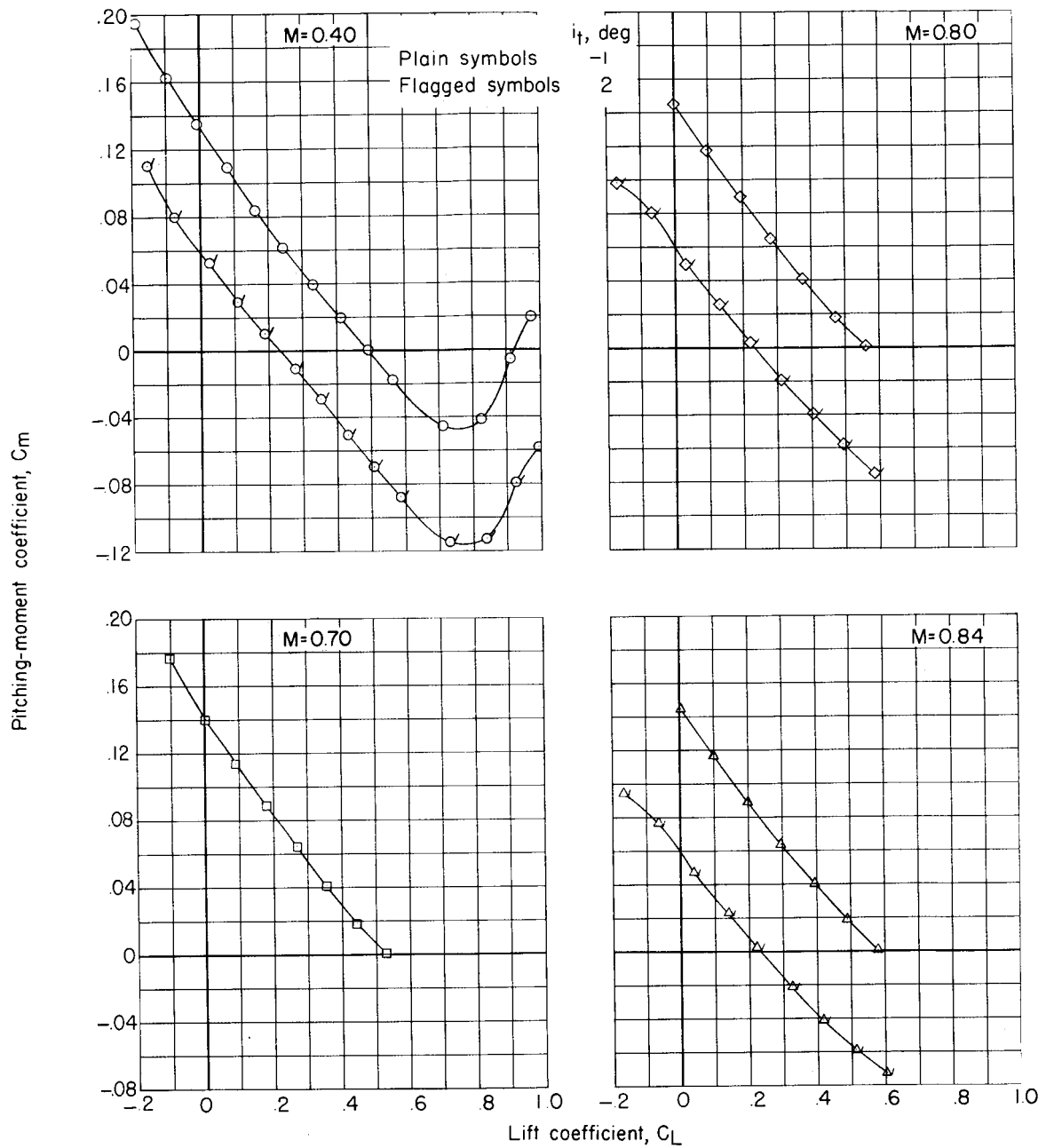
(c) Pitching moment.

Figure 16.- Continued.
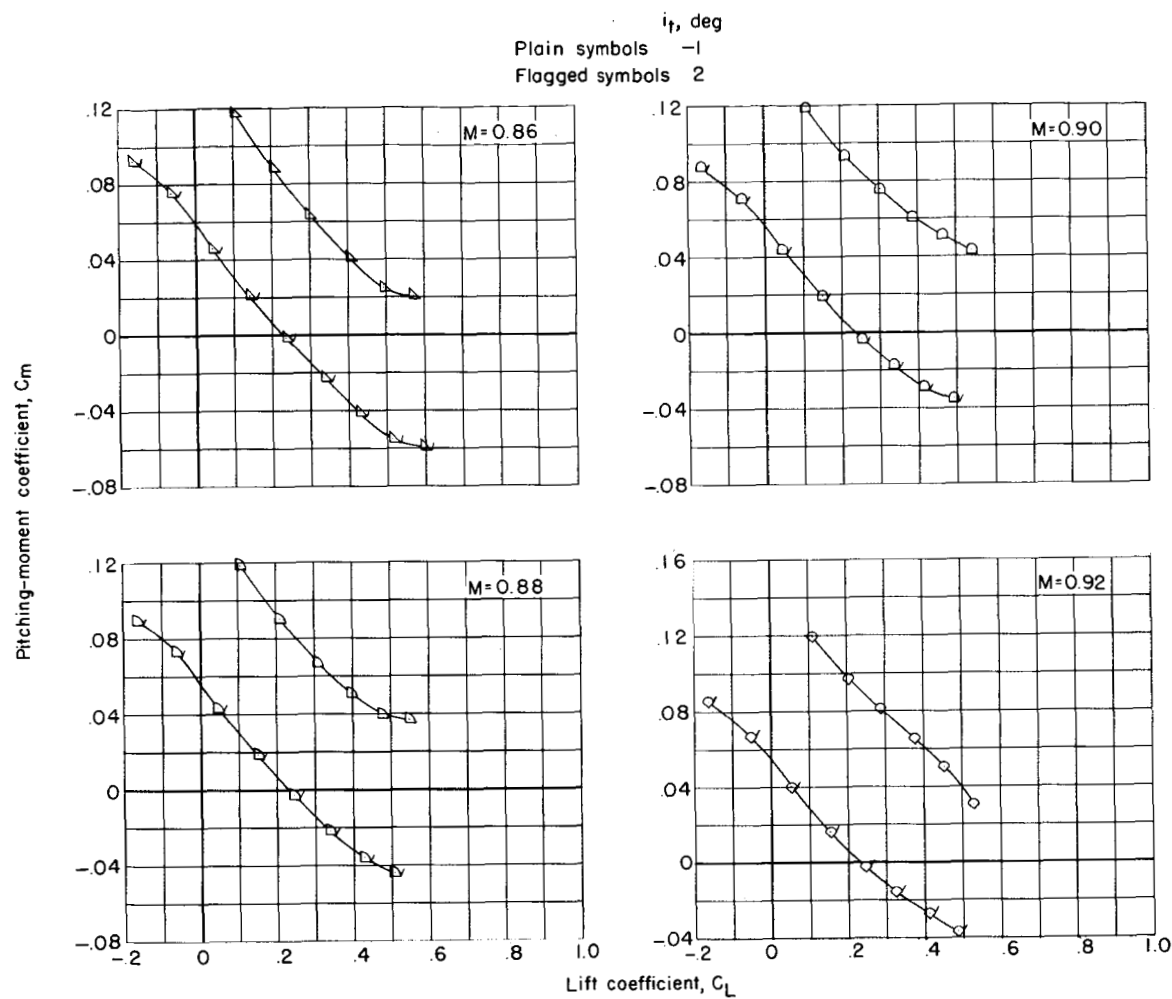
(c) Concluded.

Figure 16.- Concluded.

Lift coefficient, C_L

Plain symbols—complete configuration

Flagged symbols—four special wing bodies (nacelles removed)

M = 0.40

M = 0.40   .70   .80   .84   .86   .88   .90   .92   .94   .96

Angle of attack, α, deg
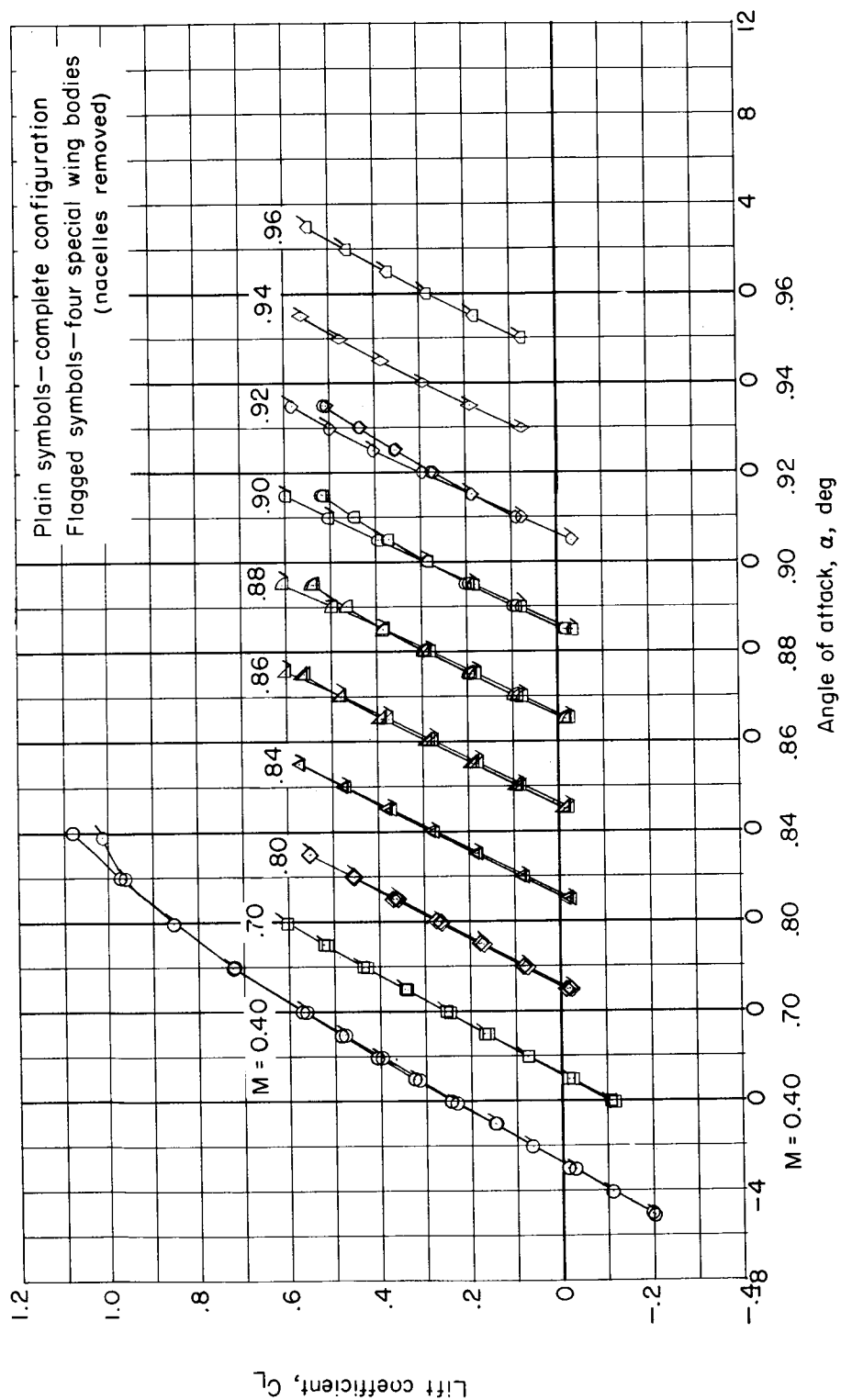
(a) Lift.

Figure 17.- Aerodynamic characteristics of the complete configuration and the configuration with four special wing bodies; each configuration has the modified contoured fuselage and empennage, $i_t = -1°$.

(b) Drag.

Figure 17.- Continued.

45
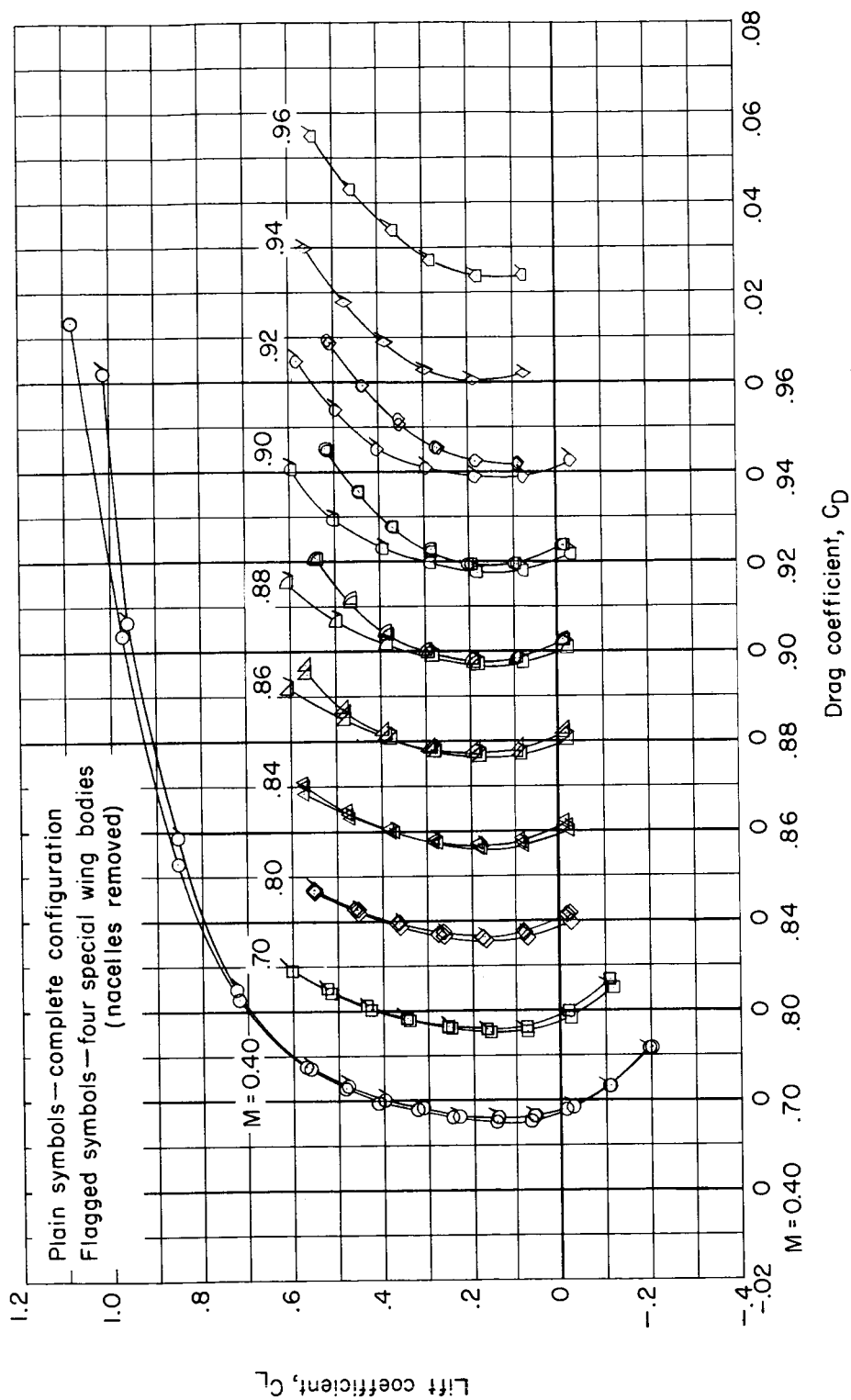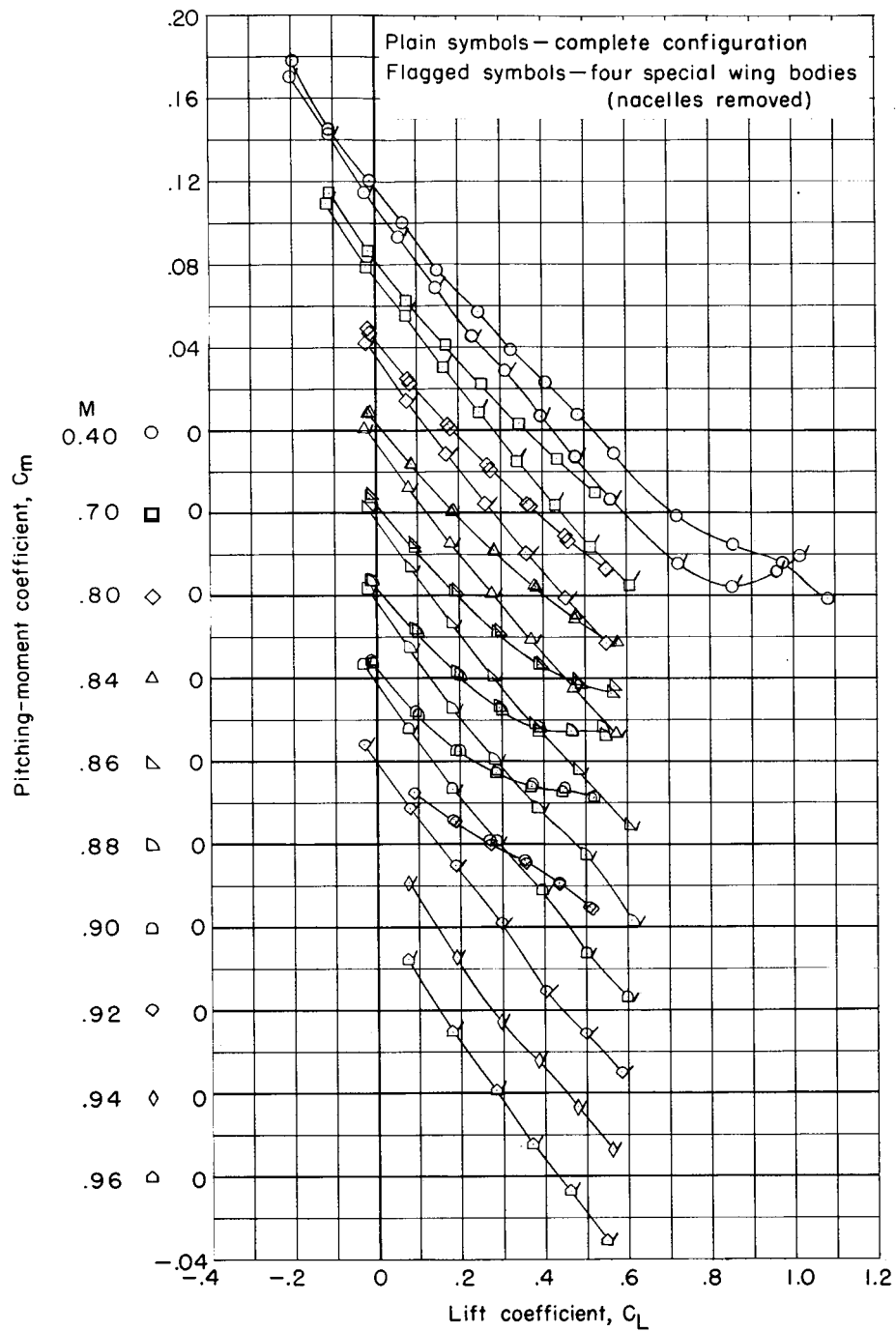
(c) Pitching moment.

Figure 17.- Concluded.
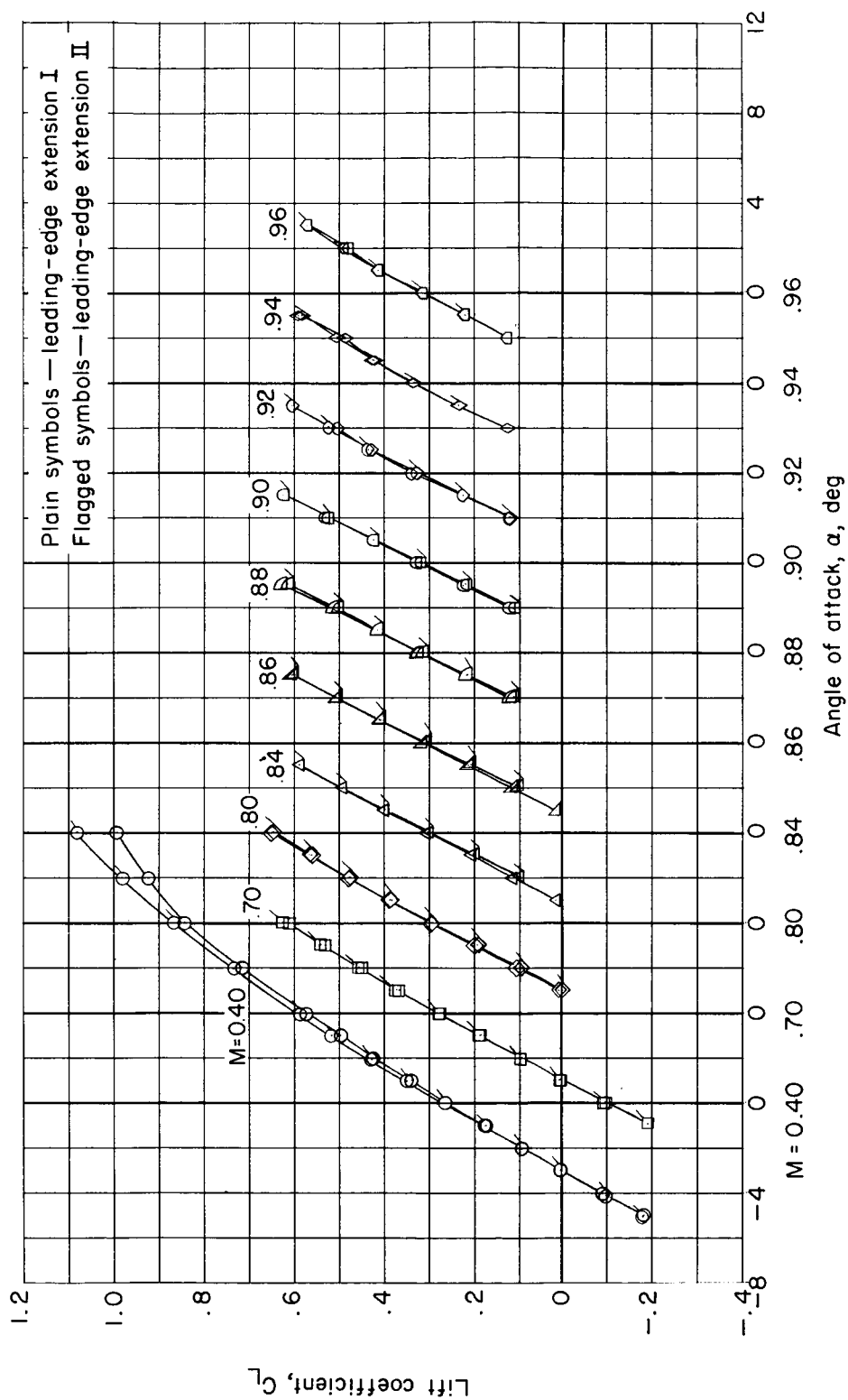
(a) Lift.

Figure 18.- Aerodynamic characteristics of wing with leading-edge extensions in combination with modified contoured fuselage, vertical tail, and horizontal tail at $i_t = -1°$.

47

Plain symbols—leading-edge extension I
Flagged symbols—leading-edge extension II

Drag coefficient, C_D

Lift coefficient, C_L
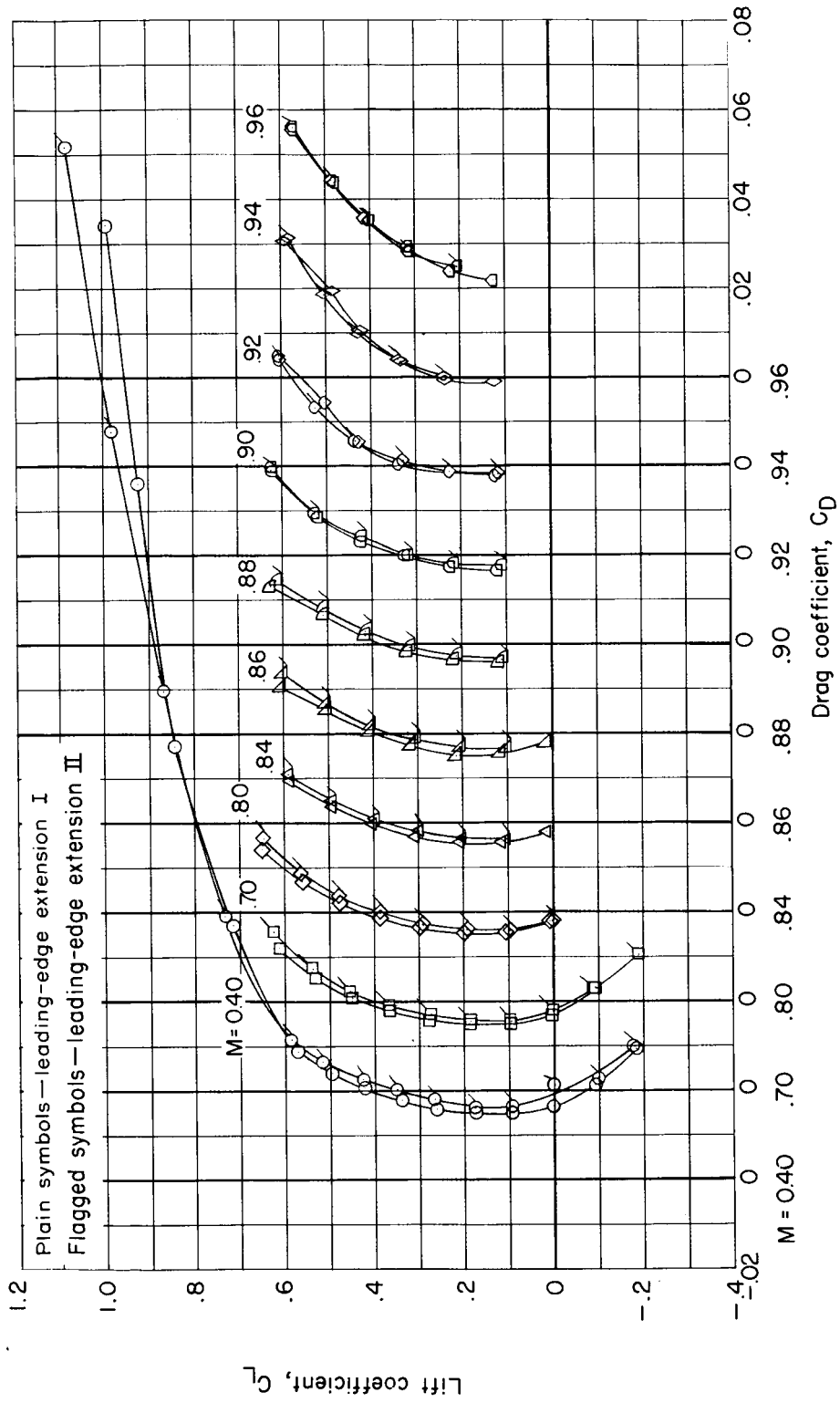
(b) Drag.

Figure 18.- Continued.

L-707
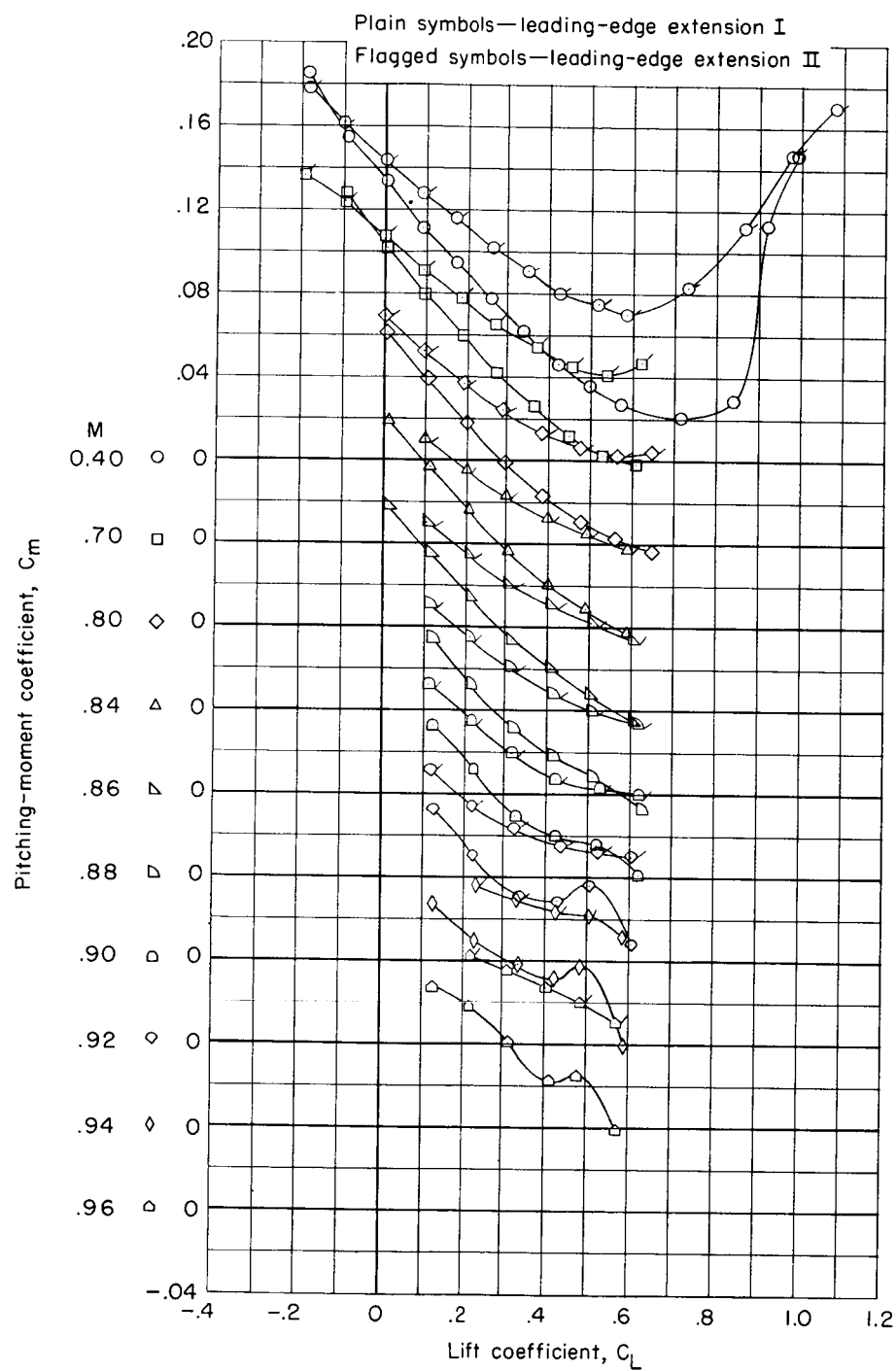
(c) Pitching moment.

Figure 18.- Concluded.
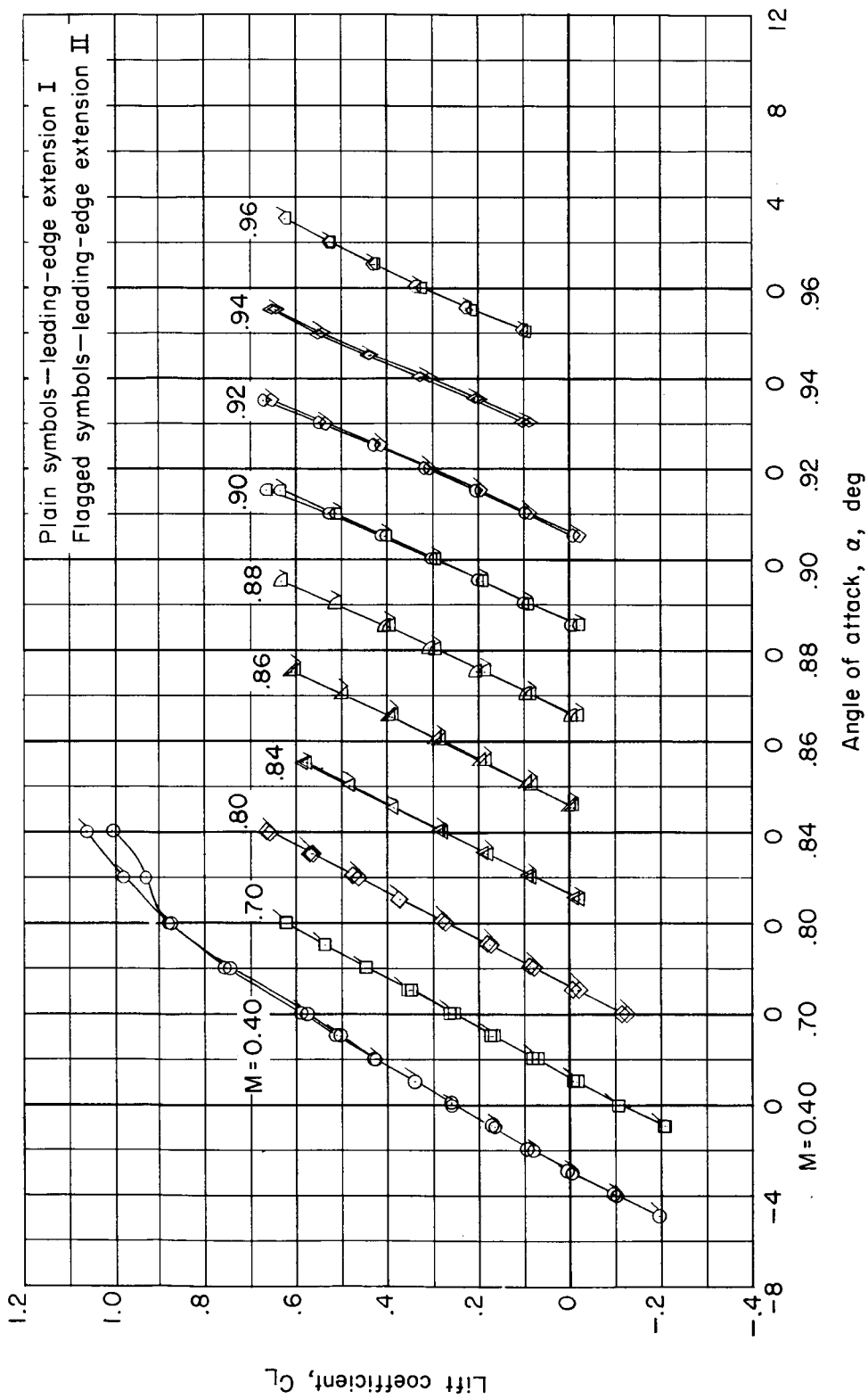
(a) Lift.

Figure 19.- Aerodynamic characteristics of wing with leading-edge extensions and six special wing bodies in combination with modified contoured fuselage, vertical tail, and horizontal tail at $i_t = -1°$.

L-707

L-707

Plain symbols—leading-edge extension I

Flagged symbols—leading-edge extension II

Lift coefficient, C_L

Drag coefficient, C_D
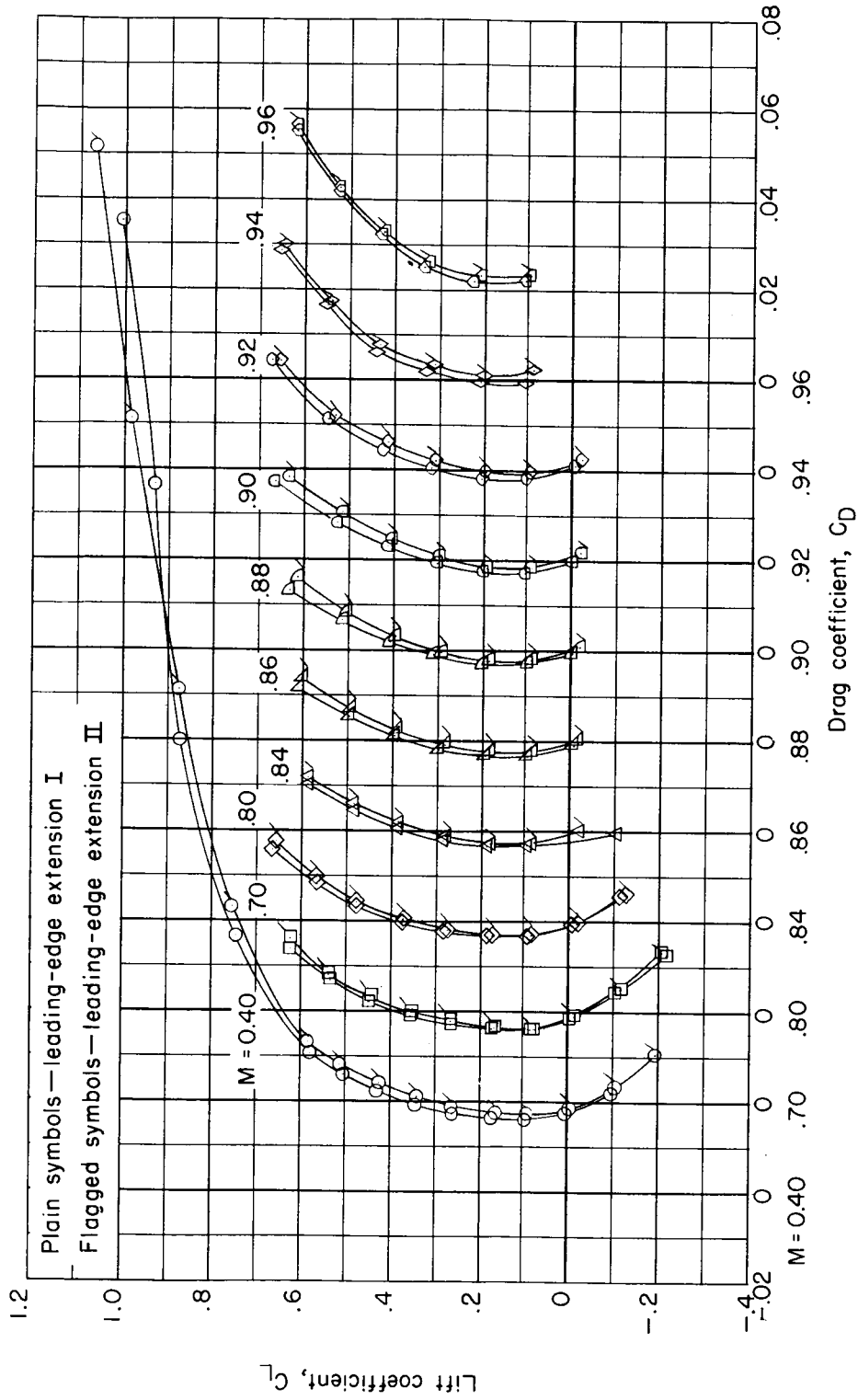
(b) Drag.

Figure 19.- Continued.
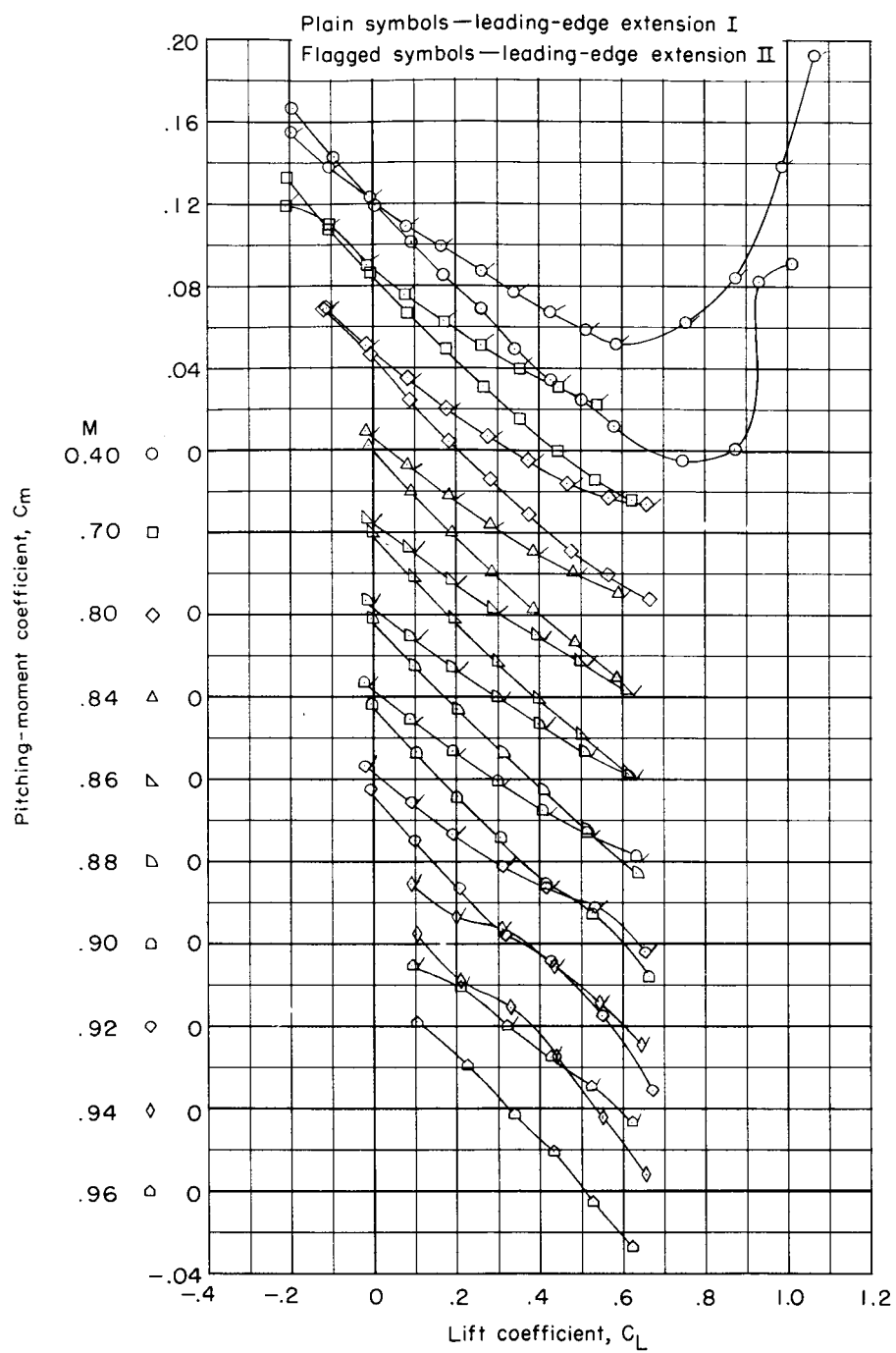
(c) Pitching moment.

Figure 19.- Concluded.
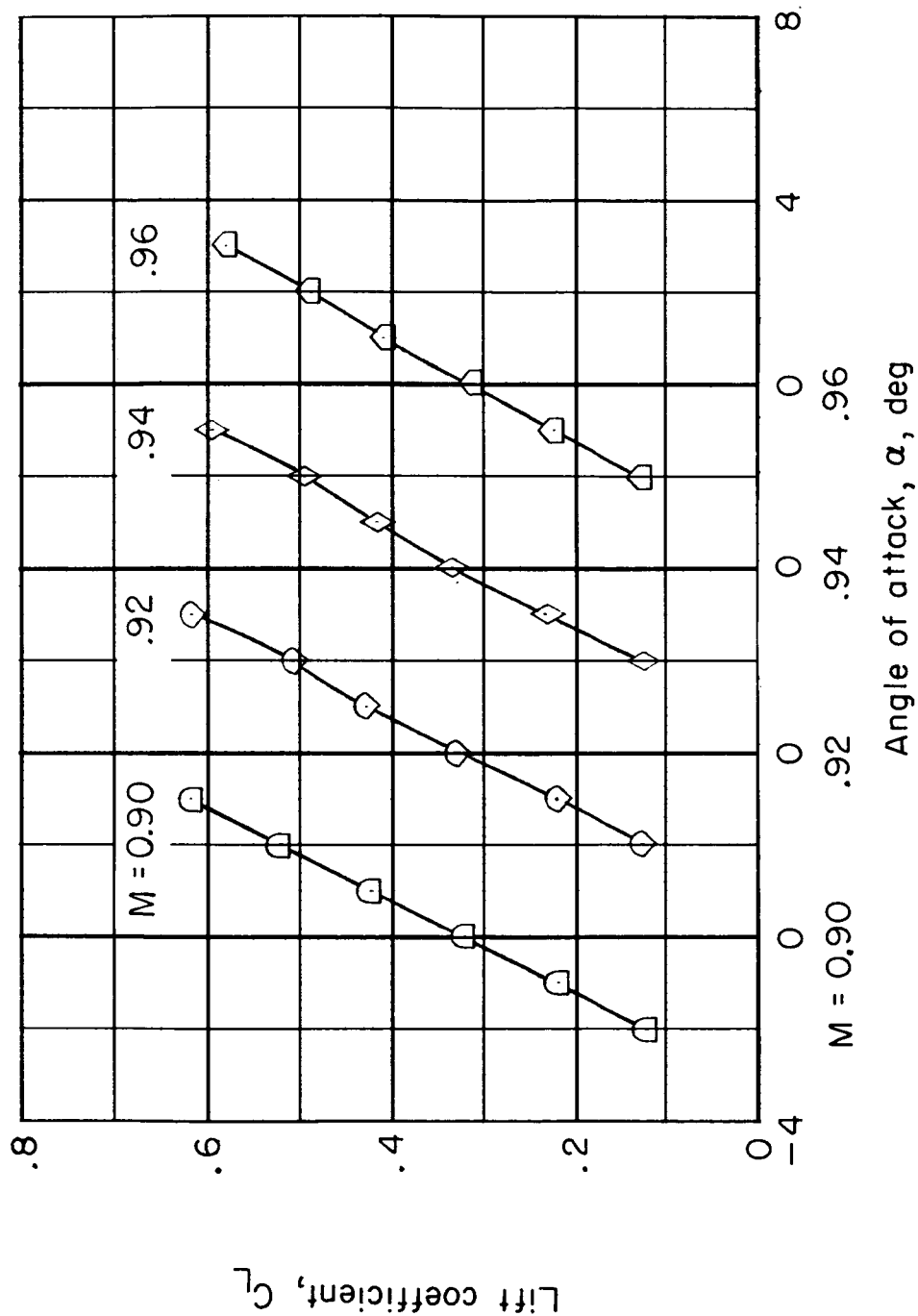
(a) Lift.

Figure 20.- Aerodynamic characteristics of the configuration with wing lower surface ridges. The wing with leading-edge extension I was used with the modified contoured fuselage, vertical tail, and horizontal tail at $i_t = -1°$.
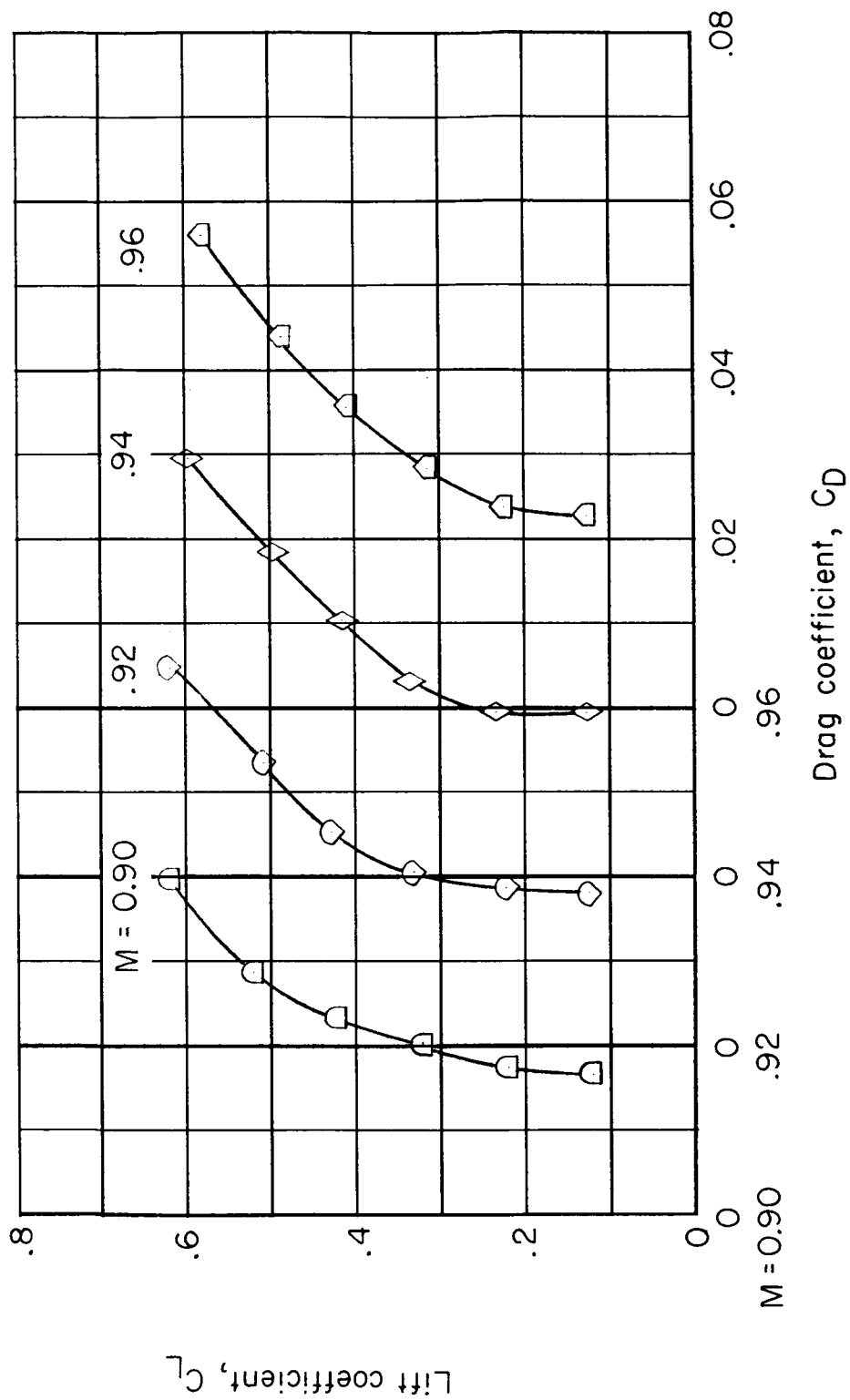
Figure 20.- Continued.

(b) Drag.
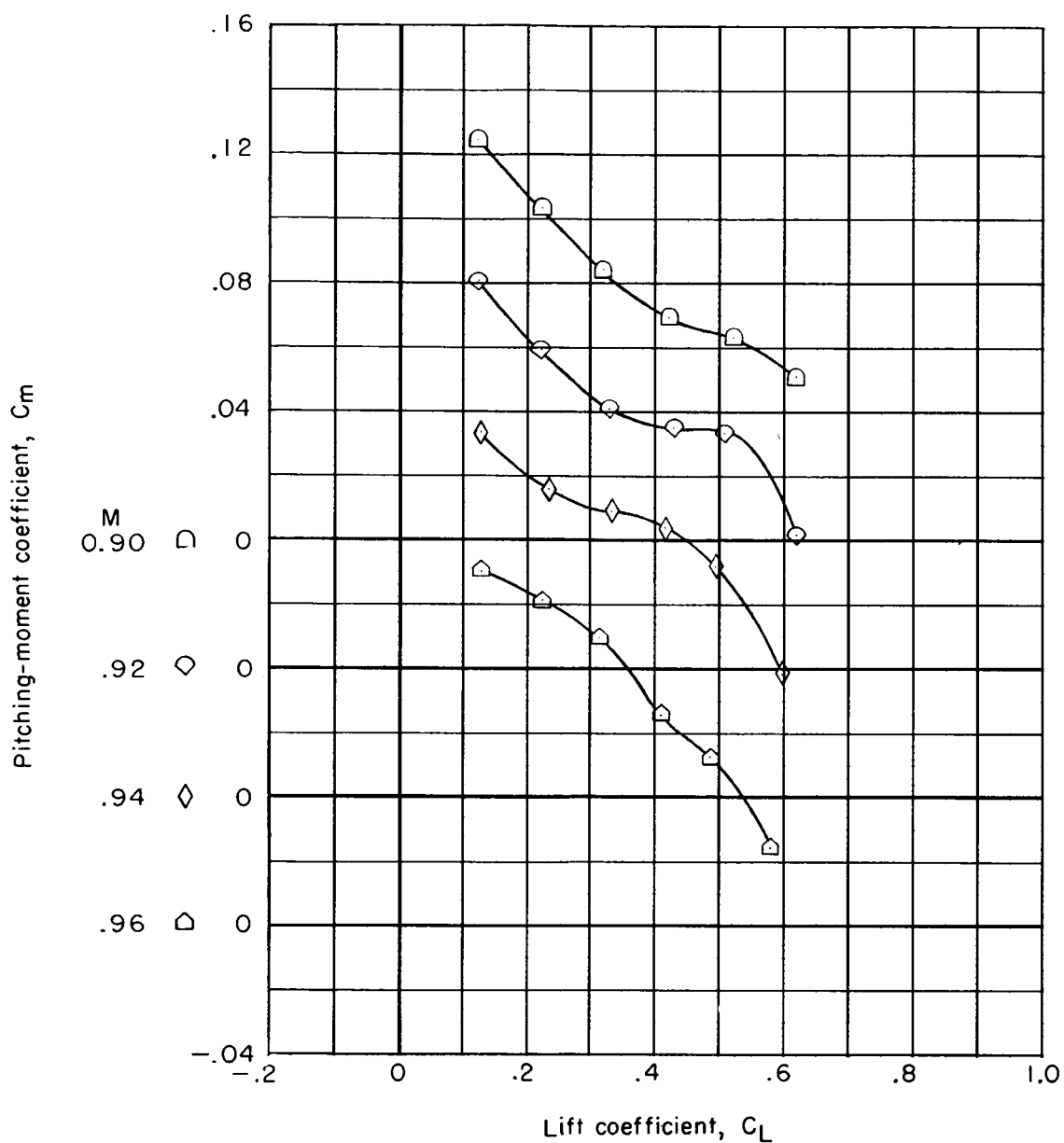
(c) Pitching moment.

Figure 20.- Concluded.
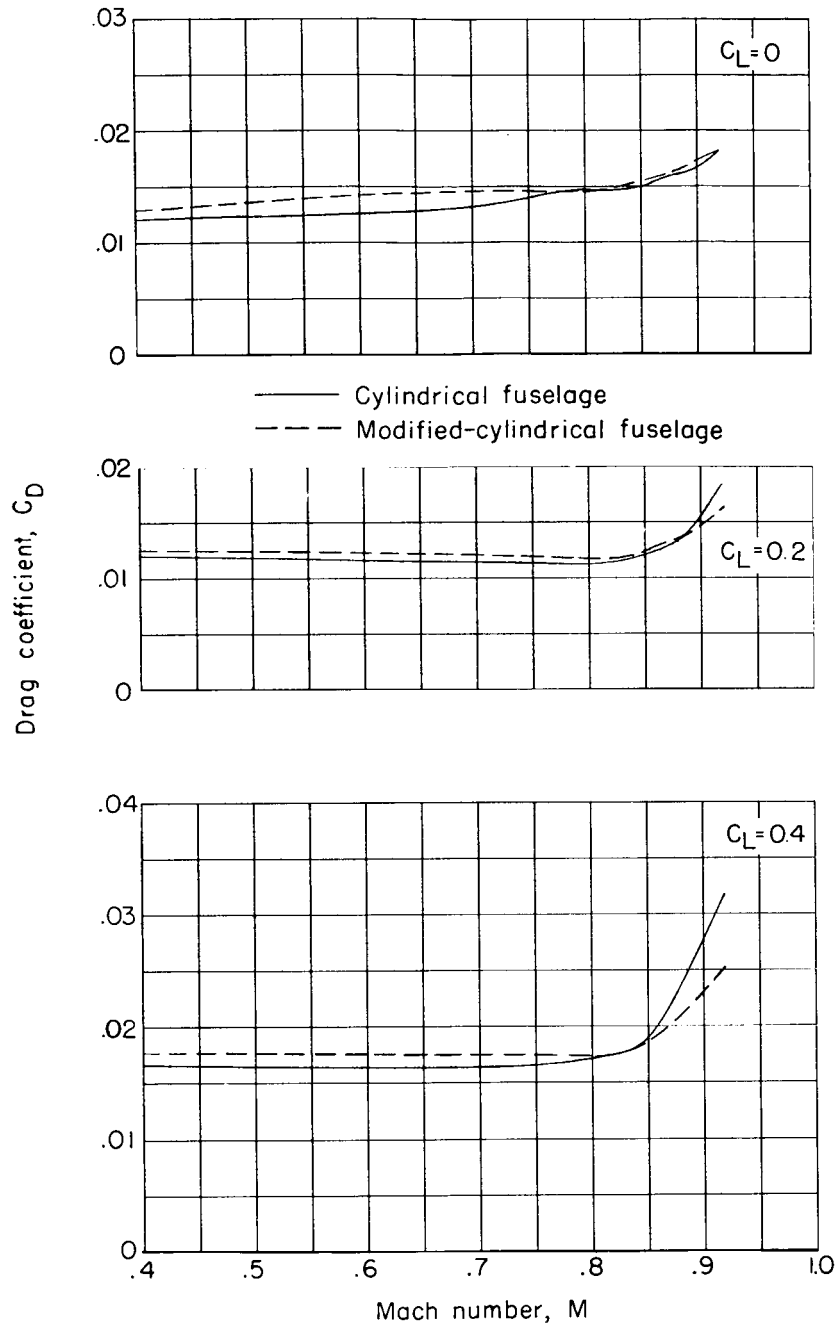
(a) Cylindrical fuselage.

Figure 21.- Variations of drag coefficient with Mach number for the various wing-fuselage configurations.

L-707

Drag coefficient, C_D

Mach number, M
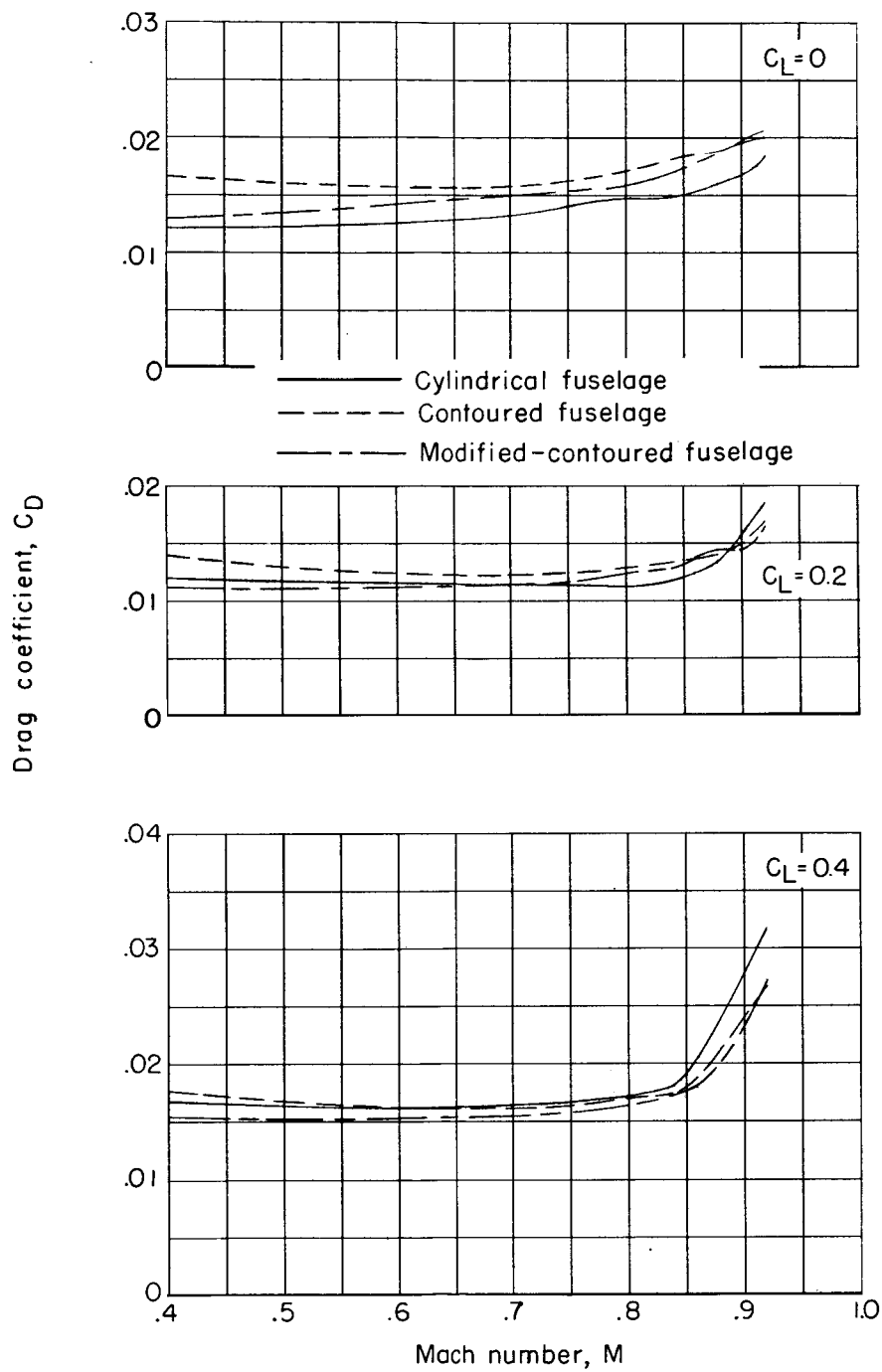
(b) Cylindrical and contoured fuselages.

Figure 21.- Concluded.
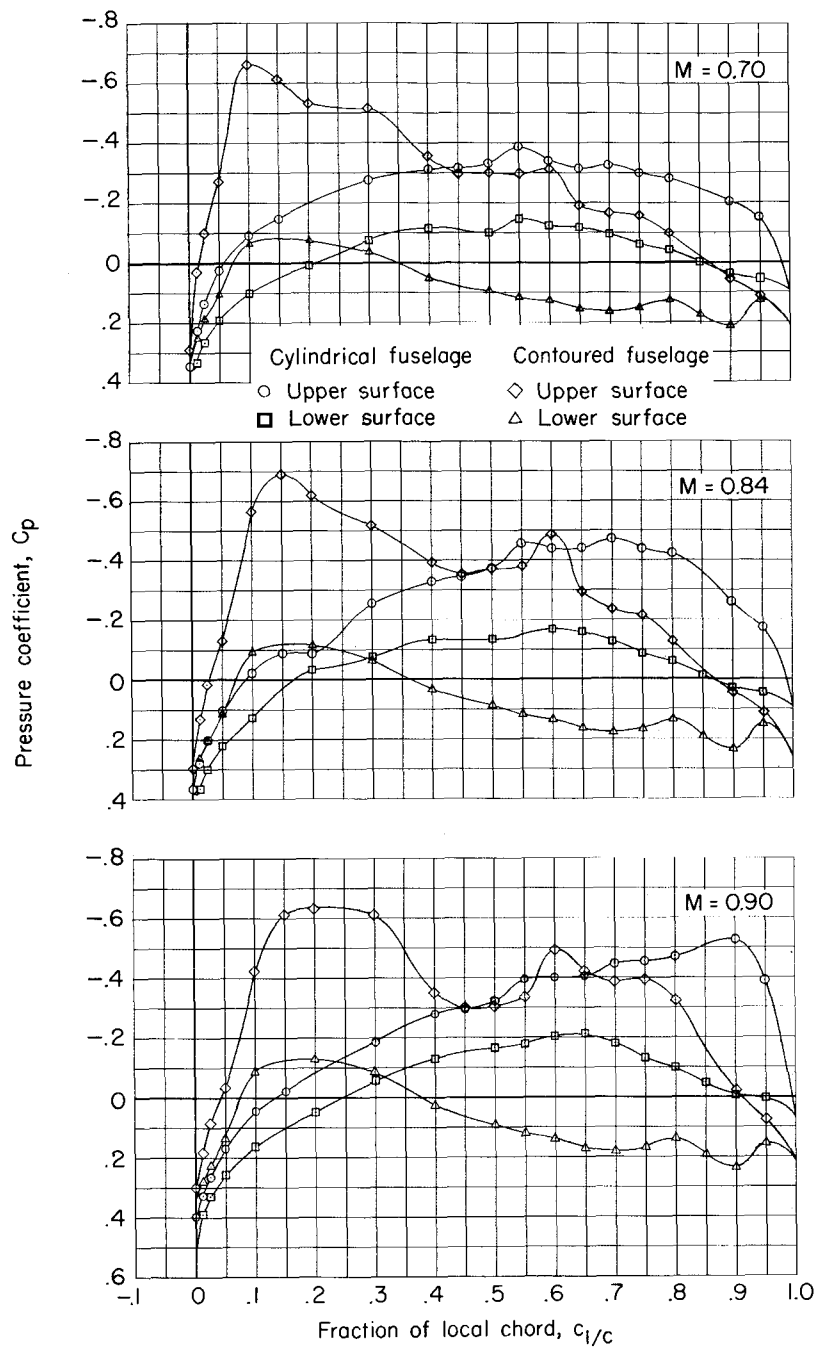
(a) Cylindrical and contoured fuselages.

Figure 22.- Pressure distributions at the wing-fuselage juncture for the cylindrical and contoured fuselages, $\alpha = 0^\circ$.
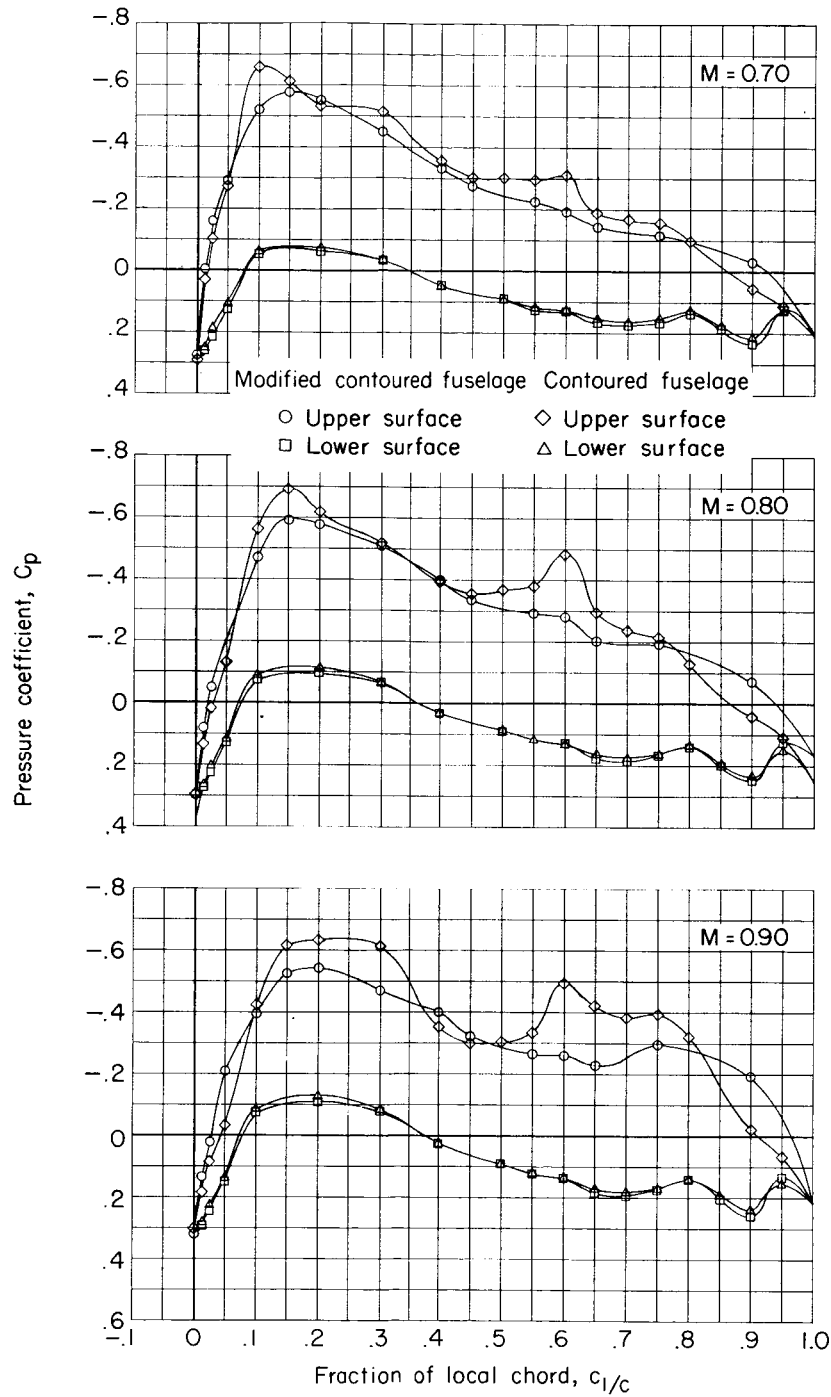
(b) Contoured and modified contoured fuselages.

Figure 22.- Concluded.

Figure 23.- Fluorescent oil film on upper surface of plain wing in combination with modified contoured fuselage for $M = 0.90$, $\alpha = 0°$, and $C_L = 0.34$.

L-59-6480

L-707
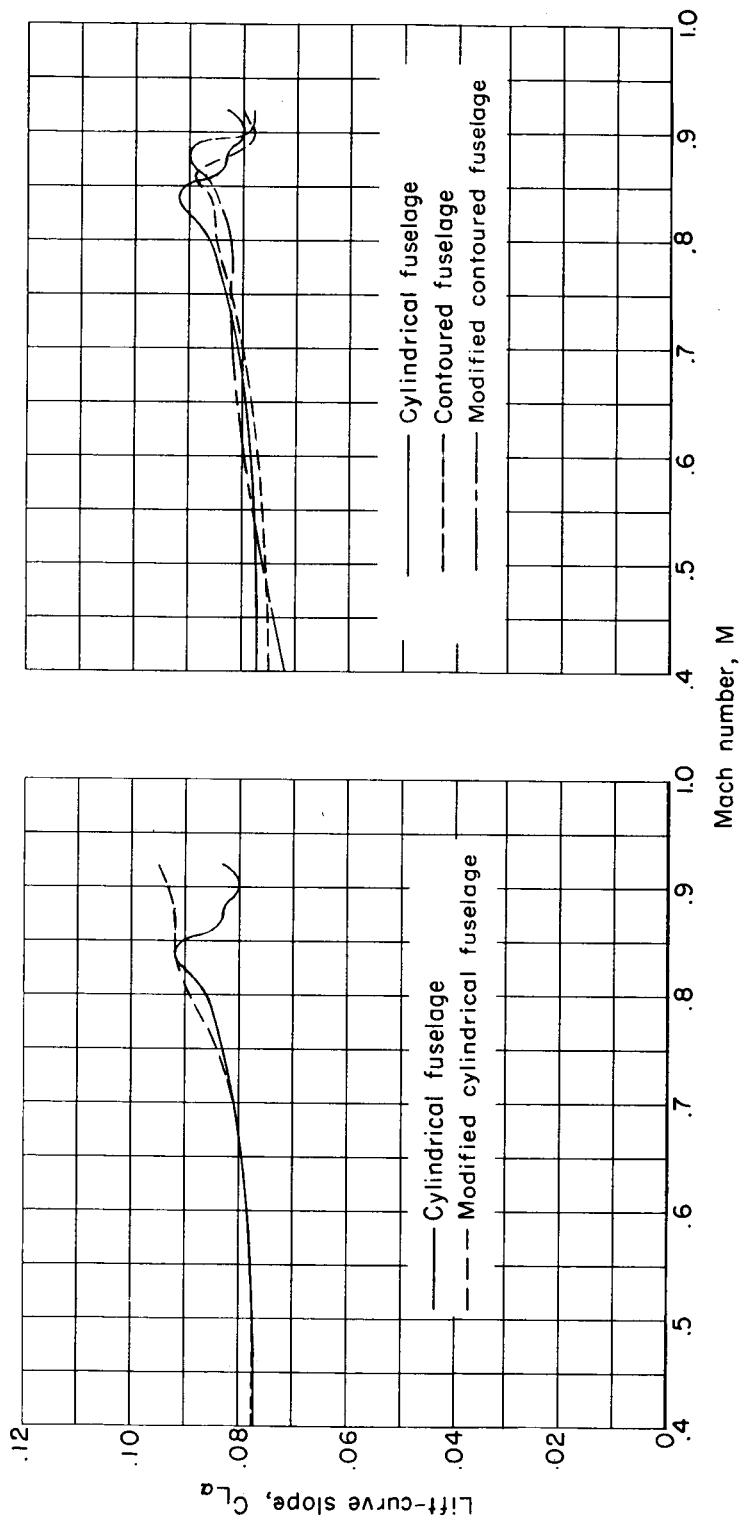
Figure 24.- Variation of lift-curve slope with Mach number at $\alpha = 0°$ for the various wing-fuselage combinations.
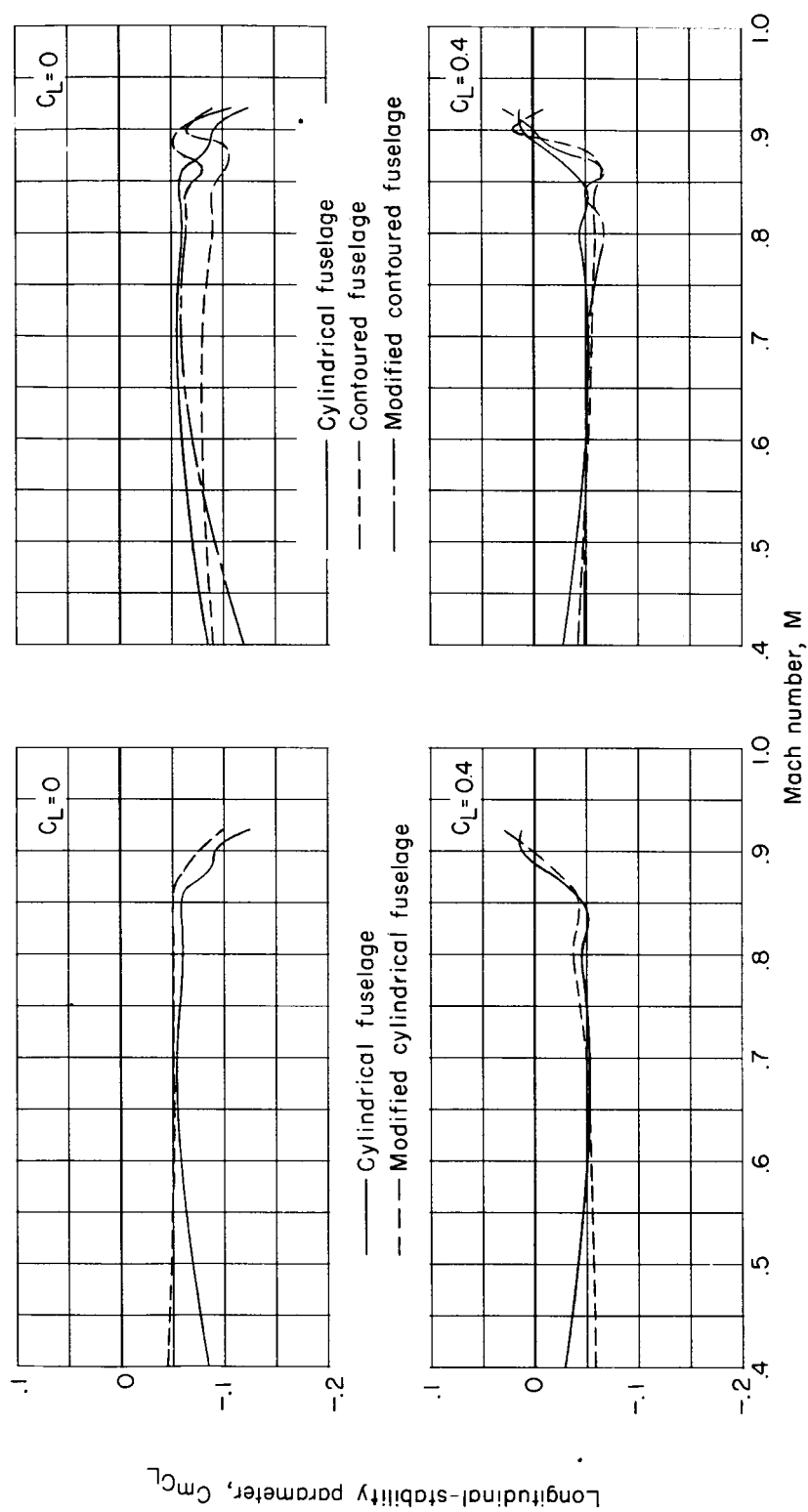
Figure 25.- Variation of longitudinal-stability parameter with Mach number for the various wing-fuselage combinations.
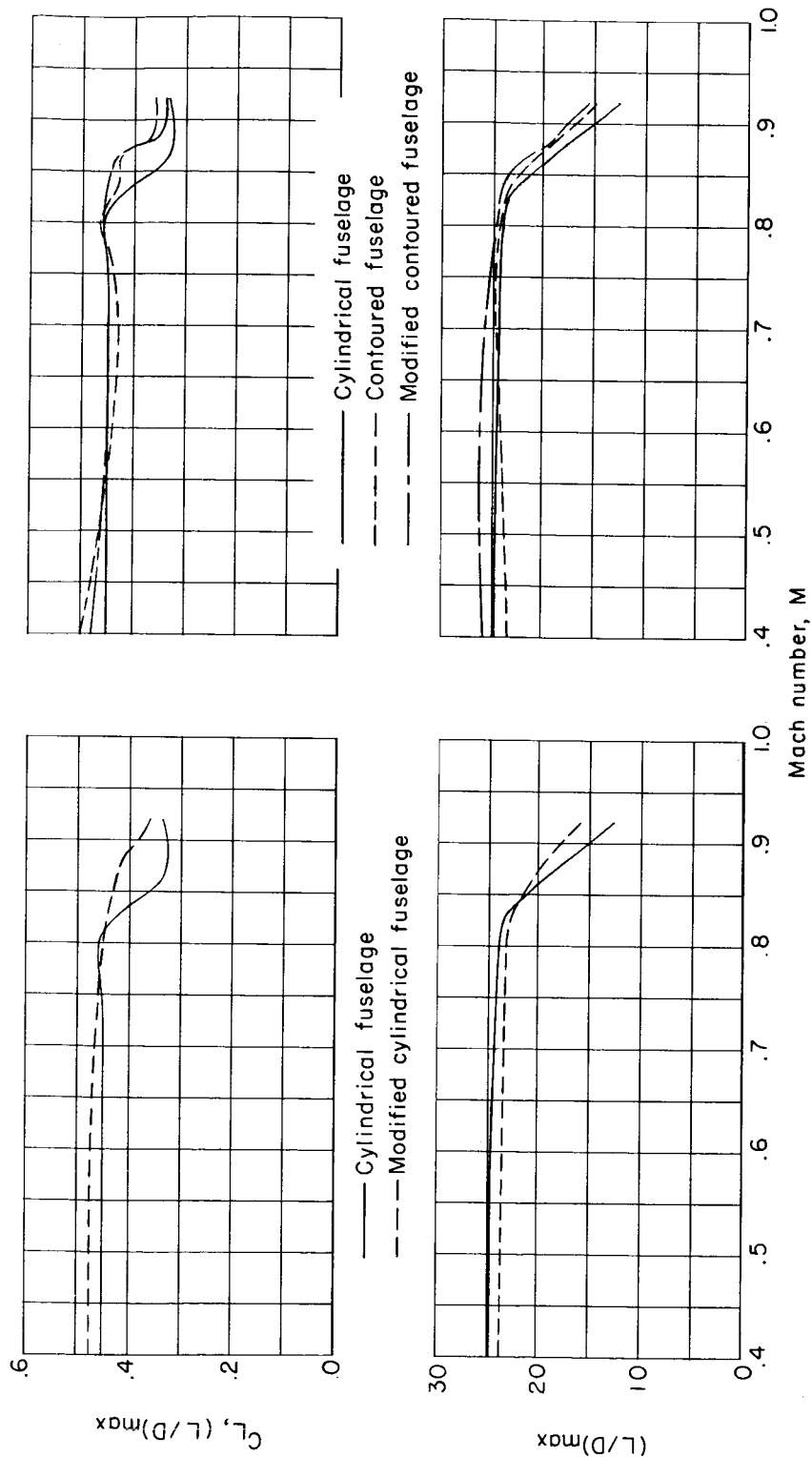
Figure 26.- Variation with Mach number of maximum lift-drag ratio and lift coefficient at maximum lift-drag ratio with Mach number for the various wing-fuselage combinations.
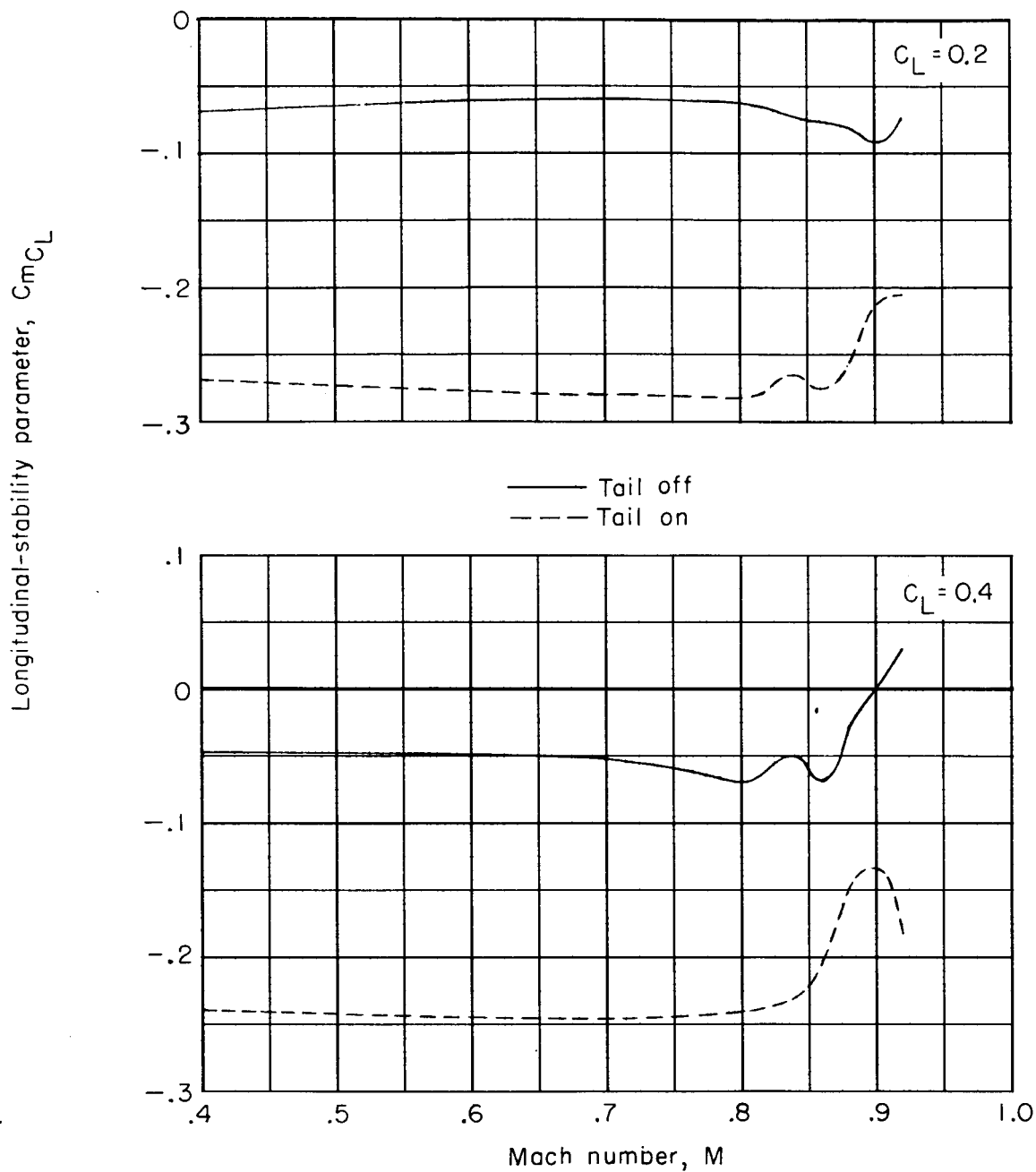
Figure 27.- Comparison of longitudinal-stability parameters for the wing in combination with the modified contoured body and vertical tail. Horizontal tail off and on ($i_t = -1^o$).

L-707
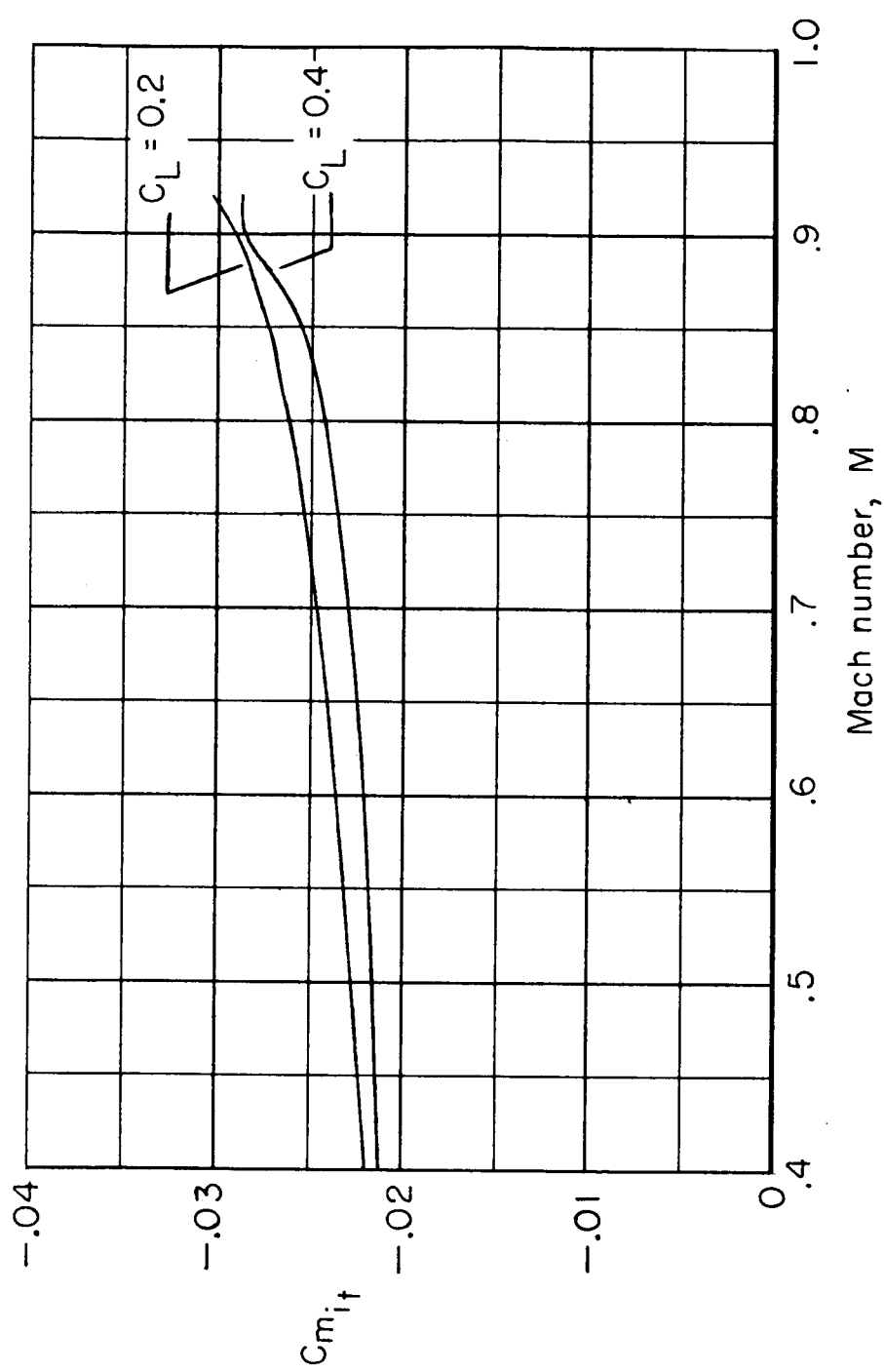
Figure 28.- Variation of horizontal-tail effectiveness parameter with Mach number for the configuration with wing, modified contoured fuselage, and vertical tail.
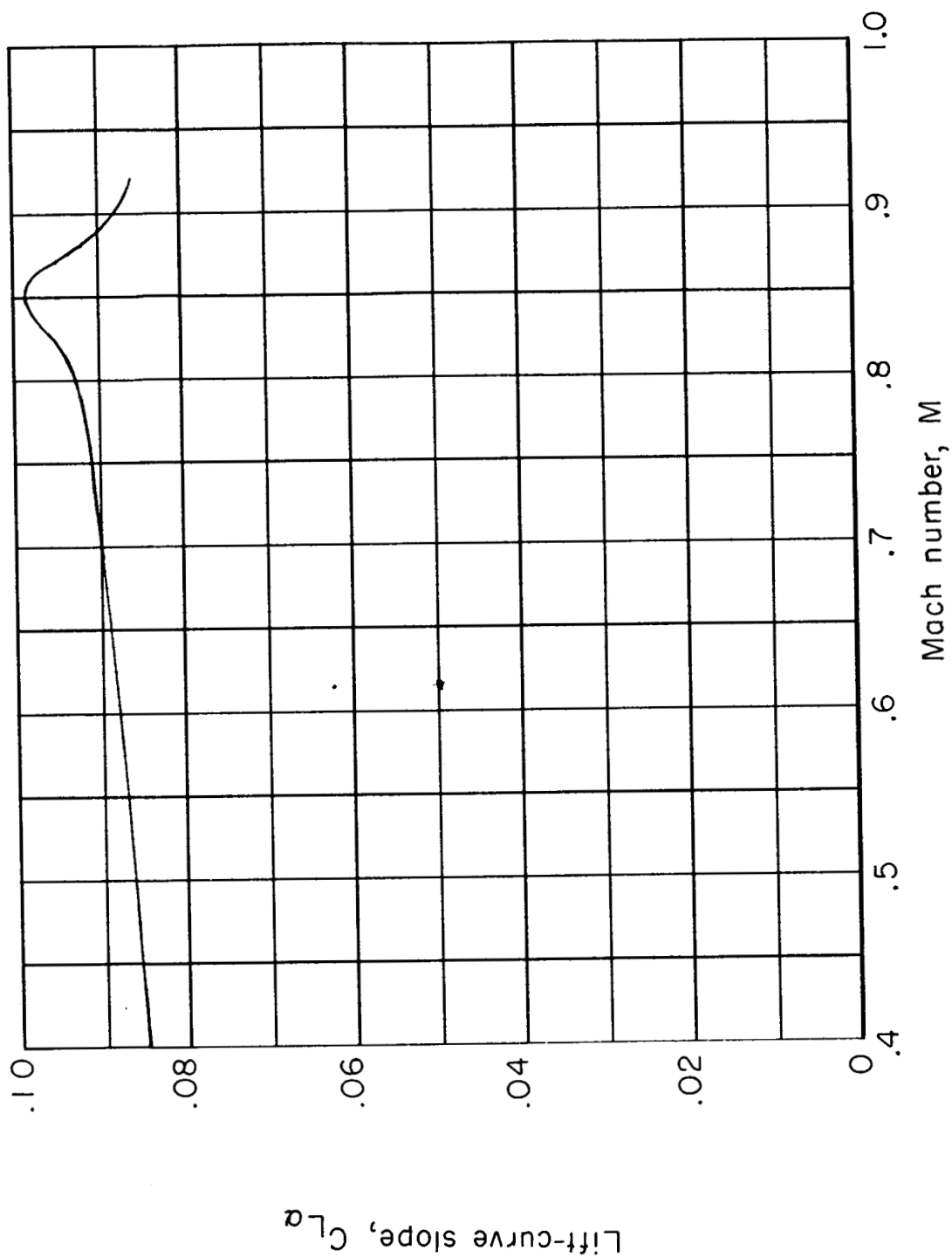
Figure 29.- Variation of lift-curve slope with Mach number for the complete configuration with the modified contoured fuselage and horizontal tail at $i_t = -1^\circ$; $\alpha = 0^\circ$.

L-707

L-707
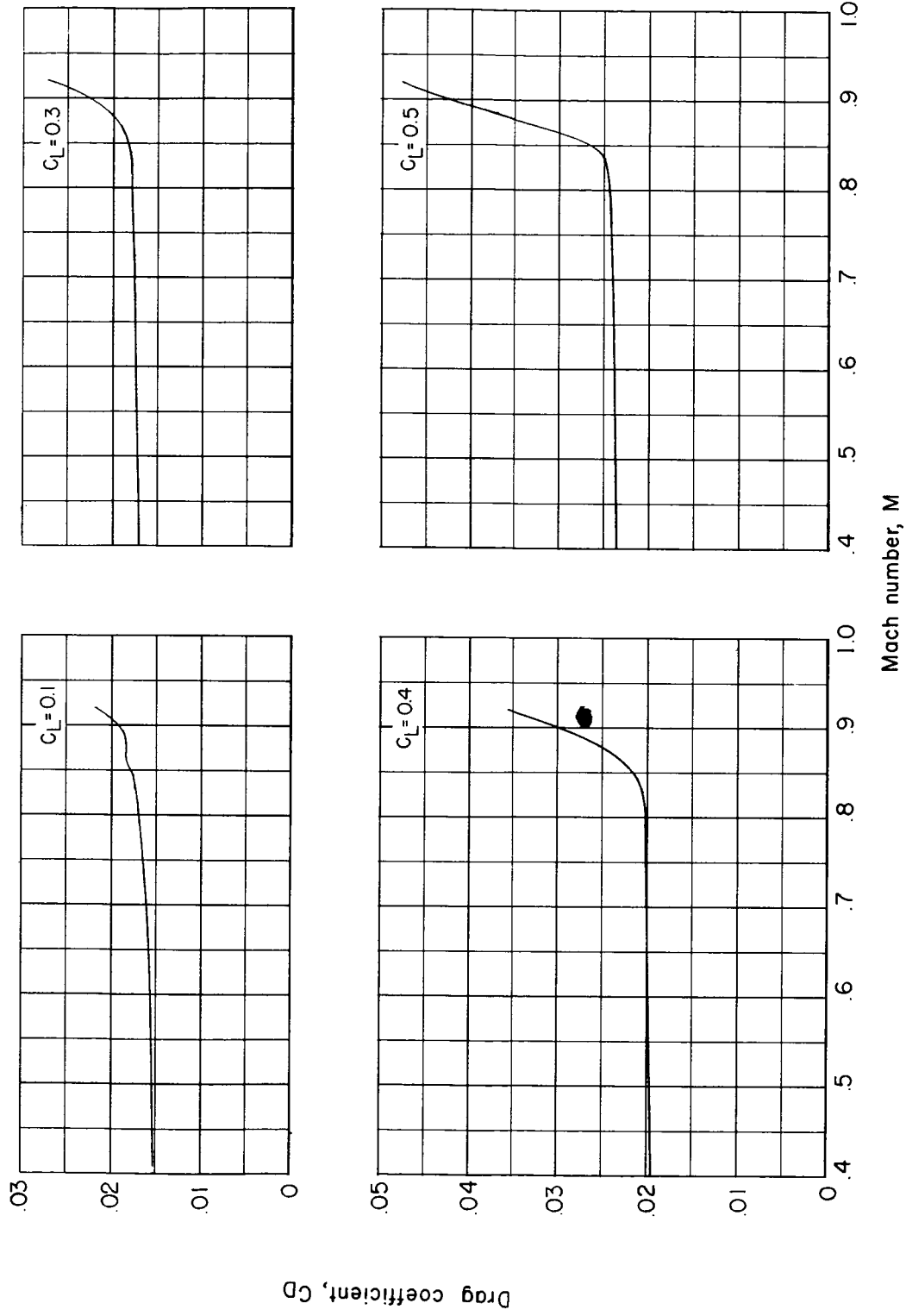
Figure 30.- Variation of drag coefficient with Mach number for complete configuration with the modified contoured fuselage and horizontal tail at $i_t = -1°$.
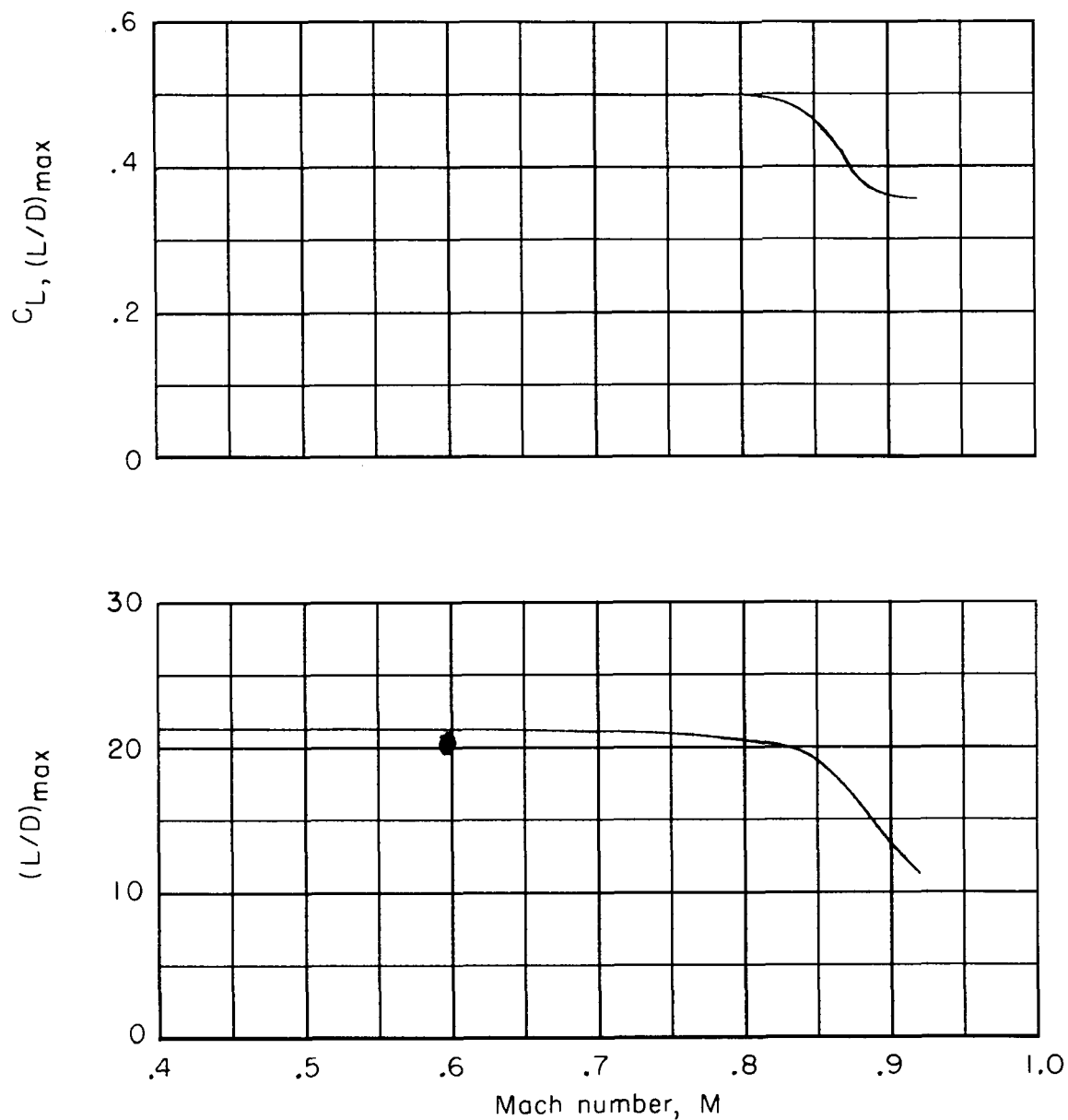
Figure 31.- Variation of maximum lift-drag ratio and lift coefficient at maximum lift-drag ratio with Mach number for complete configuration with the modified contoured fuselage and horizontal tail at $i_t = -1^o$.
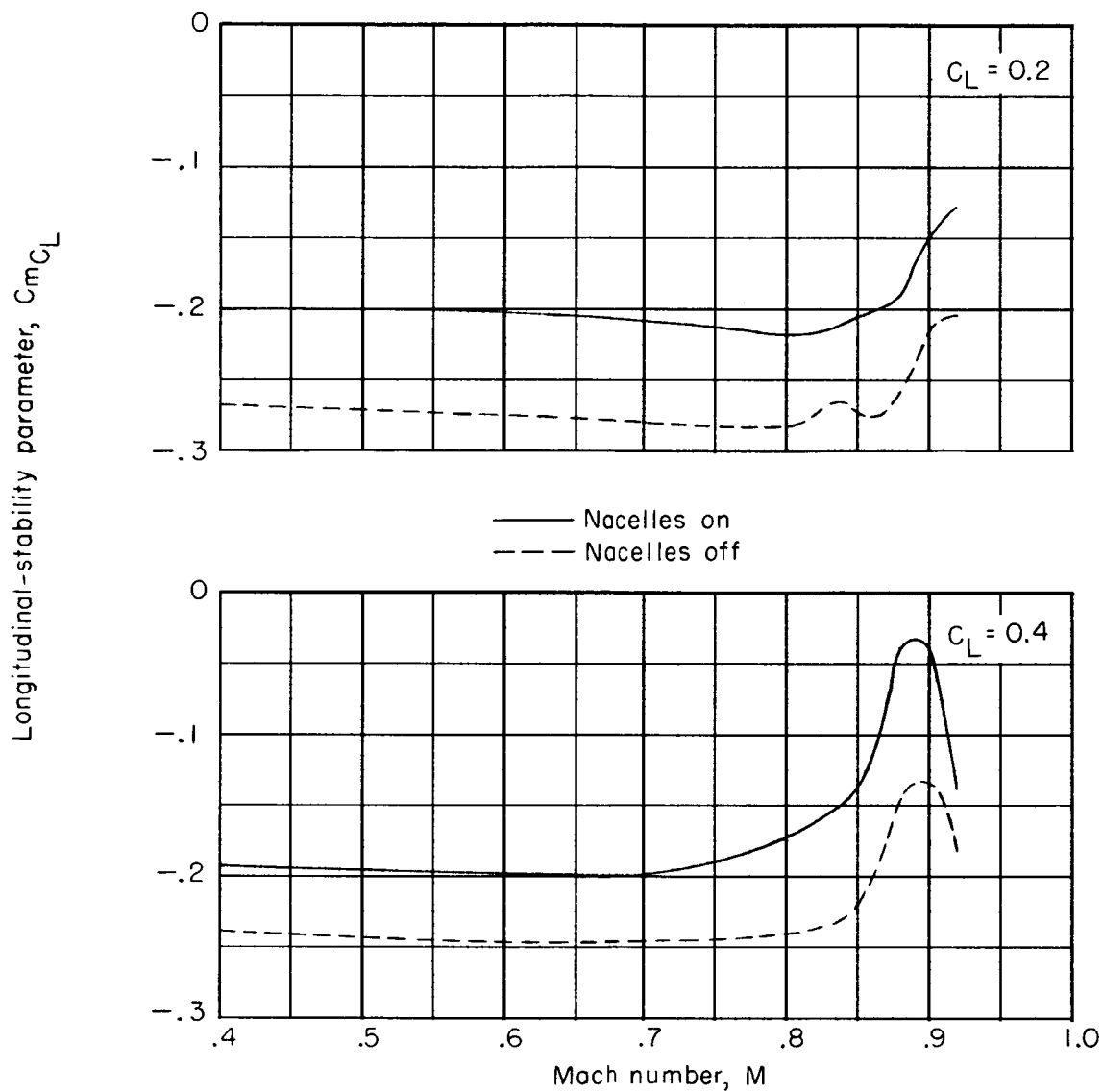
Figure 32.- Effect of nacelles on the static-longitudinal-stability parameter for the configuration with the modified contoured fuselage, vertical tail, and horizontal tail at $i_t = -1^o$.
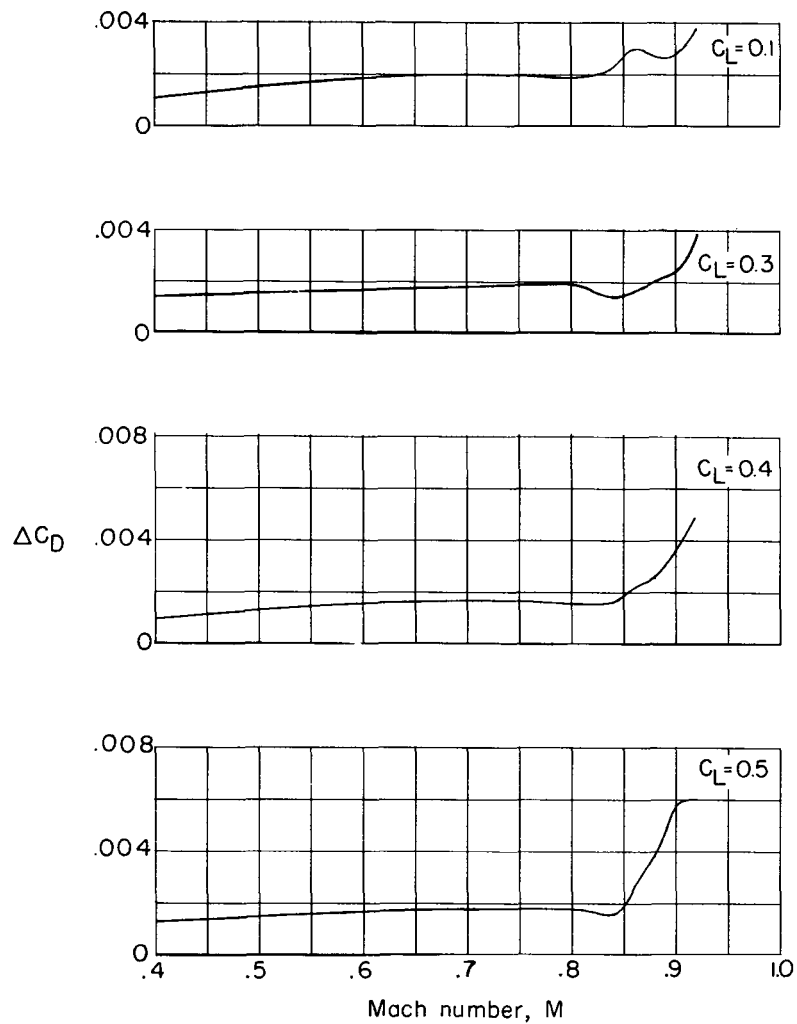
Figure 33.- Variation of the increment in drag coefficient due to the pylon-mounted nacelles with Mach number.
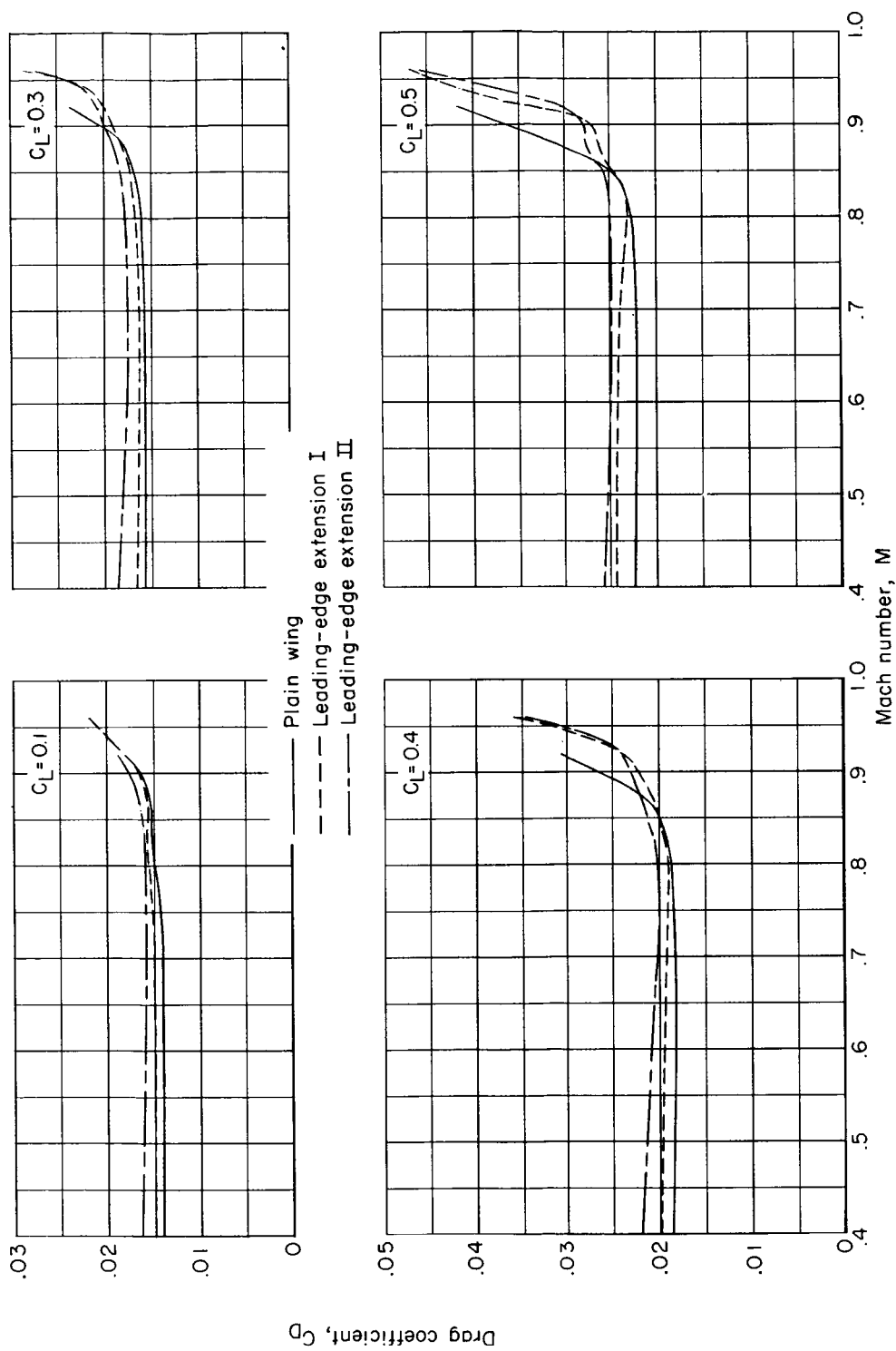
Figure 34.- Effect of two wing leading-edge extensions on the variation of drag coefficient with Mach number for the wing in combination with the modified contoured fuselage, vertical tail, and horizontal tail at $i_t = -1^o$.
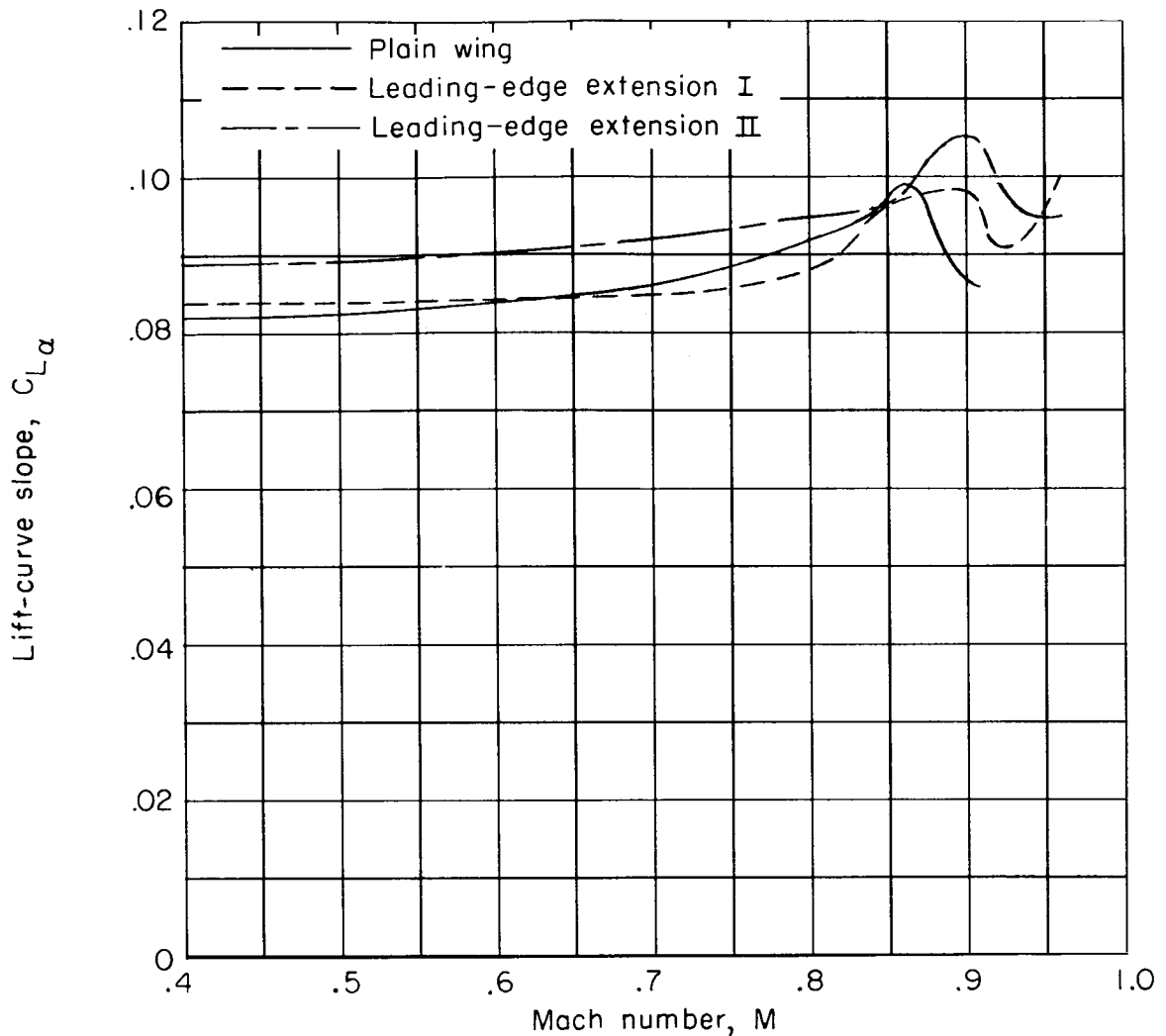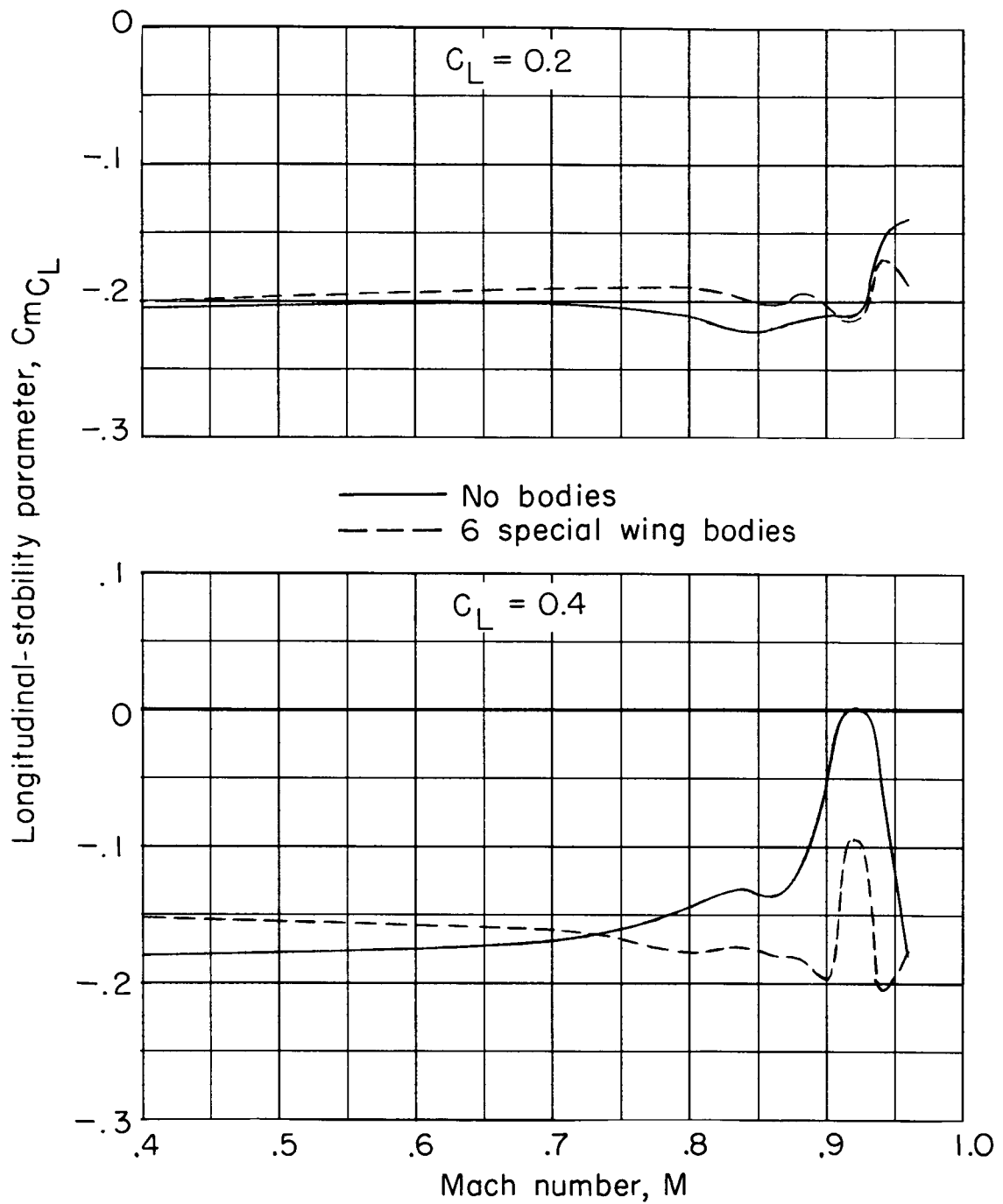
Figure 35.- Effect of two leading-edge extensions on the variation of lift-curve slope with Mach number for the wing in combination with modified contoured fuselage, vertical tail, and horizontal tail at $i_t = -1^O$; $\alpha = 0^O$.
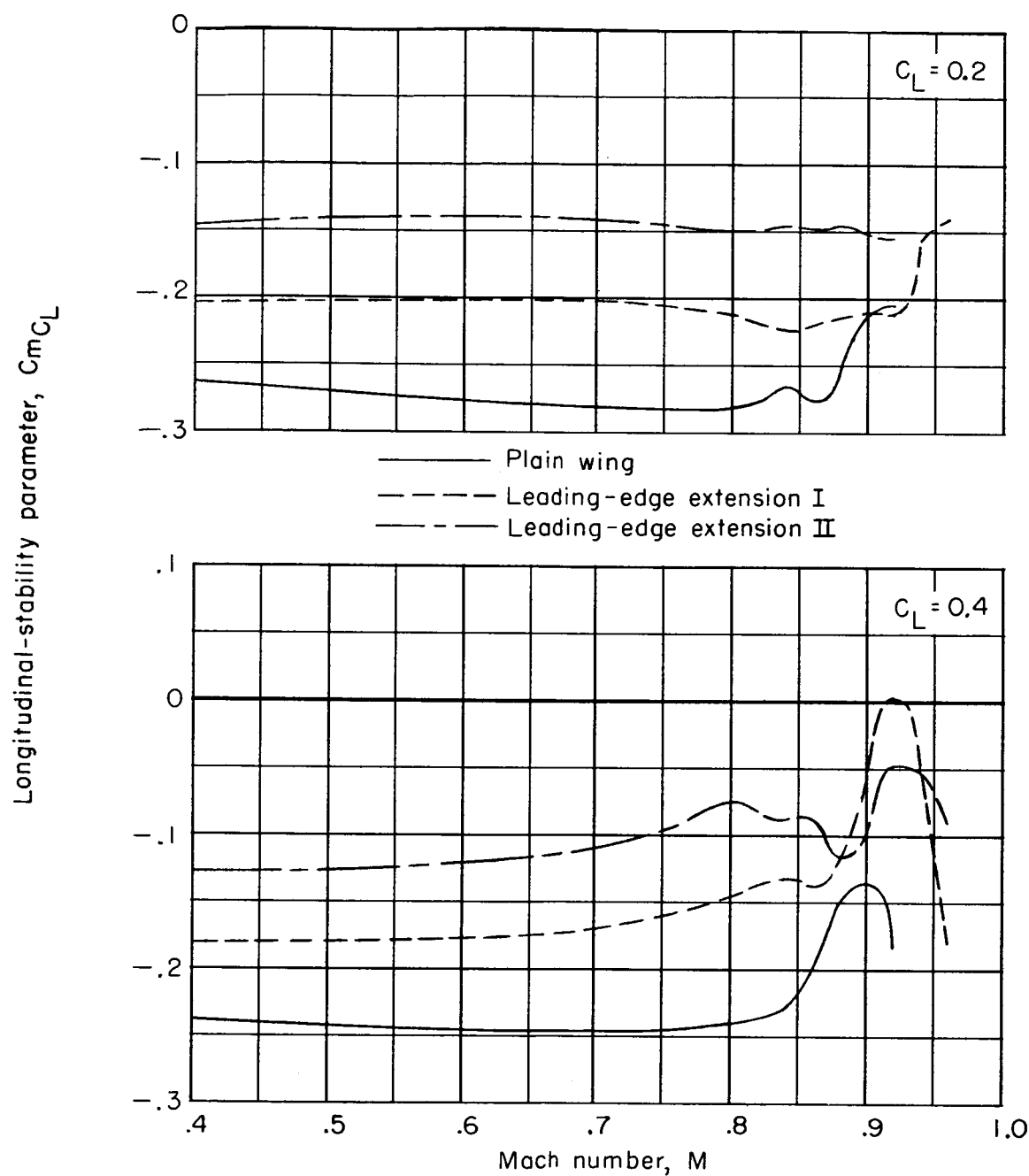
Figure 36.- Effect of two wing leading-edge extensions on the variation of longitudinal-stability parameter with Mach number for the wing in combination with modified contoured fuselage, vertical tail, and horizontal tail at $i_t = -1°$.
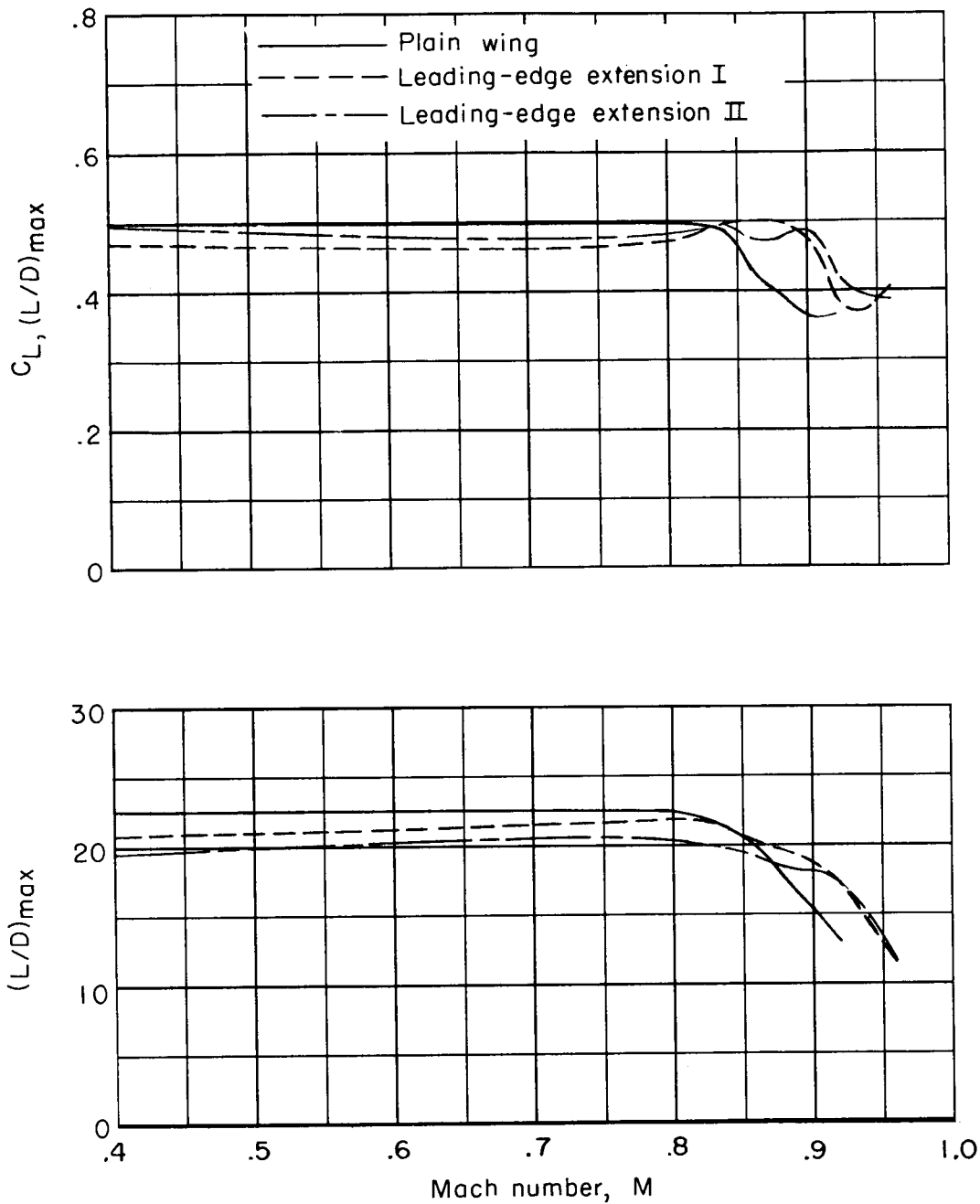
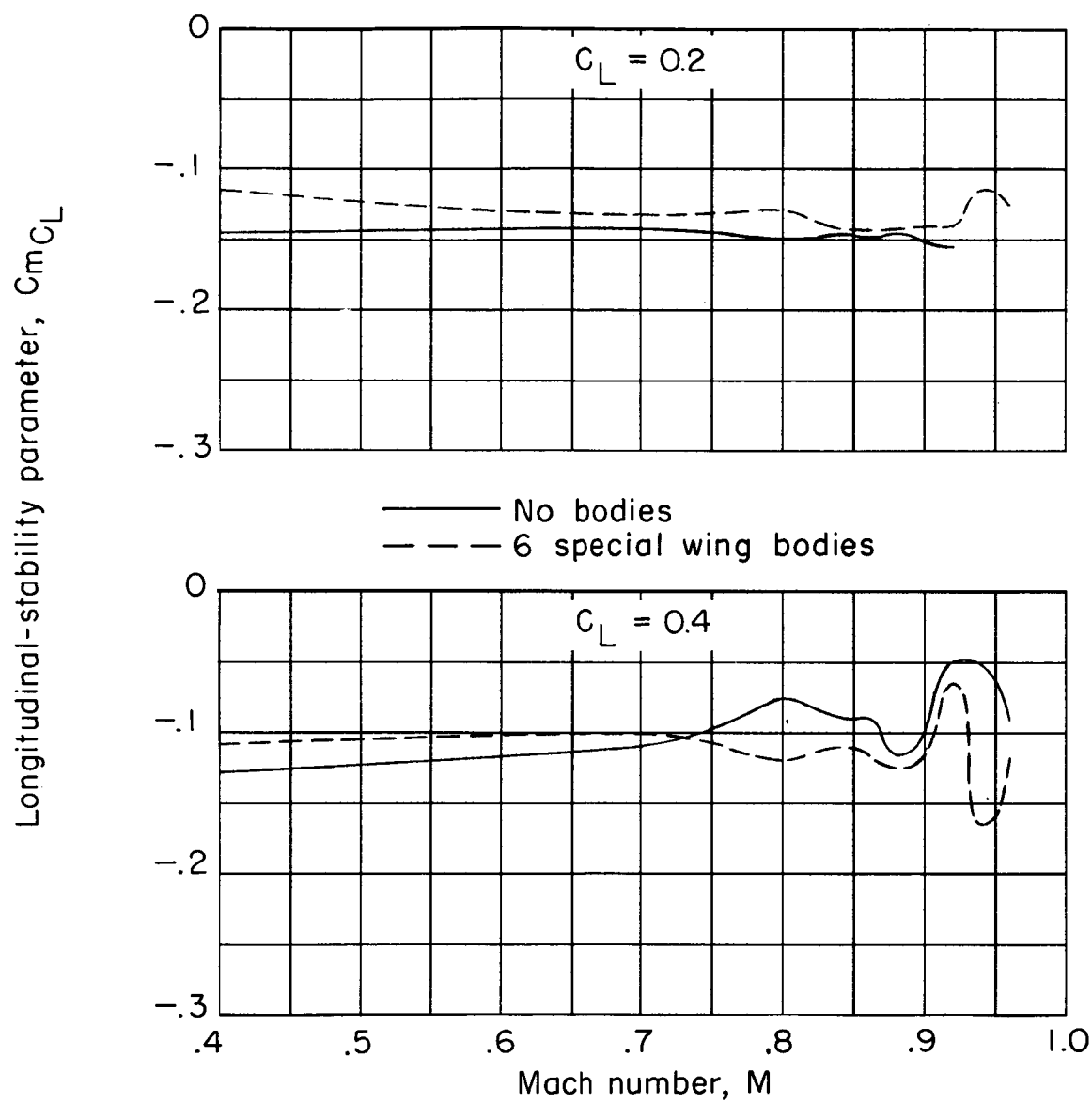Figure 37.- Effect of two wing leading-edge extensions on the variation of maximum lift-drag ratio and lift coefficient at maximum lift-drag ratio for the wing in combination with the modified contoured fuselage, vertical tail, and horizontal tail at $i_t = -1°$.

L-707

75
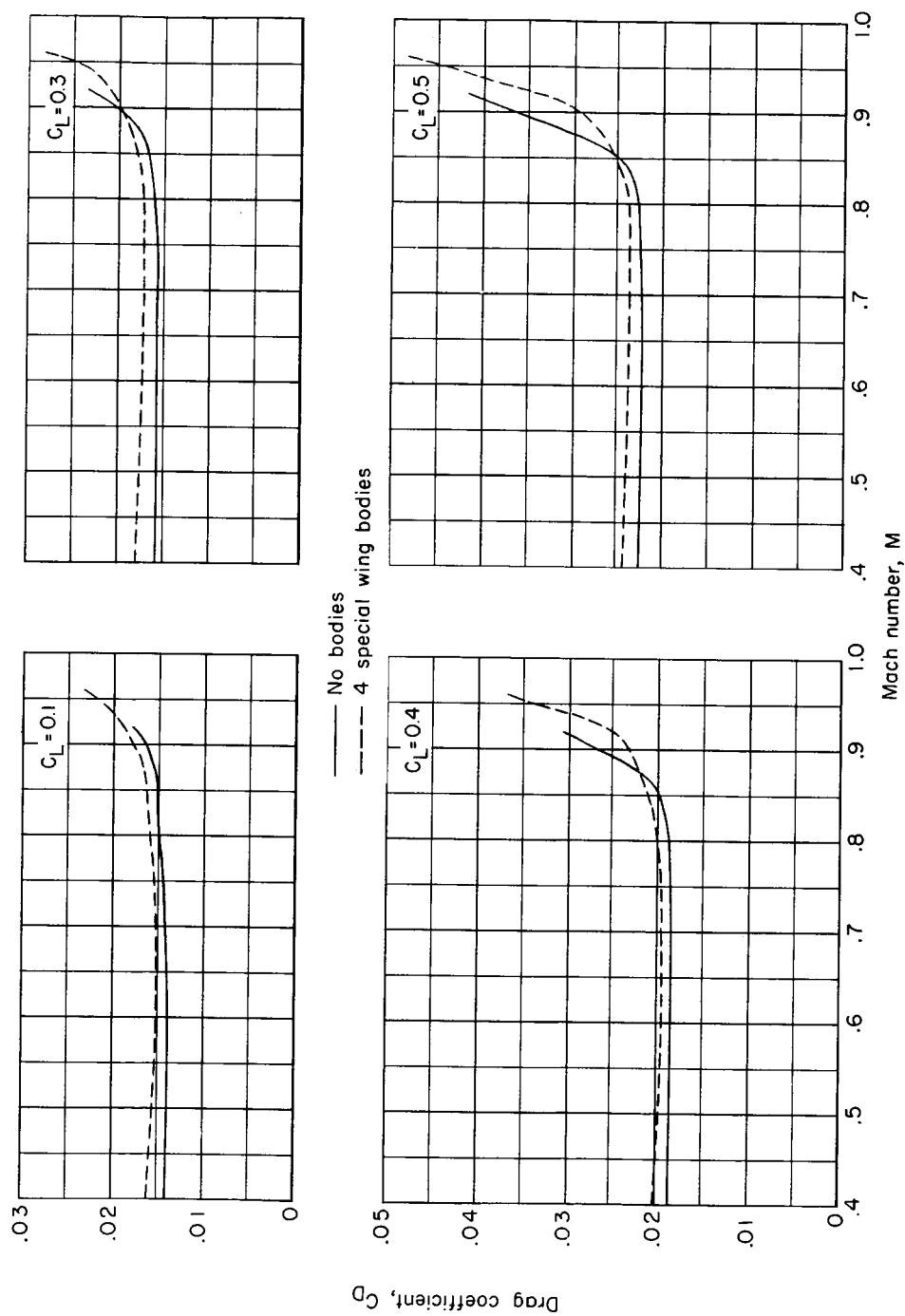
(a) Plain wing.

Figure 38.- Effect of special wing bodies on the variation of drag coefficient with Mach number for the wing in combination with modified contoured fuselage, vertical tail, and horizontal tail at $i_t = -1°$.
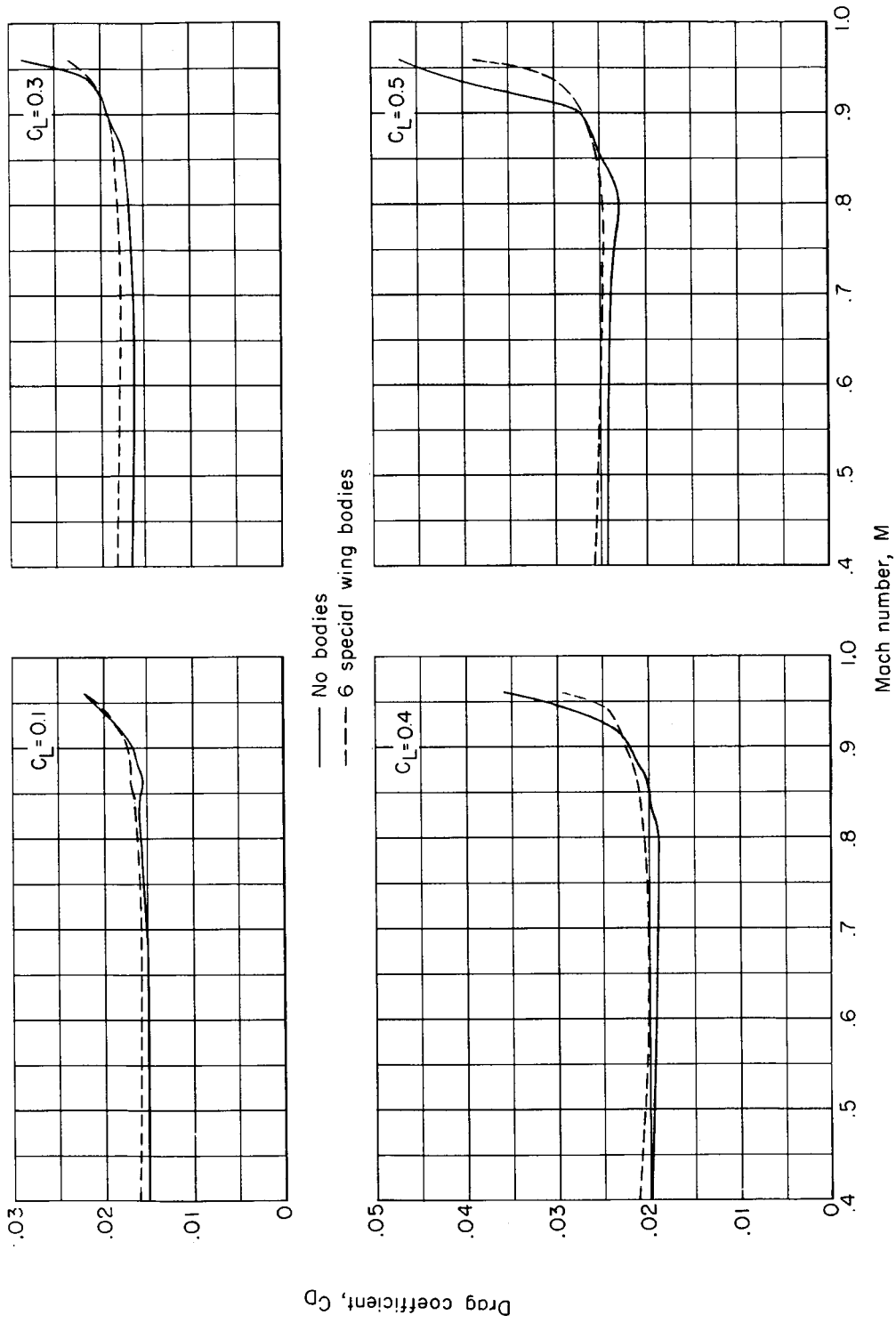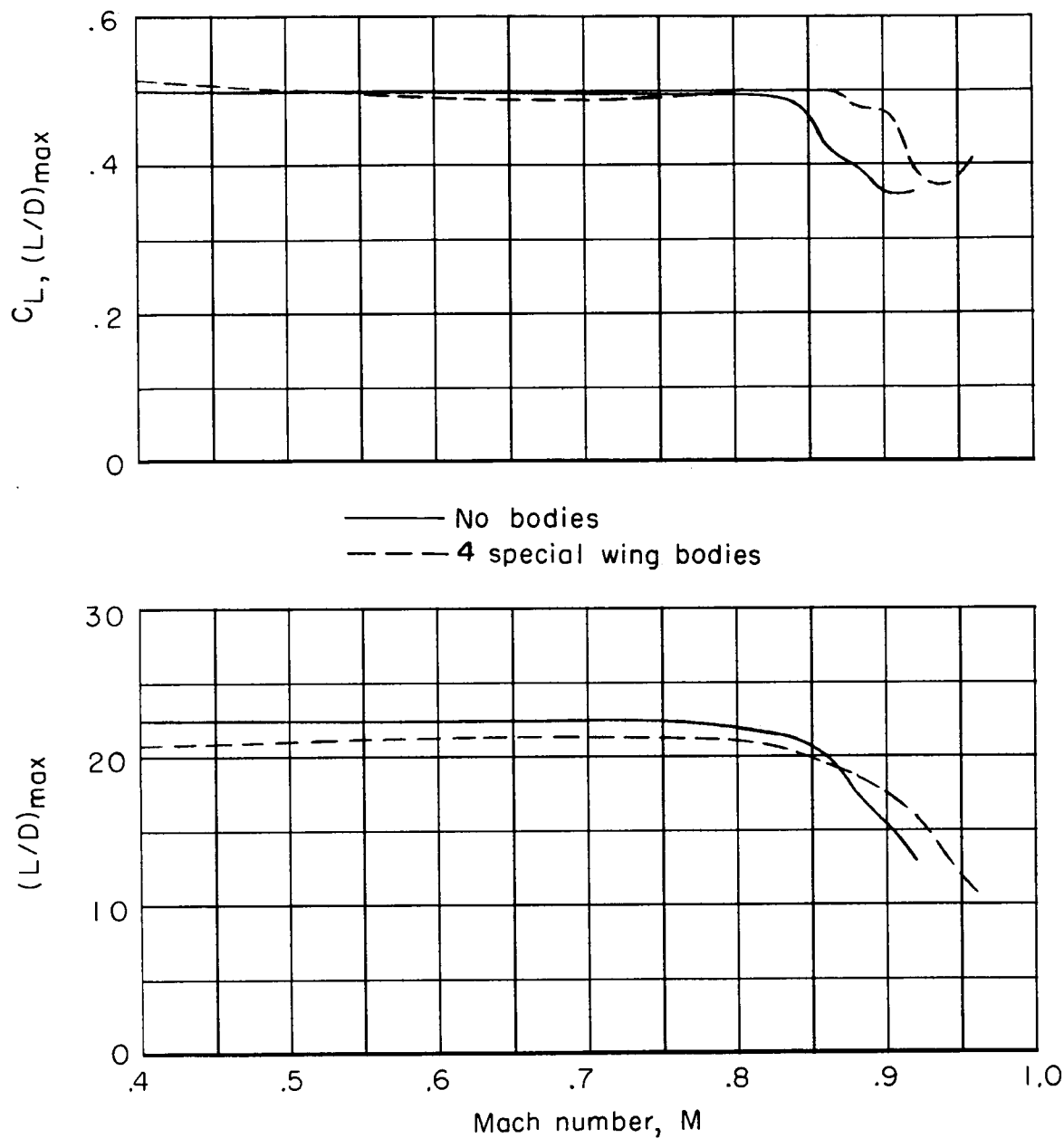
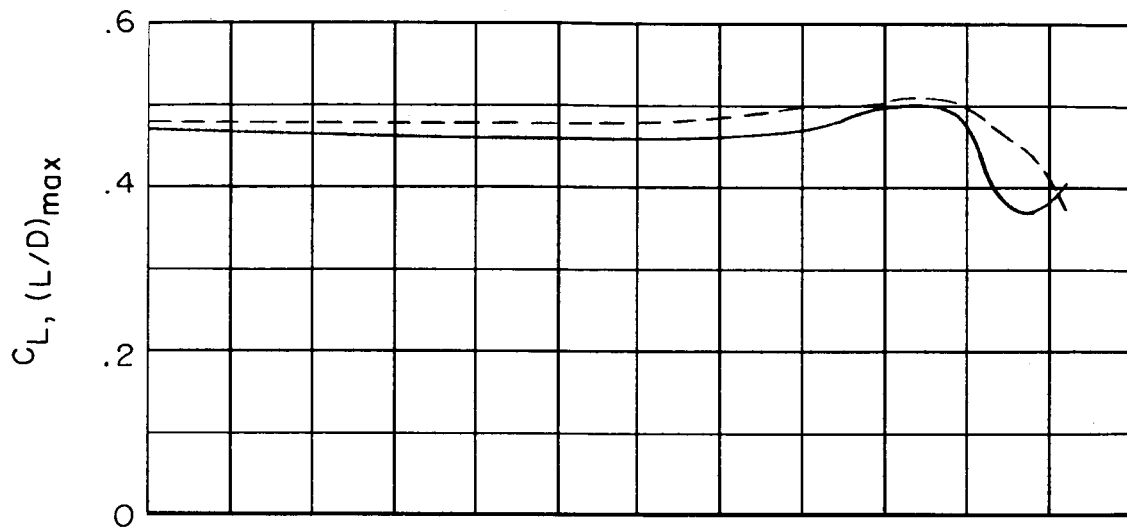(b) Wing with leading-edge extension I.

Figure 38.- Continued.
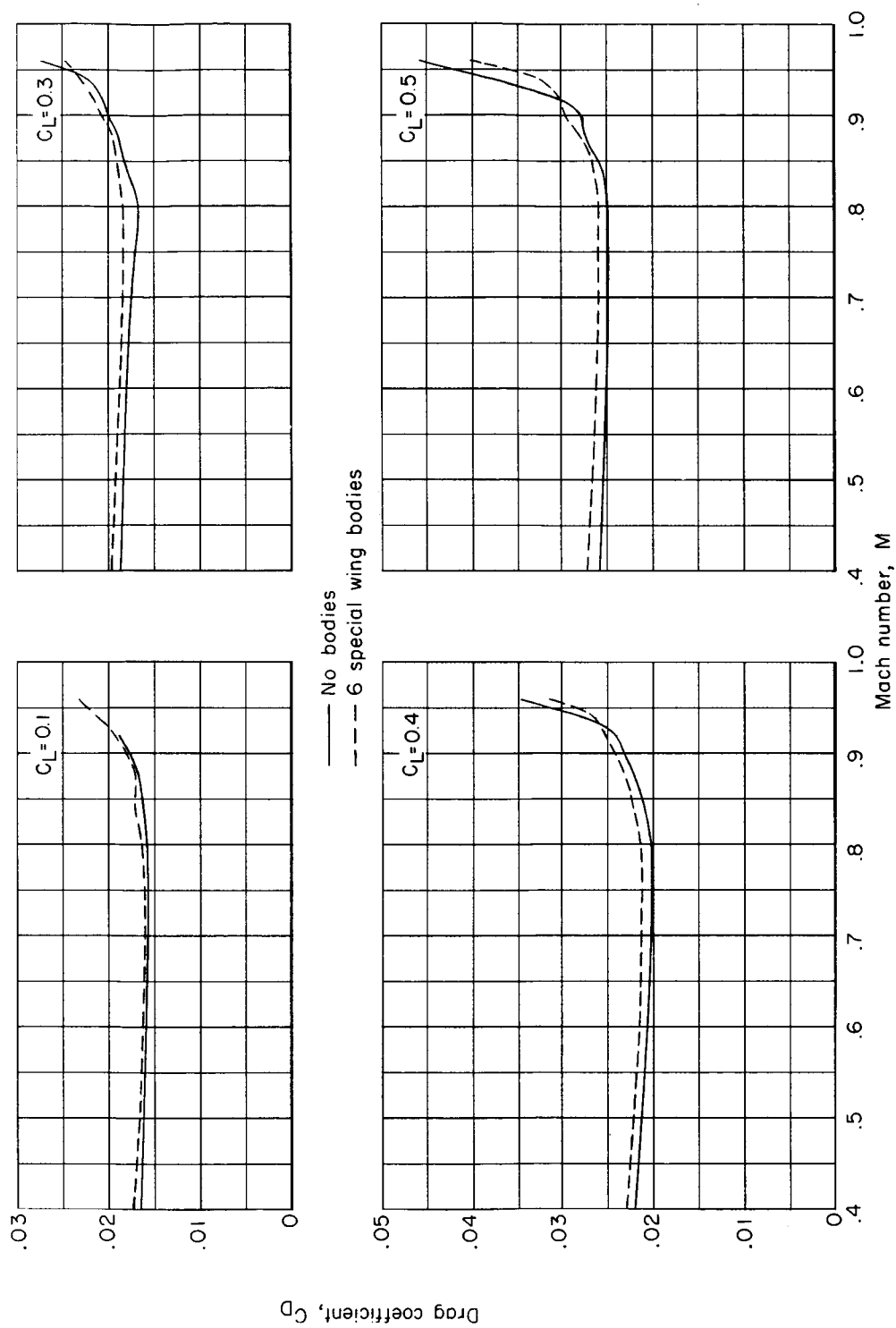
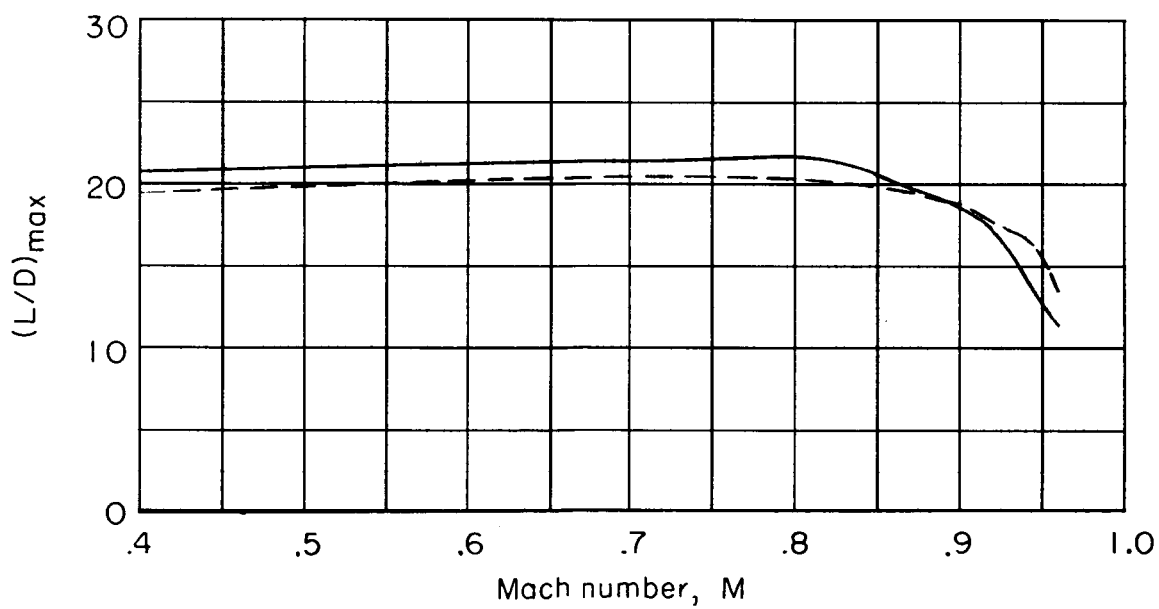(c) Wing with leading-edge extension II.

Figure 38.- Concluded.
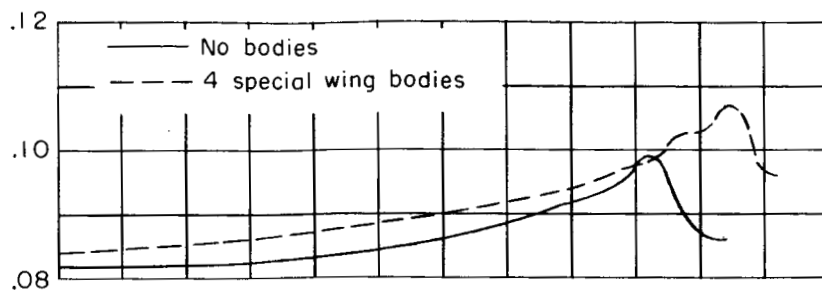
(a) Plain wing.
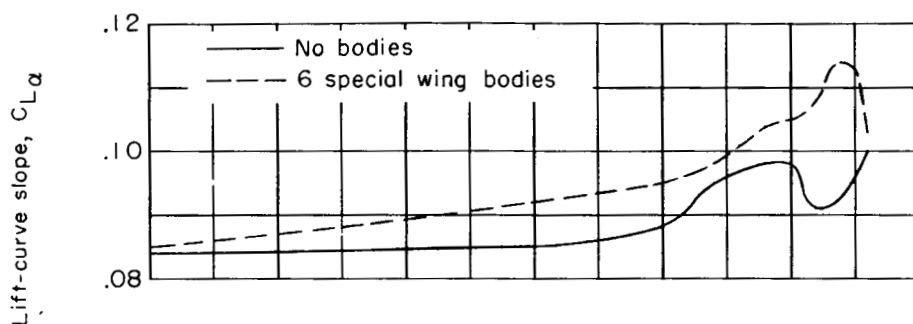
(b) Wing with leading-edge extension I.
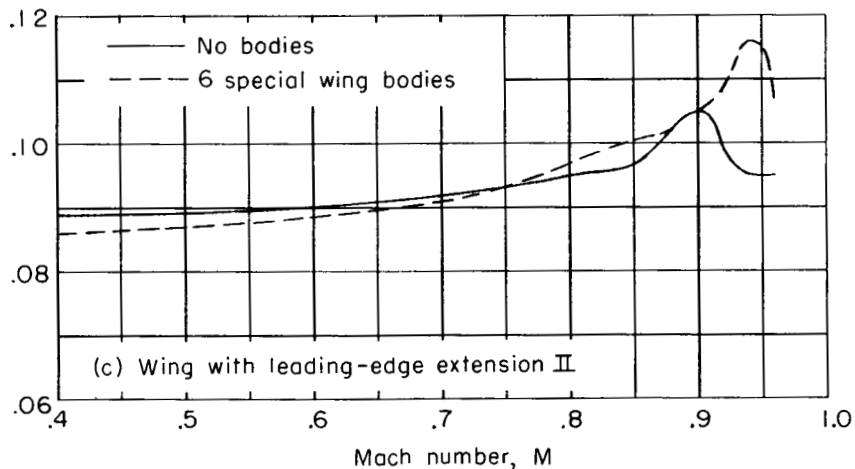
(c) Wing with leading-edge extension II.

Figure 39.- Effect of special wing bodies on the variation of lift-curve slope with Mach number for the wing in combination with modified contoured body, vertical tail, and horizontal tail at $i_t = -1^o$.
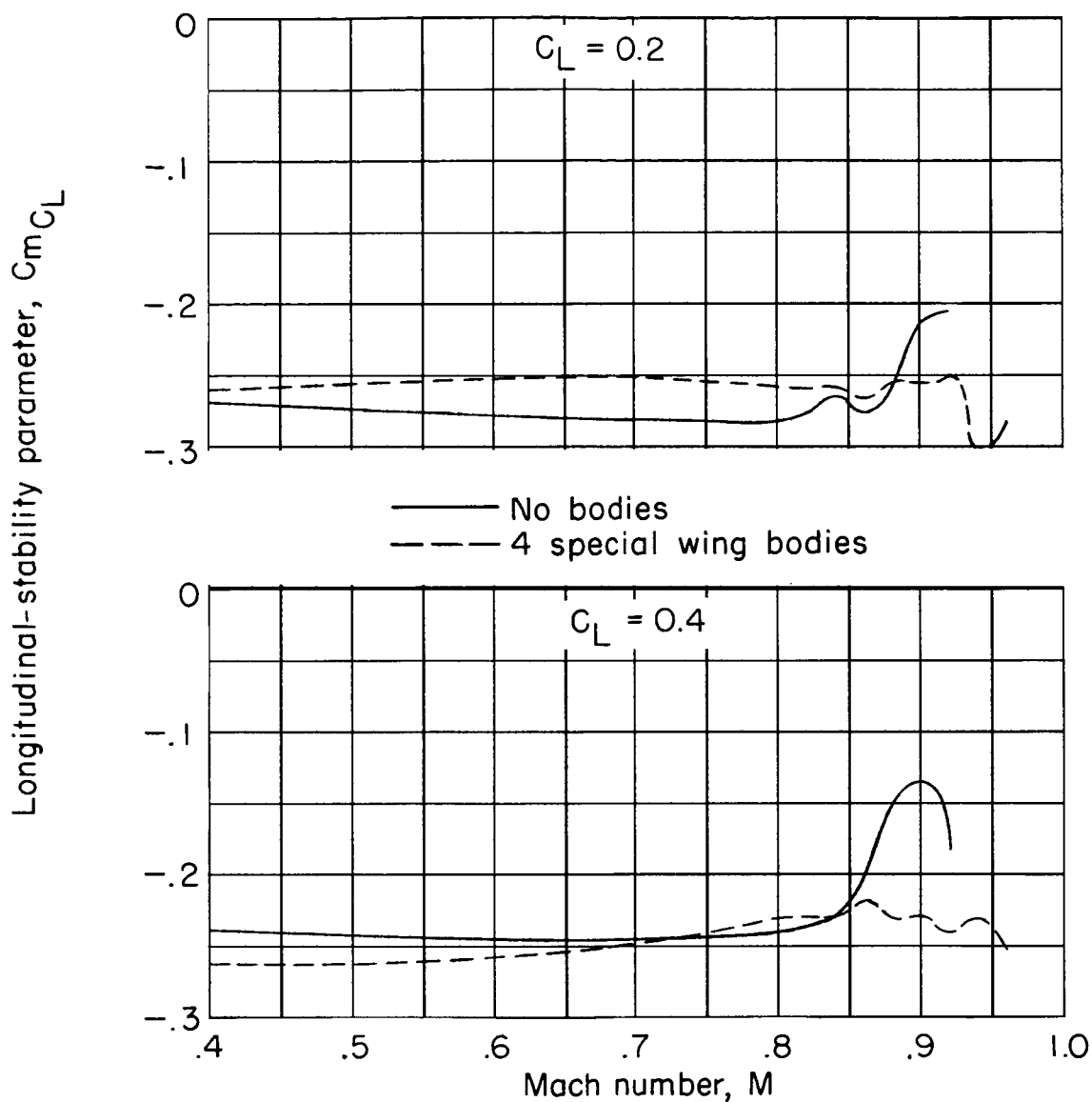
(a) Plain wing.

Figure 40.- Effect of four special wing bodies on the variation of the longitudinal-stability parameter with Mach number for the wing in combination with modified contoured fuselage, vertical tail, and horizontal tail at $i_t = -1°$.

(b) Wing with leading-edge extension I.

Figure 40.- Continued.

L-707

(c) Wing with leading-edge extension II.

Figure 40.- Concluded.

(a) Plain wing.

Figure 41.- Effect of four special wing bodies on the variation with
Mach number of the maximum lift-drag ratio and lift coefficient
at maximum lift-drag ratio for the wing in combination with the
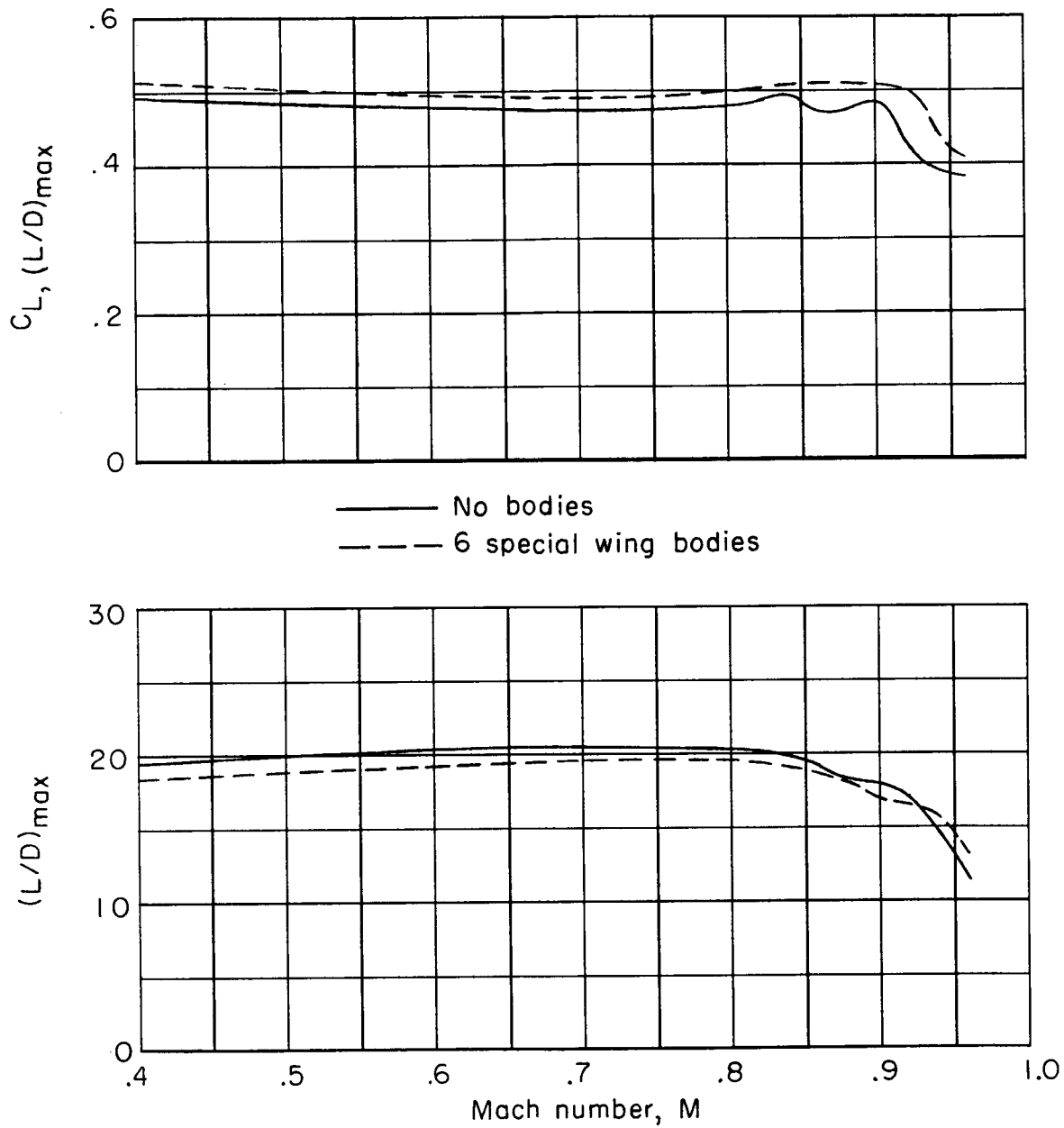modified contoured fuselage, vertical tail, and horizontal tail
at $i_t = -1^o$.

(b) Wing with leading-edge extension I.

Figure 41.- Continued.

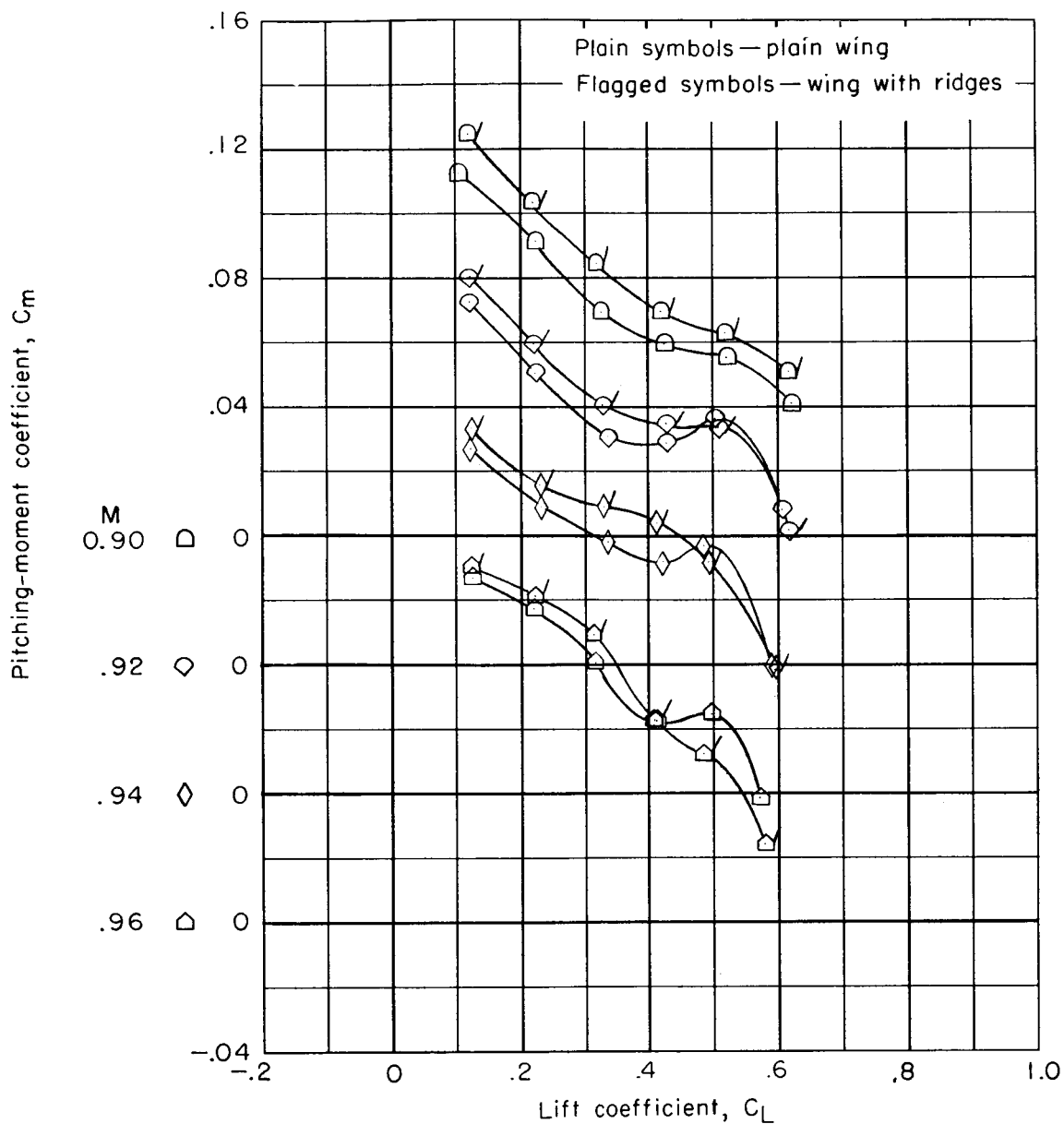(c) Wing with leading-edge extension II.

Figure 41.- Concluded.

Figure 42.- Effect of wing lower surface ridges on the variation of pitching-moment coefficient with lift coefficient for the wing with leading-edge extension I in combination with the modified contoured fuselage, vertical tail, and horizontal tail at $i_t = -1°$.
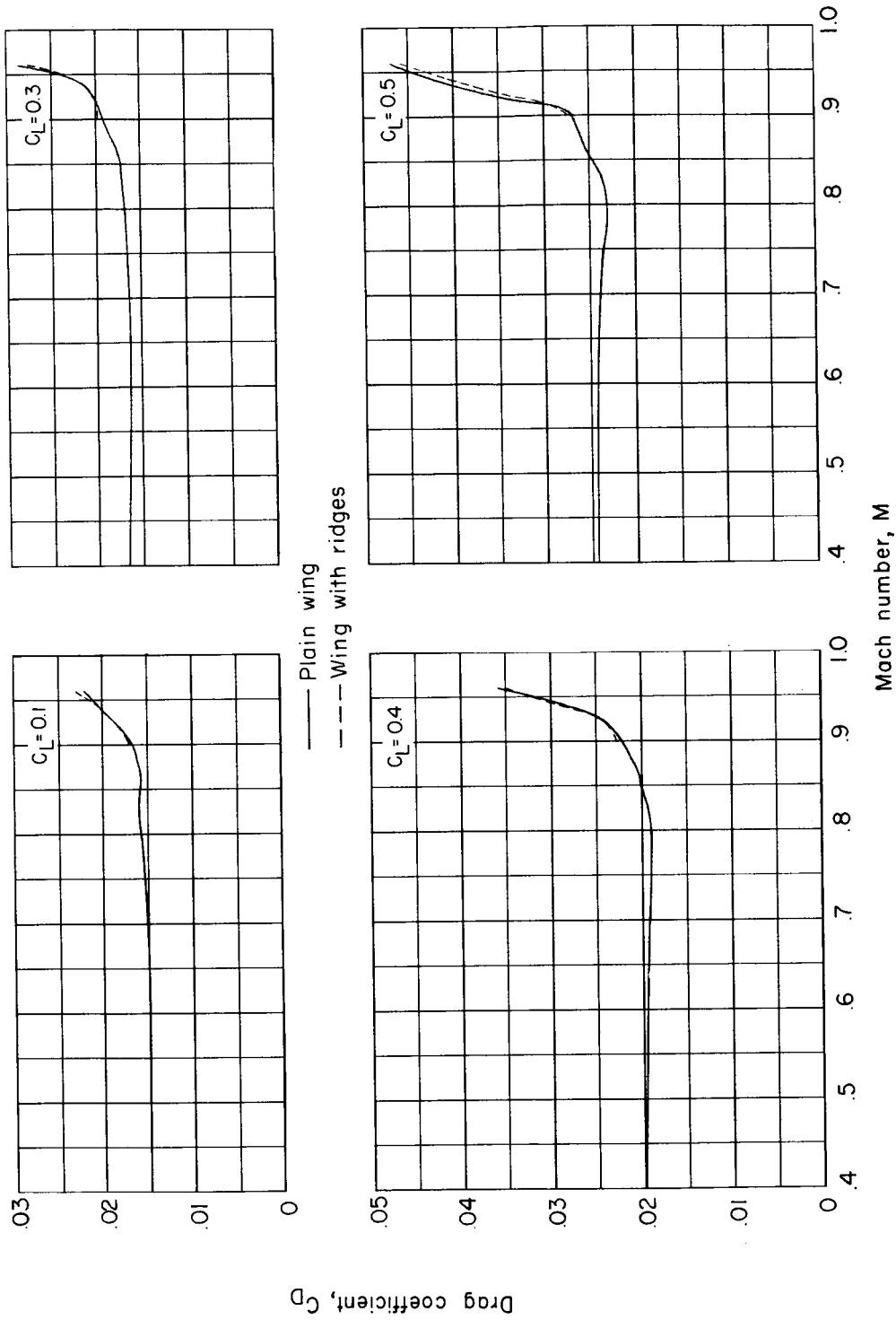
Figure 43.- Effect of wing lower surface ridges on the variation of drag coefficient with Mach number for the wing with leading-edge extension I in combination with the modified contoured fuselage, vertical tail, and horizontal tail at $i_t = -1^\circ$.
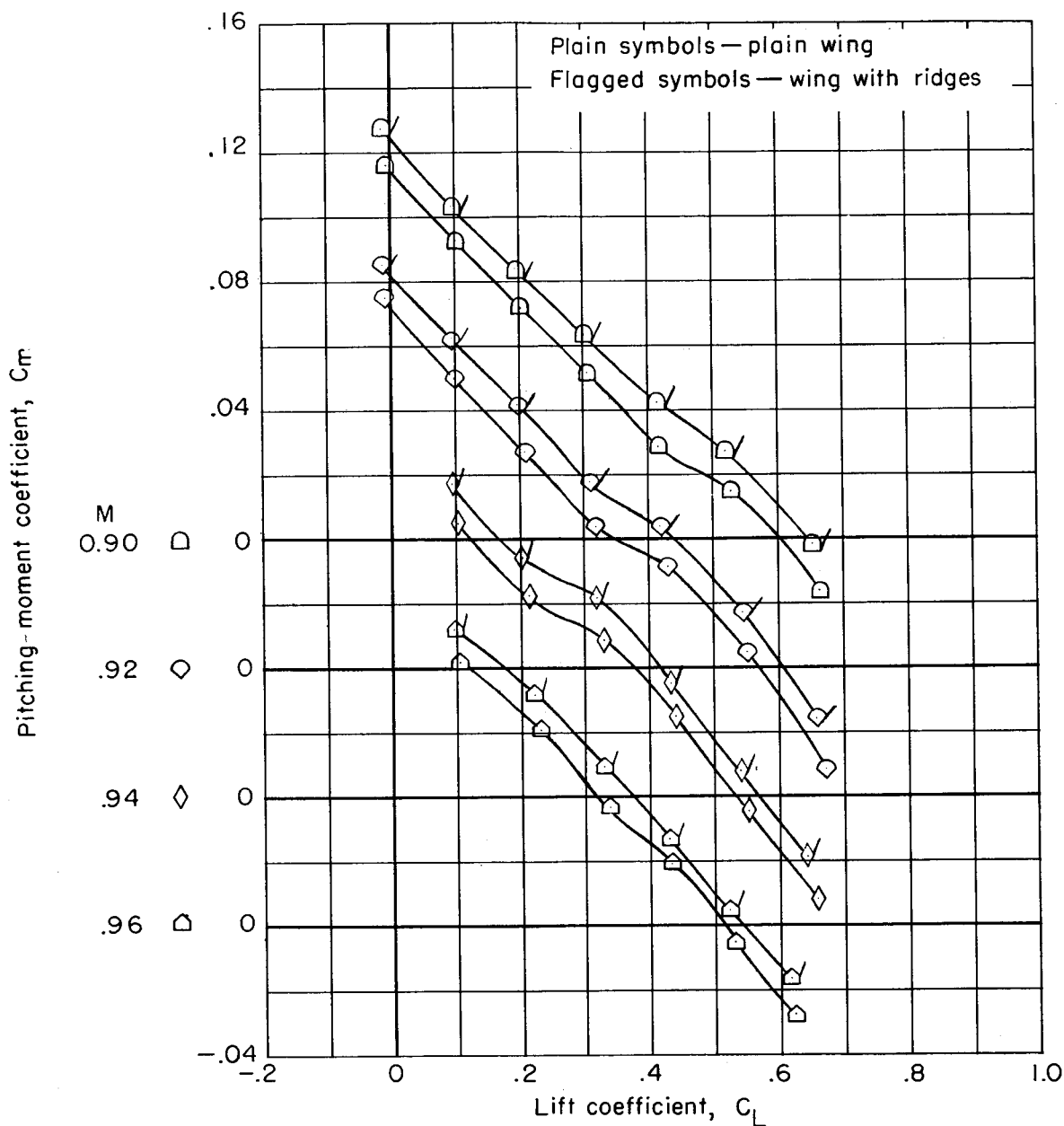
Figure 44.- Effect of wing lower surface ridges on the variation of pitching-moment coefficient with lift coefficient for the wing in combination with modified contoured fuselage, vertical tail, horizontal tail at $i_t = -1^\circ$, and six special wing bodies.
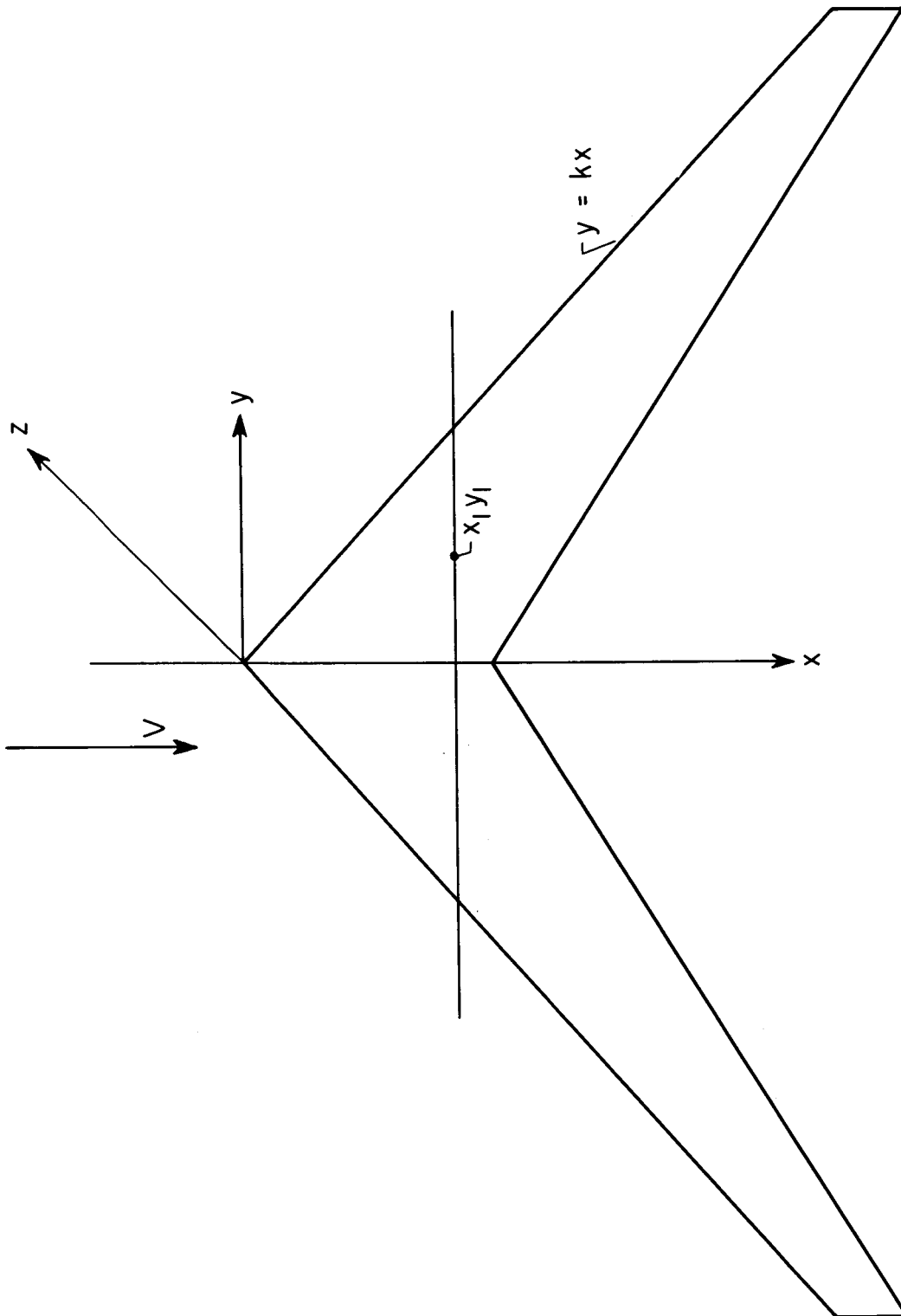
Figure 45.- Sketch of coordinate system and wing plan form used for calculation of wing camber surface.